Molecular Dynamics Simulation of Open Systems far from Equilibrium

Dissertation

zur Erlangung des Grades eines
Doktors der Naturwissenschaften
(Dr. rer. nat.)

am Fachbereich Mathematik und Informatik
der Freien Universität Berlin

vorgelegt von
Roya Ebrahimi Viand

Berlin 2022

Erstgutachter: Prof. Dr. Felix Höfling

Zweitgutachter: Prof. Dr. Jürgen Horbach

Tag der Disputation: 28.10.2022

Declaration of authorship

Name: Ebrahimi Viand
First name: Roya

I declare to the Freie Universität Berlin that I have completed the submitted dissertation independently and without the use of sources and aids other than those indicated. The present thesis is free of plagiarism. I have marked as such all statements that are taken literally or in content from other writings. This dissertation has not been submitted in the same or similar form in any previous doctoral procedure.

I agree to have my thesis examined by a plagiarism examination software.

Date: Signature:

To my wonderful father

Acknowledgements

First and foremost, I would like to thank my supervisor, Prof. Dr. Felix Höfling, for his guidance and support. I learned a lot over the past 3.5 years, and it would not have been possible without his patience, for which I am grateful. I also want to thank my other supervisors, Prof. Dr. Luigi Delle Site and Prof. Dr. Rupert Klein, for their help and fruitful advice. I would also like to express my gratitude to my colleague and friend Abbas Gholami.
My special thanks go to Sina Dortaj for all of his help and for always being willing to discuss the challenges of the project, as well as for his never-ending encouragement. None of this would have been possible without the emotional support of my parents and sister.

Abstract

Open systems have been the subject of interest in science for a long time because many complex molecular systems are open systems embedded in a large environment that serves as a reservoir of particles and energy.
In order to test the methods' accuracy and applicability, simulations of open systems exposed to different non-equilibrium conditions are performed, and the results are compared to the results of full resolution simulations and the range of applicability of the method is investigated. Furthermore, a study on fluid flow through regular bead packings as a model of a porous medium was conducted to investigate the flow–pressure relation in these media and its dependence on geometry and porosity of the medium. These simulations are also done with AdResS for extension to open boundaries.
The results presented in this thesis help to understand the capabilities of our simulation method to simulate open systems out of equilibrium. We found that by choosing proper boundary conditions and reservoir states, simulations of open systems embedded in large reservoirs of particles and energy can be done with low computational cost. The findings of this thesis pave the way for future research on applications in which a more realistic system is subjected to non-equilibrium conditions and flows of heat and mass.

Zusammenfassung

Offene Systeme sind in der Wissenschaft schon seit langem von Interesse, da viele komplexe molekulare Systeme offene Systeme sind, die in eine große Umgebung eingebettet sind, die als Reservoir für Teilchen und Energie dient.
Um die Genauigkeit und Anwendbarkeit der Methoden zu testen, werden Simulationen offener Systeme durchgeführt, die verschiedenen Nichtgleichgewichtsbedingungen ausgesetzt sind. Die Ergebnisse werden mit den Ergebnissen von Simulationen mit voller Auflösung verglichen und der Anwendungsbereich der Methode wird untersucht. Darüber hinaus wurde eine Studie über die Flüssigkeitsströmung durch regelmäßige Perlenpackungen als Modell eines porösen Mediums durchgeführt, um die Strömungs-Druck-Beziehung in diesen Medien und ihre Abhängigkeit von der Geometrie und Porosität des Mediums zu untersuchen. Diese Simulationen wurden auch mit AdResS zur Erweiterung auf offene Grenzen durchgeführt.
Die in dieser Arbeit vorgestellten Ergebnisse helfen, die Fähigkeiten unserer Simulationsmethode zur Simulation offener Systeme außerhalb des Gleichgewichts zu verstehen. Wir haben festgestellt, dass durch die Wahl geeigneter Randbedingungen und Reservoirzustände Simulationen offener Systeme, die in große Reservoirs von Teilchen und Energie eingebettet sind, mit geringem Rechenaufwand durchgeführt werden können. Die Ergebnisse dieser Arbeit ebnen den Weg für künftige Forschungsarbeiten zu Anwendungen, bei denen ein realistischeres System Nicht-Gleichgewichtsbedingungen und Wärme- und Massenströmen ausgesetzt ist.

Contents

1 Introduction

Many phenomena in nature are fundamentally out of equilibrium. The corresponding physical systems are subject to fluxes of matter and energy to and from their environments, as well as chemical reactions therein, and they may violate mechanical, chemical, or thermal equilibrium conditions. A physical system is said to be in equilibrium if it is mechanically stable, is free of currents on average, and is invariant under time reversal. State variables have inherent fluctuations that do not disturb the macroscopic state near equilibrium but can be amplified far from equilibrium [1]. These are important indications of the qualitative differences between equilibrium and non-equilibrium situations. Some examples of non-equilibrium phenomena on the molecular scale include fluid flow in porous media and nanotubes [2], liquid evaporation[3], glass formation in liquids [4], and osmosis [5].

For studying non-equilibrium phenomena, a suitable extension of thermodynamics is needed. One of the goals of non-equilibrium thermodynamics is to determine the relation between the flux of some property to the gradient of conjugate variable that drive the flux. This allows for the representation of energy, momentum and mass transport equations [6]. In 1854, W. Thomson used thermodynamic concepts to treat irreversible phenomena. Later work by Onsager in 1931 [7, 8] led to the development of the classical theory of non-equilibrium thermodynamics based on reciprocal relations connecting the coefficients of proportionality between irreversible fluxes and thermodynamic forces [1, 9, 10].

Thermal gradients can create a variety of non-equilibrium phenomena and have many applications. Experimental studies have detected non-uniform temperature fields around the membranes of living cells [11], and it is possible to control the shape of the membrane by manipulating the temperature around it. Another application is the separation of ionic liquids as a solvent from other components like water [12].

Directed fluid flow is a major transport mechanism in porous media that can either be generated by pumps or emerge in response to a gradient of pressure. The pressure-flow relation and how it depends on the structure and geometry of the medium is an important question to be answered as it helps to optimize the medium and control the flow in relevant applications such as gas separation with metal organic frameworks (MOFs) [13, 14].

For studying phenomena such as the examples above, one needs a reliable simulation technique of a system that can exchange energy and particles with the environment. The standard method for simulation of closed systems have limitations in modeling open system conditions, necessitating the development and use of well-founded algorithms for efficient and accurate numerical simulations.

From a thermodynamic standpoint, most physical systems can be classified into three groups based on their interactions with their surroundings: 1. isolated systems that are unable to interchange matter and energy, 2. closed systems that allow the exchange of energy but not matter, 3. open systems that can exchange both matter and energy. The boundary conditions mimic the interaction of the system with its surroundings. There may be walls located at the boundaries, which close the system for the exchange of particles. Periodic boundaries are another choice, and are very well suited for the simulation of microcanonical and canonical ensembles. Another option are open boundaries to model a grand canonical ensemble. One method to simulate an open system is to employ a huge system as a universe with periodic boundary conditions and to consider a subvolume of this universe as an open system where particles can enter and exit. The drawback with this type of simulation is that it requires a very large reservoir (10-20 times larger than the considered open system [15]) to imitate grand canonical conditions and to eliminate finite size effects, which has a significant computing cost.

In multi-scale systems, often details are important in some regions and not important in others. The matter of considering or ignoring the details is determined by our point of view on the problem. When investigating the local features of a system in contact with large-scale reservoir, not all of the details need to be taken into account. As a result, it has proven to be advantageous to have simulation approaches that deal with problems locally, where the region of interest is resolved microscopically and is in equilibrium with a simplified, coarse-grained (CG) environment [16].

The method used in this thesis is the Adaptive Resolution Simulation (AdResS) technique, which provides a framework to model open systems with considering different resolutions in the system and the surroundings at lower computational cost (see chapter 2). This method has been tested in equilibrium in a range of applications [17–19] and in this thesis, studies on open

systems in non-equilibrium conditions are presented. Physico-mathematical models of open systems determine the guideline protocol for the simulation algorithms. For non-equilibrium conditions, they mostly consider the linear independent combination of reservoir actions and AdResS simulations are based on these principles. These studies are conducted using AdResS as well as full-resolution simulations, in which all particles are explicitly treated with all of their degrees of freedom. This was done in order to verify the computational process and its numerical applicability.

Another approach to lowering computational costs and paving the way for complex system simulations is to run molecular dynamics simulations on high-end general purpose graphics processing units (GPUs). This can bring an encouraging performance boost, but the transition from the usual sequential algorithm to the parallel algorithm must be made carefully to gain the theoretical performance advantage. HAL's MD package (HALMD) [20] is a molecular dynamics software which has been designed and written to run on GPUs, and ref. [21] shows that simulating a Lennard-Jones fluid on GPU in HALMD has an 80-fold speedup over sequential CPU simulations. This number has changed with newer generations of hardware both in GPUs and CPUs, and varies between 50 and 200 times faster in GPUs. Similar factors are obtained for the equivalance of one GPU to the numbers of CPU cores in parallel implementations [20]. The simulations in this thesis are all performed in HALMD on GPUs.

This thesis focuses on modeling open boundaries in non-equilibrium conditions, with a minimal computing cost, which is useful in a variety of applications. We have extended the AdResS method to simulate non-equilibrium conditions. We have studied an open system subjected to temperature gradients, demonstrating that the mathematical model of an open system in non-equilibrium is also well compatible with AdResS and produces the expected results. Then the applicability range is thoroughly examined, and a detailed mathematical formulation of the non-equilibrium conditions is presented (ch.4). Going further from the simulation of a heat flux in an open system to the simulation of a mass flux, we faced some challenges and chapter 5 is dedicated to explain different approaches we used to create a steady mass current in an AdResS setup, their problems and potential solutions.

The non-equilibrium conditions featuring a steady mass flux were studied for an application-relevant setup using full resolution simulations. We studied the fluid flow through regular bead packings as a model for nano porous media in periodic boundaries (ch.6). We also studied the same setup but with open boundaries (ch.7) with the AdResS method, where the original idea of chapter 4 works naturally.

Some of the results of this thesis have already been published in the following peer-reviewed articles for which I have implemented and conducted the simulations, analysed and interpreted

the data, and written some parts of the text.

[22] R. Ebrahimi Viand, F. Höfling, R. Klein and L. Delle Site, Theory and simulation of open systems out of equilibrium, *J. Chem. Phys.* **153**. 101102 (2020), Featured article.

[23] R. Klein, R. Ebrahimi Viand, F. Höfling and L. Delle Site, Nonequilibrium induced by reservoirs: Physico-mathematical model and numerical tests, *Adv. Theory Simul.* **4**, 2100071 (2021).

2 The Adaptive Resolution Simulation Technique

Multiscale phenomena are ubiquitous in nature, and studying them requires multiscale methods. All effort can be concentrated on the phenomena of interest by ignoring numerous unimportant details. Particles in such a system should be able to move freely between different regions with different properties. This is provided by the Adaptive Resolution Simulation (AdResS) technique which has been presented for nearly two decades and has evolved in a variety of ways. In the original form of AdResS [25, 26], the region of interest with high resolution is referred to as (AT) and it is linked to the coarse-grained region via a hybrid region denoted by (Δ). Particle resolution changes smoothly and continuously from all-atom to fully coarse grained levels. The transition function $w(x)$ in the Δ region controls this change of resolution, which avoids the abrupt change in particle interactions and thus the discontinuity. This region's length is typically smaller than other regions but greater than the interaction length to avoid direct interaction between coarse-grained and full-atomistic particles.

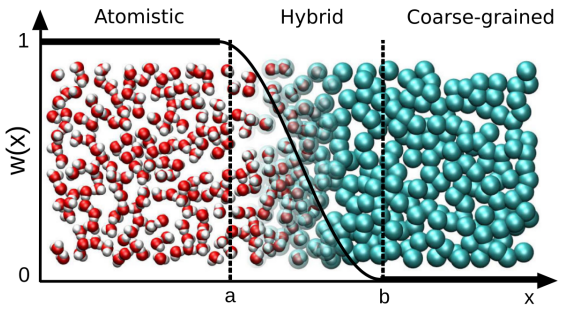

Figure 2.1: The original AdResS configuration. The box is divided into three regions. The high resolution region is depicted in the figure as the "Atomistic" region and is referred to as "AT" throughout this thesis. There exists a transition region referred to as Δ and a coarse grained region (CG) where the resolution is decreased. To change the resolution smoothly, the switching function $w(x)$ is used in the Δ region. Reprinted figure with permission from ref. [24].

Some of the system's properties are inconsistent as a result of this type of coupling. Although a thermostat can keep the temperature uniformly throughout the box, this is not true for the other parameters. The difference in resolution and, as a result, the mismatch in the number of degrees of freedom result in a difference in entropy. This results in a pressure difference, and the consequence of this pressure difference is a non-physical change in density caused only by this coupling of scales, which should be compensated for. There are two approaches to fixing this mismatch. One is based on manipulating the force and the other is based on manipulating the Hamiltonian.

A one-particle thermodynamic force is applied to fix the density in the original form of AdResS [25], which was force-based, whereas in Hamiltonian-based AdResS (H-AdResS), the free energy difference between the AT and CG regions is considered to compensate for the density difference. Both versions ensure that there is no barrier to particles passing from different regions, resulting in equilibrium between the regions of different resolution. They are, in fact, different technical expressions of the same balancing process [19]. More information on these two AdResS types, as well as a simplified version of the force-based one for dealing with open systems, is provided in the following subsections.

2.1 Force based AdResS

Particles feel different potentials in the AT and CG regions. For a system of N molecules made of n atoms with intramolecular interactions V^{int}, the Hamiltonians in the atomistic region (H_{AT}) and the coarse grained Hamiltonian (H^{CG}) are [19],

$$H^{AT} = \sum_{\alpha=1}^{N} \sum_{i=1}^{n} \frac{p_{\alpha i}^2}{2m_{\alpha i}} + V^{\text{int}} + \sum_{\alpha=1}^{N} V_{\alpha}^{\text{AT}}, \qquad V_{\alpha}^{AT} = \frac{1}{2} \sum_{\beta \neq \alpha}^{N} \sum_{ij}^{n} V^{\text{AT}} \left(|\mathbf{r}_{\alpha i} - \mathbf{r}_{\beta j}| \right), \tag{2.1}$$

$$H^{CG} = \sum_{\alpha=1}^{N} \frac{p_{\alpha}^2}{2m_{\alpha}} + V^{\text{int}} + \sum_{\alpha=1}^{N} V_{\alpha}^{\text{CG}}, \qquad V_{\alpha}^{CG} = \frac{1}{2} \sum_{\beta \neq \alpha}^{N} V^{\text{CG}} \left(|\mathbf{R}_{\alpha} - \mathbf{R}_{\beta}| \right). \tag{2.2}$$

In these equations, p is momentum, m is mass, $\mathbf{r}$ is particle position and $\mathbf{R}$ is the center of mass of the coarse grained particle. The subscripts i and α refer to atom and molecule indexes, respectively. V^{int} can have any form and is not important in our case.

When moving from one region to another, particles pass through the transition region Δ,

where the transition function $w(x)$ is felt. As a result, the final force between particles is [26]

$$\mathbf{F}_{\alpha\beta} = w(x_\alpha)\, w(x_\beta)\mathbf{F}^{AT}_{\alpha\beta} + \left(1 - w(x_\alpha)\, w(x_\beta)\right)\mathbf{F}^{CG}_{\alpha\beta}, \tag{2.3}$$

where $x_\alpha = \hat{e}_x \cdot \mathbf{r}_\alpha$ in which $\hat{e}_x$ is the unit vector along the x-axis. $\mathbf{F}^{AT}_{\alpha\beta}$ represents the total force exerted by the atoms of molecule β on molecule α due to the atomistic interactions and the force between the centers of mass of the coarse-grained particles is represented by $\mathbf{F}^{CG}_{\alpha\beta} = -\nabla V^{CG}(\mathbf{R}_\alpha - \mathbf{R}_\beta)$.

The thermostat and a position-dependent thermodynamic force $\mathbf{F}_{th}(x)$ keep the simulation box in global thermodynamic equilibrium. $\mathbf{F}_{th}$ compensates for pressure differences in the system to reach constant density ρ in the whole box and is calculated iteratively,

$$\mathbf{F}_{th}(x) = \frac{M}{\rho}\nabla P(x) \tag{2.4}$$

with M being the molecular mass.

2.2 Hamiltonian based AdResS

In the force-based AdResS, the force is defined everywhere in the box, but it is non-conservative in the Δ region [27, 28], so a global Hamiltonian cannot be defined. A well-defined Hamiltonian is required, such as in a Monte Carlo AdResS where the energy should be known everywhere [29]. This is one of the reasons for performing interpolation at the potential level. H-AdResS is a free energy compensation scheme that attempts to balances the missing free energy contributions of the AT region due to the loss of degrees of freedom in the coarse-grained region [30, 31]. The Hamiltonian includes the smooth transition function and is given by

$$H = \sum_{\alpha=1}^{N}\sum_{i=1}^{n}\frac{p_{\alpha i}}{2m_{\alpha i}} + \sum_{\alpha=1} N\left[w(x_\alpha)\, V^{\mathrm{AT}}_\alpha + (1 - w(x_\alpha))\, V^{\mathrm{CG}}_\alpha\right] + V^{\mathrm{int}}. \tag{2.5}$$

From this Hamiltonian, the force applied on ith atom of molecule α is calculated as

$$\begin{aligned}\mathbf{F}_{\alpha i} = &\sum_{\beta,\beta\neq\alpha}\left[\frac{w(x_\alpha) + w(x_\beta)}{2}\sum_{j=1}^{n}\mathbf{F}^{\mathrm{AT}}_{\alpha i,\beta j} + \left(1 - \frac{w(x_\alpha) + w(x_\beta)}{2}\right)\mathbf{F}^{\mathrm{CG}}_{\alpha i,\beta}\right] \\ &+ \mathbf{F}^{\mathrm{int}}_{\alpha i} - \left[V^{\mathrm{AT}}_\alpha - V^{\mathrm{CG}}_\alpha\right]\nabla_{\alpha i}\, w(x_\alpha).\end{aligned} \tag{2.6}$$

A drift term $\left[V_\alpha^{\mathrm{AT}} - V_\alpha^{\mathrm{CG}}\right] \nabla_{\alpha i} w(x_\alpha)$ appears in the force, coming from the energy differences and proportional to the gradient of transition function and this violates the Newton's Third Law. The fact that energy and force are defined everywhere in this scheme appears to be a plus, but calculating force from this smooth Hamiltonian has some mathematical issues, and the equation is ill-posed [28].

2.3 GC-AdResS for the simulation of open systems

AdResS's high efficiency, in simulating a system that exchanges energy and particles with another system, makes it a good candidate for modeling open systems. The *AT* region of AdResS can be treated as a high-resolution open system embedded in a larger, coarser reservoir of energy and particles. In AdResS, the *AT* region shows grand canonical (GC) behavior, which is formulated in the GC version of AdResS [32].

The Liouville equation describes the time evolution of the probability distribution of a system of particles and is normally used for closed systems in molecular dynamics (more details are given later in section 3.1), but Bergmann and Lebowitz developed a generalization of the Liouville equation for open systems in 1955 and later [33, 34]. The system in this mathematical model has impulsive interactions with one or more reservoirs, resulting in a transition from a state with M particles to a state with N particles. The reservoir's state remains unchanged after this transition. The reservoir's action (I) is formalized by a stochastic function that determines the probability of this transition as a result of interaction with the reservoir. Liouville's equation describes the time evolution of the probability distribution ($f(X_M, M)$) of a system of M particles

$$\frac{\partial f(X_M, M, t)}{\partial t} = -\{f(X_M, M, t), H(X_M)\} + I(X_M, f(X_N, N, t)), \tag{2.7}$$

where $\{.,.\}$ is the poisson bracket. This model assumes the linear sum of actions of different reservoirs, so the actions of different reservoirs will be added together. The BL model's principles can be properly translated into AdResS, and AdResS can be used to model open systems in and out of equilibrium.

2.4 Further simplifications of GC-AdResS

In ref. [35], an abrupt change in resolution was tested and shown to be accurate, the need for a smooth transition function in the Δ region was demonstrated to be ignorable. It was also tested separately and with the original smooth switching function that two-body interactions

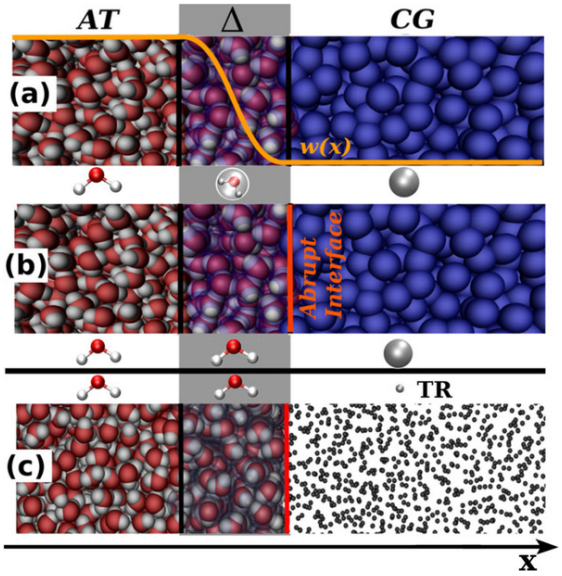

Figure 2.2: Representation of different types of AdResS. (a) The original idea of AdResS with a switching function to smooth the change of particle resolution. (b) An abrupt interface between high resolution and coarse grain region is employed. (c) The CG particles are replaced with non-interacting particles (tracers). Reprinted figure from ref. [17].

in the CG region can be removed and non-interacting particles used instead [36]. In ref. [17] a newer version of AdResS is presented that combines these two simplifications in modeling open systems. In this model, the transition function $w(x)$ is eliminated and the particles feel an abrupt change of identity instead of a smooth and continuous change as shown in part (b) of figure fig. 2.2. The Δ region in which the resolution changed smoothly is now filled with full resolution particles.

As shown in part (c) of figure fig. 2.2, it also replaces CG particles with point-like non-interacting particles (tracers), which significantly increases computational efficiency. The disadvantage of this computational efficiency is the emergence of numerical instabilities. Non-interacting particles enter the high resolution region (Δ) without any barriers, exactly as we want and expect, and then change to full resolution particles. Particles' new positions are determined by other particles and the net force exerted on them. This avoids being in very close vicinity to other particles. This is not the case for the newborn particles at the $CG-\Delta$ interface. The tracers do not interact with each other or with particles in the Δ and AT regions. When the newborn particles pass through the interface, they choose their new position blindly, and they may be located in an inappropriate location, very close to other particles, causing a strong repulsive force and instability. This problem is solved by considering a force value threshold in each direction that is greater than the maximum possible force. Forces with values greater than this threshold are truncated and will eventually relax in the following steps.

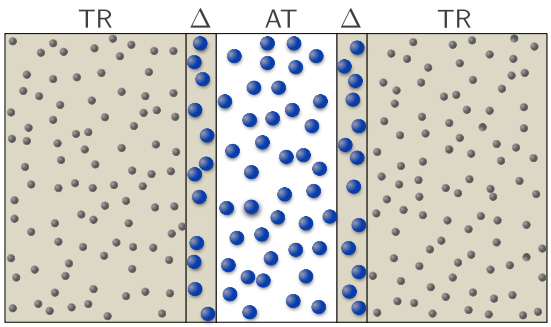

Figure 2.3: AdResS configuration illustration. Blue spheres represent full resolution particles, while small gray dots represent tracers. Thermostat is used on the colored areas. Reprinted from ref. [22], with the permission of AIP publishing.

This is not very likely and accounts for about 1% of total interactions in each time step, but it is crucial to avoid instabilities. We will use this variation of AdResS with an abrupt change in resolution and non-interacting particles in the CG region, which we will refer to as the TR region from now on in this thesis.

2.5 Simulation process

In order to simulate a physical system with AdResS, the simulation box should be divided into different regions and the reservoir (Δ and TR regions) is kept at the desired temperature using a suitable thermostat. When passing through the boundary of the Δ and TR regions, particles are converted to tracers and vice versa. Particle forces in the transition region should be checked to ensure that they do not exceed the threshold value. Thermodynamic Force $\mathbf{F}_{\text{th}}$ of eq. (2.4) should be calculated but local pressure is not easily accessible. For a constant ρ_0 in the simulation domain, in the first estimation, the local pressure dependent on the density is $p(\rho(x), T) \approx p_0 + 1/(\rho_0 \chi_T)(\rho_0 - \rho(x))$, where χ_T is the isothermal compressibility. Using this approximation, eq. (2.4) can be rewritten as

$$F_{\text{th}}^{k+1}(x) = F_{\text{th}}^{k}(x) - \frac{M}{\rho_0^2 \chi_T} \nabla \rho^k(x). \tag{2.8}$$

This formula is not directly dependent on pressure and is easier to implement comparing to eq. (2.4). Alternative approach is considering the fact that the potential energy $\phi(x)$ is uniquely determined by the equilibrium density [37]. The number density can be approximated by its

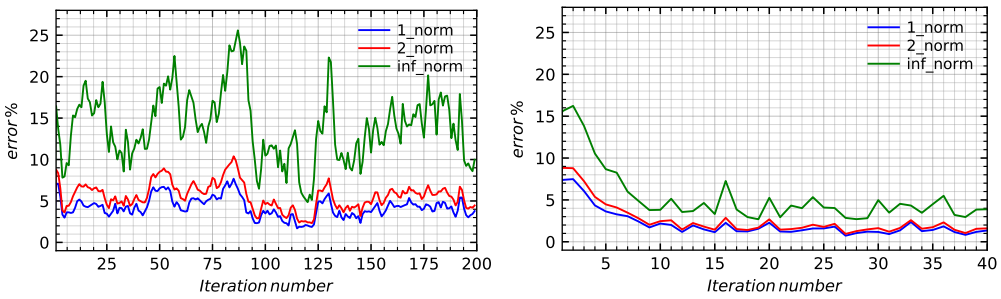

Figure 2.4: Comparison of convergence of thermodynamic forces for eq. (2.8) (left) and eq. (2.12)(right). The x-axis is different in two plots.

ideal gas expression as

$$\rho(x) \propto \exp(-\frac{1}{k_B T}\phi_{\text{th}}(x)), \tag{2.9}$$

so the corresponding external potential is

$$\phi_{\text{th}}(x) \propto -k_B T \ln(\rho(x)). \tag{2.10}$$

In each iteration, the potential ϕ_{th}^k and density ρ^k may differ from the target potential ϕ_{th}^0 and target constant density ρ^0, ($\phi_{\text{th}}^0 = \phi_{\text{th}}^{k+1} = \phi_{\text{th}}^k + A(x)$), so $A(x)$ will be:

$$A(x) = \phi_{\text{th}}^0 - \phi_{\text{th}}^k = k_B T \ln\left(\frac{\rho^k(x)}{\rho^0(x)}\right) \tag{2.11}$$

For interacting fluids, the potential can be approximated iteratively as

$$\phi_{\text{th}}^{k+1}(x) = \phi_{\text{th}}^k(x) + k_B T \ln\left(\frac{\rho^k(x)}{\rho_0(x)}\right), \tag{2.12}$$

and the thermodynamic force is calculated as the gradient of this potential, $\mathbf{F}_{\text{th}}(x) = -\nabla\phi_{\text{th}}(x)$. The latter formula converges faster than eq. (2.8) as shown in fig. 2.4 and we used it for all the AdResS simulations through this thesis.

The initial configuration of the fluid is exposed to the thermostats, and other AdResS elements such as species change and particle interaction are applied, and simulation is run without any external force at first. Using the resulting density profile and taking into account the target density profile and temperature, the new force and potential to reach the target density are calculated using eq. (2.12). Another simulation begins by applying the calculated $\mathbf{F}_{\text{th}}$ to the previous simulation's final configuration. This process of correcting the required force

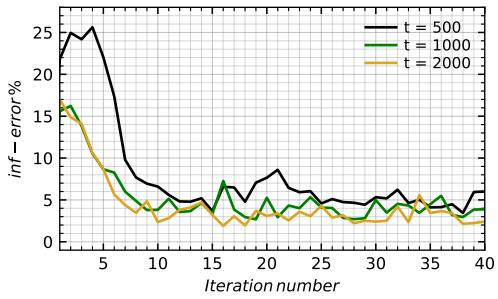

Figure 2.5: Comparison of convergence of thermodynamic forces for different simulation times. The infinity norm of density does not show a significant improvement with increasing simulation time.

is repeated until the density error is within the prescribed tolerance. The converged $\mathbf{F}_{\text{th}}(x)$ value is calculated once and is then used in the main simulation. The typical number of iterations required to achieve convergence is around 30–40, but this can vary depending on the state of the liquid and the size of the simulation. For a system of 12150 particles with $T = 1.6k_B/\varepsilon$ and in $\rho = 0.3\sigma^{-3}$, the convergence was tested for $t = 1000\tau$ with thermodynamic force and potential calculated by eq. (2.12) and with eq. (2.8). This was done by comparing the $\mathbf{L}^p$ distances between the current and the target densities in a set of grid points (x_i) in the space. The first and second norms are $\|\rho(x) - \rho_0(x)\|_p = \left(\sum_{i=1}^{n} |\rho(x_i) - \rho_0(x_i)|^p\right)^{1/p}$ with $p = 1, 2$ and the infinity norm is $\|\rho(x) - \rho_0(x)\|_\infty = max|\rho(x_i) - \rho_0(x_i)|$. As previously indicated, eq. (2.12) converges after 30 steps, which is considerably faster than the other formula, where the error is still approximately 5 percent after 200 steps as demonstrated in fig. 2.4.

Different parameters can influence convergence, and we investigated the role of simulation time, as shown in fig. 2.5. When the simulation time is increased from 500τ to 1000τ, the number of iterations required for convergence decreases, but increasing the simulation time further does not change the convergence and does not decrease the error.

To check if any spatially adaptive molecular resolution technique is subjective for modeling open systems and has realistic physical meaning, we need to make sure that the method produce the same properties in AT region as the all-atom simulation. Some criteria that need to be met are as follows [38]:

- During the simulation, the system should reach equilibrium and have a flat density and temperature all over the box within a certain tolerance. This is required because the reservoir in the BL model is designed such that its thermodynamic state is unaffected by the AT region. This is accomplished by using a thermostat to maintain temperature and thermodynamic force to control the density.
- In the thermodynamic limit, the system needs to display the typical characteristics of

a grand canonical ensemble. At any time t, the interaction energy of full resolution particles in the AT region with particles in the reservoir, (which reduces to the Δ region as tracers are non-interacting) $U(t)_{\mathrm{AT}-\Delta}$, should be negligible comparing to the interaction energy of the particles in AT region with themselves $|U(t)_{\mathrm{AT}-\mathrm{AT}}|$.

$$\delta(t) = \frac{|U(t)_{\mathrm{AT}-\Delta}|}{|U(t)_{\mathrm{AT}-\mathrm{AT}}|} \ll 1 \tag{2.13}$$

- The probability distribution function of the number of particles in the AT region should be Gaussian and equal to the all-atom simulation.
- Finally, the detailed structural properties should agree with the full-atom simulation, as determined by the radial distribution function $g(r)$ in the AT region.

An example of such validation can be found later in section 4.1.7.1.

3 Molecular Dynamics Simulations

Molecular dynamics simulation is a powerful tool for investigating classical many-body problems. It is the numerical solution to Newton's equation of motion for a system of classical particles. Particle configurations and their time evolution are then used to obtain observables, e.g., thermodynamic quantities and material constants.

The fundamentals of statistical mechanics is explained in the following section before going deeper into the methods and materials, and giving an explanation of the massively parallel programming technique, which is the power of the HAL's MD package [20, 21] used in this thesis.

3.1 Liouville dynamics

For an isolated system of N particles of mass m in a box with volume V, the position of the ith particle is indicated with $\mathbf{r}_i$ and its momentum is shown with $\mathbf{p}_i$. In phase space of $(\mathbf{r}^N, \mathbf{p}^N) \in \mathbb{R}^{6N}$, the Hamiltonian of the system is defined as $H(\mathbf{r}^N, \mathbf{p}^N) = T(\mathbf{p}^N) + U(\mathbf{r}^N)$, where T is the kinetic energy and U is the potential energy of the system. The Hamiltonian equations of motion are

$$\dot{\mathbf{r}}_i = \frac{\partial H}{\partial \mathbf{p}_i}, \qquad \dot{\mathbf{p}}_i = -\frac{\partial H}{\partial \mathbf{r}_i}. \tag{3.1}$$

An ensemble is a collection of phase points in phase space that can result in the same macroscopic properties. The phase space probability density $f(\mathbf{r}^N, \mathbf{p}^N, t)$ allows us to determine the statistical properties of all macroscopic observables that are dependent on particle positions and momenta, and so the time evolution of this probability density contains detailed information on the dynamics of the system. Phase space trajectories do not merge or split, according

to the Liouville theorem, and the probability density is conserved over time [39]:

$$\frac{df(\mathbf{r}^N, \mathbf{p}^N, t)}{dt} = 0. \tag{3.2}$$

Positions and momenta are time dependent, and the total time derivative is expressed as

$$\frac{\partial f}{\partial t} + \sum_{i=1}^{N} \left(\dot{\mathbf{r}}_i \frac{\partial f}{\partial \mathbf{r}_i} + \dot{\mathbf{p}}_i \frac{\partial f}{\partial \mathbf{p}_i} \right) = 0. \tag{3.3}$$

By inserting eqs. (3.1) and (3.3) into eq. (3.2) and using the Poisson bracket definition, we get $\partial_t f = \{H, f\}$. Considering the Liouville operator, that is a linear differential operator on the phase space $\mathscr{L} \equiv i\{H, \cdot\}$, leads to $\partial_t f = -i\mathscr{L} f$. The formal solution to this equation is

$$f(\mathbf{r}^N, \mathbf{p}^N, t) = \exp(-i\mathscr{L} t) f(\mathbf{r}^N, \mathbf{p}^N, 0). \tag{3.4}$$

Any observable property $A(\mathbf{r}^N(t), \mathbf{p}^N(t))$ of the system which depends on the phase space variables has a temporal evolution that is connected to the evolution of the phase space probability density. The observable is not directly dependent on time, although it does change over time as the system progresses through phase space:

$$\frac{dA}{dt} = \sum_{i=1}^{N} \left(\dot{\mathbf{r}}_i \frac{\partial A}{\partial \mathbf{r}_i} + \dot{\mathbf{p}}_i \frac{\partial A}{\partial \mathbf{p}_i} \right) = i\mathscr{L} A, \tag{3.5}$$

and the solution is

$$A(t) = A(\mathbf{r}^N(t), \mathbf{p}^N(t)) = \exp(i\mathscr{L} t) A(0). \tag{3.6}$$

The integration of the equation of motion is used to follow the motion of the particles. To achieve this, the macroscopic time interval $[0, t]$ is divided into n discrete intervals of length Δt [39],

$$\exp(i\mathscr{L} t) = \left[\exp(i\mathscr{L} \Delta t)\right]^n. \tag{3.7}$$

After each interval, new positions and momenta are calculated by discretizing and solving the equation of motion. This will cause a velocity computation error, and then an energy drift. Because many physical systems have continuous potentials, the integration technique must be carefully chosen and should be symplectic to ensure that the total energy does not increase and remains constant on average.

The Liouville operator is made up of two different shifts in phase space, $i\mathscr{L} = i\mathscr{L}_{\mathbf{r}} + i\mathscr{L}_{\mathbf{p}}$, where

$$i\mathscr{L}_{\mathbf{r}} = \frac{\mathbf{p}}{m}\frac{\partial}{\partial \mathbf{r}}, \qquad i\mathscr{L}_{\mathbf{p}} = \mathbf{F}\frac{\partial}{\partial \mathbf{p}}. \tag{3.8}$$

As a result, both positions and momenta are displaced in phase space after the interval Δt. The order of these shifts is important and $e^{i\mathscr{L}} \neq e^{i\mathscr{L}_{\mathbf{r}}} e^{i\mathscr{L}_{\mathbf{p}}}$ as $\mathscr{L}_{\mathbf{r}}$ and $\mathscr{L}_{\mathbf{p}}$ do not commute. The error of different combinations of shifts in phase space can be calculated using the Baker–Campbell–Hausdorff formula

$$Z = X + Y + \frac{1}{2}[X, Y] + \frac{1}{12}([X, [X, Y]] + [Y, [Y, X]]) + ..., \tag{3.9}$$

where $[X, Y] = XY - YX$ and Z is the solution to the equation $e^X e^Y = e^Z$.

For the choice of $e^{i\Delta t\mathscr{L}_{\mathbf{p}}} e^{i\Delta t\mathscr{L}_{\mathbf{r}}}$, the discretisation error of $\mathscr{L}$ would be of the order $\mathscr{O}(\Delta t)$. The error is reduced by using the following approximation for $i\mathscr{L}$, known as velocity-verlet algorithm:

$$\exp\left(i\mathscr{L}_{\mathbf{p}}\frac{\Delta t}{2}\right)\exp\left(i\mathscr{L}_{\mathbf{r}}\Delta t\right)\exp\left(i\mathscr{L}_{\mathbf{p}}\frac{\Delta t}{2}\right) = \exp\left(i\mathscr{L}\Delta t + \mathscr{O}(\Delta t^3)\right). \tag{3.10}$$

This indicates that position and momentum are displaced in phase space in three successive stages. A displacement in momentum is followed by a displacement in position and is completed by another displacement of momentum. This approximation of the Liouville operator, conserves energy within a reasonable error range. The scheme is symplectic by construction as a sequence of shifts, and thus it generates stable trajectories in phase space.

Other alternative approximations include the position-verlet method, which has two shifts in position and one shift in momentum. It has the same error as velocity verlet, however it needs more force calculations at least in sampling steps. Other decomposition choices are also suggested in [40] and the efficiency of these algorithm were investigated in a student project in which I had a contribution. Although there are more efficient approximations, the velocity-Verlet approach is the most widely used, and we used it in all of our simulations in HALMD.

The integration procedure in each time step and for each particle, according to eq. (3.10), is made up of sequential steps given in algorithm 1:

Algorithm 1 Velocity-verlet algorithm

1: $\mathbf{p}_i \leftarrow \mathbf{p}_i + (\Delta t/2)\mathbf{F}_i$ ▷ Estimating the momentum after $(\Delta t/2)$ using the current force
2: $\mathbf{r}_i \leftarrow \mathbf{r}_i + (\Delta t/m)\mathbf{p}_i$ ▷ Predicting the position after (Δt) using the new momentum
3: $\mathbf{F}_i \leftarrow \mathbf{F}_i^{\text{new}}$ ▷ Updating the force because the positions changed in the previous step
4: $\mathbf{p}_i \leftarrow \mathbf{p}_i + (\Delta t/2)\mathbf{F}_i$ ▷ Using this updated force to finalize the integration of momentum

3.2 Parallelization with GPU

Molecular dynamics simulations require a large number of floating-point instructions to be completed in a reasonable amount of time. This massive number of instructions and calculations can severely limit the number of particles that can be considered in the simulation, necessitating a shift to high-performance computations in order to speed up calculations and model larger systems of particles in the same amount of time.

The performance of central processing units (CPUs) has been improving for the past decades, allowing them to perform more floating point operations per second, but the rate of growth has slowed since 2003, and thus most software written sequentially and optimized for CPUs will not improve significantly [41]. Multicore CPUs were used to execute programs parallel on multiple cores in order to boost efficiency. A multicore processing system is essentially a single processor on a single chip with multiple execution cores. An alternative is massive parallelisation of microprocessors on high-end general purpose graphics processing units (GPUs), in which a large number of execution threads work together to finish a task. A GPU consists of about 100 so-called Streaming Multiprocessors (SMs), each of them can operate 128 floating-point operations in parallel. The ratio of peak floating point operations between GPUs and multicore processors is about 10 [41]. Software for GPUs should be developed in a way that allows for parallel executions. This means the program should be written as a sequence of tasks that can be completed in parallel, rather than sequentially, as is typical with sequential programming.

GPUs have a hierarchical memory design. These memories differ in terms of bandwidth (the rate at which data can be read from or written to) and latency (the time it takes from initiating a request for a byte in memory until it is retrieved by a processor). Register is the fastest memory and private to each single thread. GPU caches include L1 cache stored on-chip and L2 cache stored off-chip. The L1 cache is shared by threads of the same multiprocessor and is typically relatively small. It has a high bandwidth as well as a low latency. L2 cache is in the next level of hierarchy, connected to all multiprocessors, and is slower than L1 cache. It is connected to the global memory which is GPU's main memory. The global memory has lower bandwidth and high latency and is accessible to all the threads. A problem with thread communication is

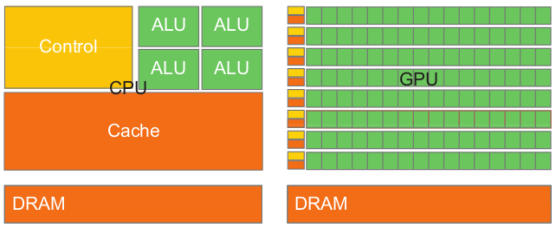

Figure 3.1: A simplified version of the CPU and GPU designs. There is a big memory cache in the CPU while there are small caches for each multiprocessor of threads in GPU. The control unit is a big part of CPUs, but this is not so in GPUs . Reprinted figure from [41] with permission from Elsevier.

that the order, in which the threads are processed, is not defined (more precisely, the order of thread blocks), so typically communication via global memory uses several kernel calls and requires synchronisation barriers. The L2 cache and, e.g., atomic locking of the memory access, have been introduced to mitigate these limitations, but we do not have any control over it. We have control over global memory, which exchanges data with CPU memory. We can also explicitly allocate and manage the shared memory, which threads of a multiprocessor can access and communicate with [42, 43]. Among the mentioned memory, the only persistent memory across kernel calls is the global memory.

A code can be processed in parallel by a central logic in a multi-core CPU, which can be complex needs complex instructions and branch predictions. There should be a large cache memory for the memory access of this cores. A limiting issue is memory bandwidth. GPUs have a rate that is ten times higher, making it difficult to compete with them, although CPUs have been improved either.

In GPUs, while some threads take longer to accomplish their tasks, other threads execute a greater number of instructions and do not have to wait for the long-running threads. CPUs, on the other hand, have focused on increasing the speed of single executions at the expense of large memory caches and increased power consumption.

As a result, applications that are ideal candidates for parallel programming usually process a lot of data, demand a lot of computation in each iteration, or execute a lot of iterations on the data. Aside from that, the CPU is a fine choice. We deal with such a vast number of particles in molecular dynamics that each of them can be handled by a single thread and the numerically intensive calculations can be performed in parallel on GPUs.

The Compute Unified Device Architecture (CUDA) programming interface can be used to access GPUs for scientific programming. In Fig. 3.2 the structure of the GPU is shown. The thread execution manager distributes the threads in a number of multiprocessors. Each multiprocessor contains a number of threads shown in green. Threads of each multiprocessor

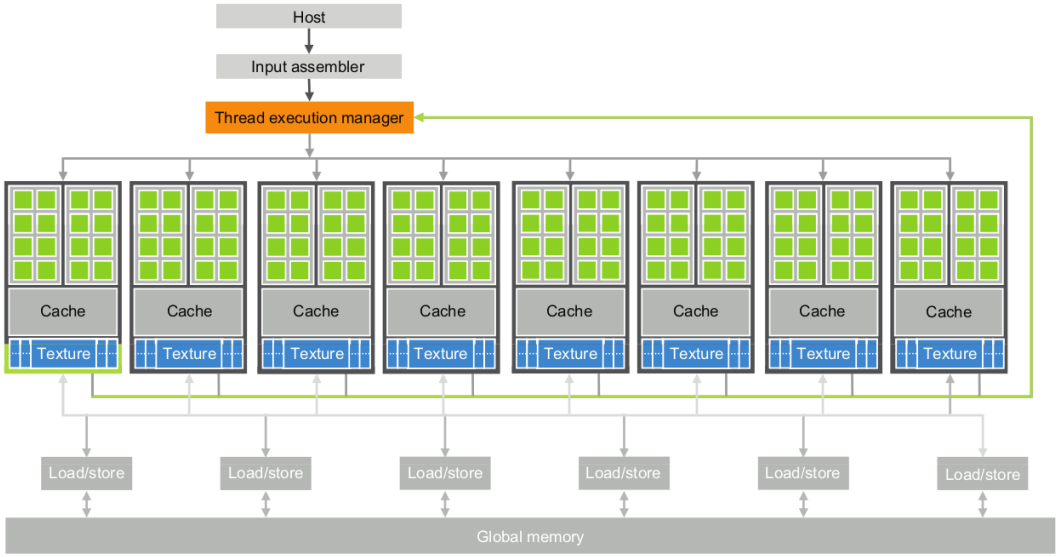

Figure 3.2: Architecture of a CUDA-capable GPU. Reprinted figure from [41] with permission from Elsevier.

share the same control logic and memory cache. The multiprocessors are in contact with a global memory to exchange data with.

The host (CPU) and GPU devices coexist in a CUDA code. The code begins on the host side and then calls kernel functions which are executed by many GPU threads in parallel. When a kernel is launched, a grid of threads is created, and when all of the threads have completed their tasks, such as updating all of the particle positions and velocities, the grid terminates.

The GPU-implemented code in HALMD can speed up a Lennard-Jones fluid by up to 80 times [21] as compared to a serial CPU implementation. This has changed over years and the speed up is now between 50 to 200 times for different generations of hardwares. This enables the simulation of systems with more particles and over longer times.

Calculating properties which are needed every MD step or in some intervals, such as temperature and centre-of-mass velocity need many executions. The parallel reduction algorithm on GPU is used to do this calculations efficiently. It typically refers to an algorithm which performs a mathematical operation such as summation on the elements of an array, producing a single result. It uses the multiple thread blocks in a GPU to reduce a small portion of the array. A tree based reduction is used inside each thread block [44] and shared memory is used to achieve communication among threads of the same block and synchronization among them.

A small portion of the array is read from the global memory by each thread and stored into the

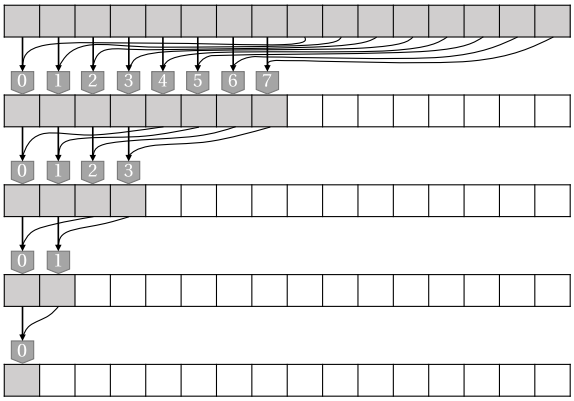

Figure 3.3: Parallel reduction operations are done in different steps and is continued until a single result is obtained.

shared memory. The array is then reduced in the shared memory which means the operations are performed on the pairs of elements within each thread block. The result is then stored in the shared memory leading to halved array size. The process is repeated recursively by several kernel calls, until a single result is obtained as shown in fig. 3.3.

3.3 Molecular dynamics algorithm

In a MD simulation, particles are usually assigned initial velocities from the Maxwell distribution according to the desired temperature. The initial coordinates are chosen to be within the defined simulation box. The integrator tracks the particles' movements and updates the particle information at each step. A system state comprises data arrays for position, velocity, mass, force and chemical species of each particle.

When the positions of particles are updated, the values of the interaction potential of the particles change, and the force must be updated as well. Force calculation is the most computationally expensive part of a molecular dynamics simulation. A verlet neighbor list is used for each particle to lower this cost by book keeping of its neighbors within a defined radius. After the force has been updated, the process continues with finalizing the integration and the velocity is updated once more in this stage. Calculation of macroscopic properties such as temperature, pressure, and so on, occurs after the finalize step as depicted in the flowchart 3.4.

In order to control the temperature of the system, the integrator can include some additional rules for updating velocities. A number of thermostats utilized in this thesis are discussed in the following section.

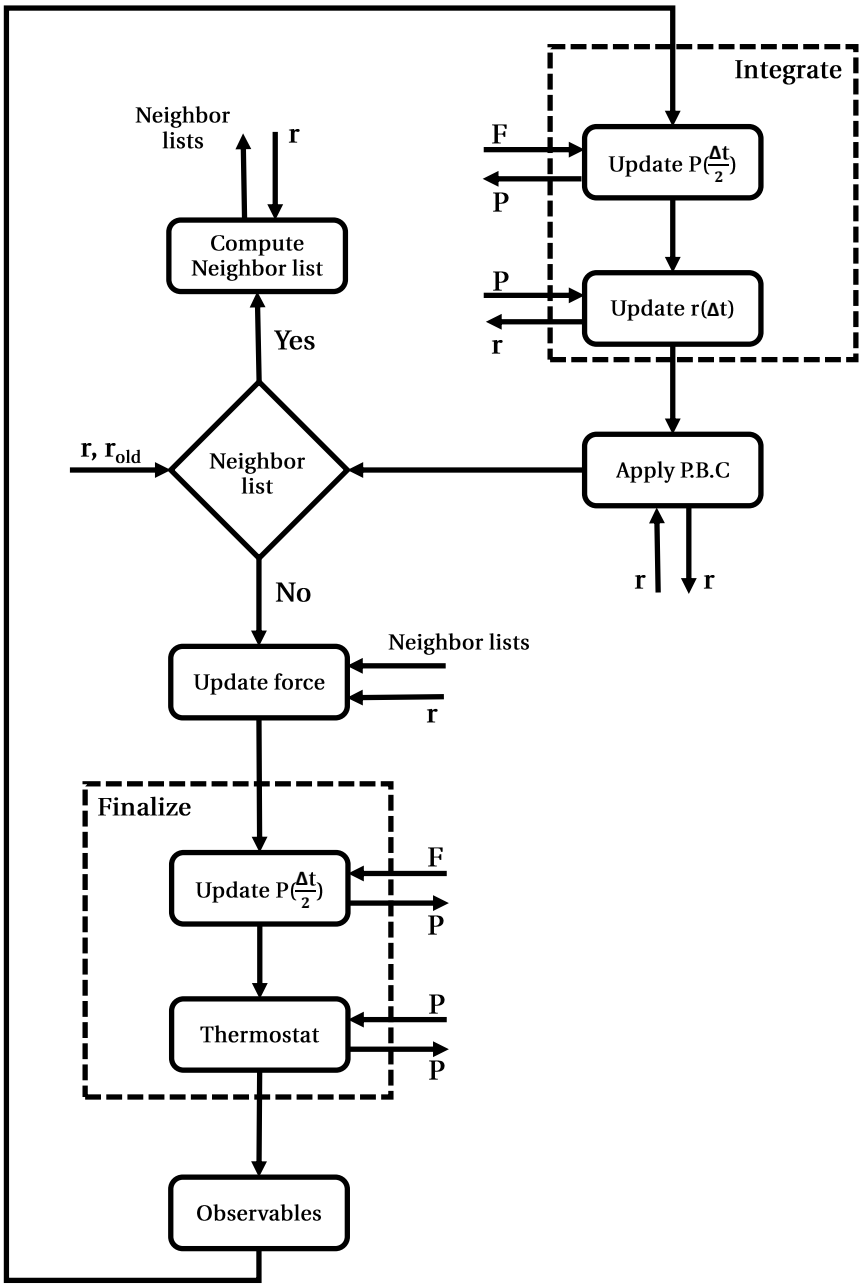

Figure 3.4: The standard molecular dynamics algorithm.

3.4 Thermostats

Many physical experiments are done at a prescribed temperature. Temperature is a measure of the average kinetic energy of the particles in a system. A a result, the best way to control the temperature in the system is to manipulate the velocities during or after the integration step. This allows us to generate a statistical ensemble at a fixed temperature, for example, a canonical ensemble.

A variety of thermostat methods are available to add and remove heat during a MD simulation, and they all modify the dynamics of the system. Among them, some cause a change of net momentum, while others control the temperature while conserving momentum [45, 46]. Thermostats can be local or global. Global thermostats dissipate energy uniformly across the system, whereas local thermostats do so in a spatially localized fashion [45].

The following subsections describe a number of thermostats that are implemented in HALMD package and used in this thesis. The net momentum fluctuates about zero in the first two thermostats, while the others conserve or adjust the momentum's value as needed.

3.4.1 The Andersen thermostat

The Andersen thermostat, introduced in 1980 [47], assigns random velocities to each particle in random intervals, using the Maxwell-Boltzmann distribution,

$$f_{\mathrm{MB}}(v) = \sqrt{\frac{m}{2\pi k_B T}} \exp\left(\frac{-mv^2}{2k_B T}\right), \tag{3.11}$$

where k_B is the Boltzmann constant. "Collisions" with the heat bath occur infrequently and on randomly picked particles in this thermostat. This leads to a local dissipation of energy. Because successive collisions are uncorrelated, the distribution of time intervals between two stochastic collisions $P(t)$ takes the shape of an exponential distribution

$$P(t) = \Gamma \exp(-\Gamma t), \tag{3.12}$$

$P(t)$ is the probability that the next collision will take place in the interval $[t, t+\Delta t]$ and $\Gamma = 1/\Delta s$.

The velocity-Verlet algorithm coupled to the Andersen thermostat is a modification to the finalize step of the algorithm in each step as given in algorithm 2. Each CUDA thread is assigned to a single particle in the GPU version, and the integration is done in parallel. The

integration is then finalized in parallel, either by updating the velocities at random or normally by using Newton's equation.

Algorithm 2 Andersen thermostat

1: **for all** particles i **do** ▷ update position and velocity of all particles in parallel
2: $\quad \mathbf{p}_i \leftarrow \mathbf{p}_i + (\Delta t/2)\mathbf{F}_i$
3: $\quad \mathbf{r}_i \leftarrow \mathbf{r}_i + (\Delta t/m)\mathbf{p}_i$
4: **end for**
5: **for all** particles i **do** ▷ finalize the integration
6: $\quad$ Update $\mathbf{F}_i$
7: $\quad$ **if** $\mathscr{U}(0,1) \leq \Gamma \Delta t$ **then**
8: $\quad\quad \mathbf{p}_i \leftarrow m\mathscr{N}(0, \sqrt{k_B T/m})$ ▷ random velocity
9: $\quad$ **else**
10: $\quad\quad \mathbf{p}_i \leftarrow \mathbf{p}_i + (\Delta t/2)\mathbf{F}_i$ ▷ deterministic step
11: $\quad$ **end if**
12: **end for**

3.4.2 The Maxwell-Boltzmann thermostat

This thermostat is a global stochastic thermostat and is a special case of the Andersen thermostat introduced in previous section. Unlike Andersen thermostat, the time interval between random rescaling of each particle's velocities is fixed here and after each s steps, all particles are assigned Gaussian random velocities according to eq. (3.11). The coupling rate of the thermostat is $\Gamma = \frac{1}{s\Delta t}$.

The Maxwell-Boltzmann thermostat has the same algorithm as algorithm 2 with the line 6 replaced by:

if $t \mod s == 0$ **then**
$\quad$ ...,

where t is the time step.

3.4.3 Non-equilibrium extensions of the Maxwell-Boltzmann thermostat

Previous thermostats changed the velocities to a random distribution with a zero mean value, preventing the center of mass of the particles from moving. In non-equilibrium systems with particle flows, we have to make sure that the mass flux is not suppressed by the thermostat's action and that the thermostat conserves the local momentum. The temperature on these thermostats is set so that the particle's center of mass velocity prior to the update is preserved.

As a simple implementation of a global, momentum conserving thermostat, we suggest taking

Algorithm 3 Velocity conserving MB and pump algorithms

1: $\mu \leftarrow 0$ $\quad \mu \leftarrow input$
2: **for all** particles i **do**
3: $\quad \mathbf{p}_i \leftarrow \mathbf{p}_i + (\Delta t/2)\mathbf{F}_i$
4: $\quad \mathbf{r}_i \leftarrow \mathbf{r}_i + (\Delta t/m)\mathbf{p}_i$
5: **end for**
6: $\mu \leftarrow \mu + \mathbf{p}_i/m$ $\quad$ – – – – – $\quad \triangleright$ μ is calculated in MB and not in pump
7: **for all** particles i **do**
8: $\quad$ Update $\mathbf{F}_i$
9: $\quad$ **if** $t \mod s == 0$ **then**
10: $\quad\quad \mathbf{p}_i \leftarrow m\mathcal{N}(\mu, \sqrt{k_B T/m})$
11: $\quad$ **else**
12: $\quad\quad \mathbf{p}_i \leftarrow \mathbf{p}_i + (\Delta t/2)\mathbf{F}_i$
13: $\quad$ **end if**
14: **end for**

the center of mass velocity of all particles prior to re-assignment and shifting the new center of mass velocities accordingly.

Thermalization is performed by combining the Maxwell-Boltzmann distribution of velocities and the velocity Verlet algorithm, like section 3.4.2, but keeping the center of mass velocity of all particles and shifting the new random velocities according to it. This implies that the random velocities should come from a Gaussian distribution with a non-zero mean value, v_{cm} for each component,

$$v \sim \mathcal{N}\left(v_{cm}, \sqrt{k_B T/m}\right). \tag{3.13}$$

A pump-like thermostat was another sort of integrator employed in this thesis. The goal is to enforce a mass flux in the system by manipulating the velocity of particles in a part of box. For the pump, the Maxwell-Boltzmann thermostat 3.4.2 is modified to shift the freshly generated random velocities of particles to a prescribed velocity, rather than the previously determined center of mass velocity. This helps to create a synthetic mass flux in the system as determined by us, not by the system. The algorithm for these two types of thermostats is presented in algorithm 3. The differences in the pump algorithm is indicated by the red text. The velocity conserving MB thermostat should calculate the center of mass velocity μ, so it is set to zero before the integration and updated after the momentum updates. The value of μ in the pump, on the other hand, is determined at the beginning and remains constant.

The summation of particle velocities in line 6 of the algorithm 3 is performed on GPU utilizing a parallel reduction scheme. Other system properties are also calculated in each MD step if

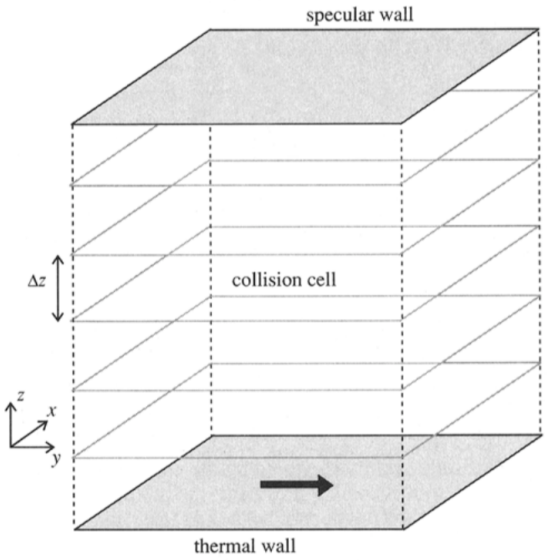

Figure 3.5: A schematic of a simulation box divided into a number of collision cells appropriate for DSMC and MPC thermostats. For this specific system, the collision cells are located on top of each other in the z direction, as it is simulating a fluid bounded in this direction by two walls, but there may be a number of cells needed in the other two directions as well for other simulations. Figure reproduced from [55], with the permission of AIP Publishing.

needed, using parallel reduction to speed up the calculations [21, 48]. It's worth noting that, the enforced mass flux of pump, can be also created by a custom flow as suggested in [49] and tested in this thesis later in section 5.3.

3.4.4 Lowe-Andersen thermostat

A local momentum conserving thermostat known as Lowe-Andersen [50, 51] is used in this thesis. Prior to presentation of this thermostat in 1999, a number of other momentum conserving thermostats where presented, like Dissipative Particle Dynamics (DPD) thermostat [52, 53], which updates pairs of neighboring particles together and assigns the new velocity such that their center of mass momentum does not change. Another technique to conserve momentum is Direct Simulation Monte Carlo (DSMC) [54, 55], which divides the space into a number of cells and selects pairs of particles from these cells to update the momentum. An illustration of these cells are shown in fig. 3.5. This approach is extended in Multi Particle Collision (MPC) dynamics [56] to update the position of each particle individually, but sets the new velocity to be along the cell's center of mass velocity instead of a pair's to increase efficiency.

The Lowe-Andersen thermostat combines the ideas of Andersen section 3.4.1 and DPD thermostats. The procedure is similar to Andersen's methodology, but instead of changing the

velocity of individual particles, it changes the relative velocity of pairs of particles separated at most by a distance R_T to ensure the locality of momentum conservation.

The bath collision involves selecting a new relative velocity for the two particles based on the Maxwellian distribution of relative velocities. This operation is only performed on the component of the relative velocity parallel to the connecting line of particle centers to conserve angular momentum. In addition, the new relative velocity is imposed in such a way that linear momentum is preserved. In the event of a successful pair selection and collision with a heat bath, the new velocities of the two selected particles will be

$$\begin{cases} \mathbf{v}_1^* = \mathbf{v}_1 + (M/m_1)\,(\lambda - (\mathbf{v}_1 - \mathbf{v}_2)\cdot\hat{\sigma}_{12})\,\hat{\sigma}_{12}, \\ \mathbf{v}_2^* = \mathbf{v}_2 - (M/m_2)\,(\lambda - (\mathbf{v}_1 - \mathbf{v}_2)\cdot\hat{\sigma}_{12})\,\hat{\sigma}_{12} \end{cases} \tag{3.14}$$

In this equations $\hat{\sigma}_{12}$ represents the unit separation vector, $M = m_1 m_2/(m_1+m_2)$ is the reduced mass, and λ denotes a Gaussian random number with a mean of zero and a variance $k_B T/M$. We discovered that the original Lowe-Andersen thermostat, which conserves both linear and angular momentum, does not yield the precise target temperature. The error is small enough to be ignored, but by giving up angular momentum conservation, which is unnecessary if one is working with a cuboid simulation box, the target temperature is matched more accurately. The new velocities in this variant is as follows

$$\begin{cases} \mathbf{v}_1^* = \mathbf{v}_{cm} + (M/m_1)\lambda, \\ \mathbf{v}_2^* = \mathbf{v}_{cm} - (M/m_2)\lambda. \end{cases} \tag{3.15}$$

The algorithm that we used is presented below, and more details and a comparison between our and the original algorithm can be found in the appendix A.

3.5 Potential and force fields

For the simulation a fluid, we need two types of forces. A brief description of each is provided below.

3.5.1 Interaction potential

The Lennard-Jones model is the paradigm of a simple fluid and works well for noble gases as well as spherical, uncharged molecules like methane. The Lennard-Jones pair potential for

Algorithm 4 Lowe-Andersen thermostat algorithm

for all particles i **do**
  $\mathbf{p}_i \leftarrow \mathbf{p}_i + (\Delta t/2)\mathbf{F}_i$
  $\mathbf{r}_i \leftarrow \mathbf{r}_i + (\Delta t/m_i)\mathbf{p}_i$
end for
for all particle pairs $(i, i+1)$ **do** ▷ each CUDA thread deals with a pair of particle
  Update $\mathbf{F}_i$ and $\mathbf{F}_{i+1}$
  $\mathbf{p}_i \leftarrow \mathbf{p}_i + (\Delta t/2)\mathbf{F}_i$
  $\mathbf{p}_{i+1} \leftarrow \mathbf{p}_{i+1} + (\Delta t/2)\mathbf{F}_{i+1}$
  if $\mathscr{U}(0,1) \leq \Gamma \Delta t$ **then**
    if $|\mathbf{r}_i - \mathbf{r}_{i+1}| \leq R_T$ **then**
      $M \leftarrow m_i * m_{i+1}/(m_i + m_{i+1})$ ▷ reduced mass is calculated
      $v_{cm} \leftarrow (\mathbf{p}_i + \mathbf{p}_{i+1})/(m_i + m_{i+1})$
      $\lambda \leftarrow \mathscr{N}(0, \sqrt{k_B T/M})$
      $\mathbf{p}_i \leftarrow m_i * v_{cm} + M * \lambda$
      $\mathbf{p}_{i+1} \leftarrow m_{i+1} * v_{cm} - M * \lambda$
    end if
  end if
end for

two particles in distance r is given by

$$U_{\mathrm{LJ}}(r) = 4\varepsilon \left[\left(\frac{\sigma}{r}\right)^{12} - \left(\frac{\sigma}{r}\right)^{6} \right]. \tag{3.16}$$

This potential is small for large pair separations, so it is put to zero for distances greater than some cutoff radius r_c. This truncation produces a drift in the energy due to the discontinuity at $r = r_c$. To reduce energy drift, the potential is shifted and smoothly truncated so that it remains C^2-continuous at the cutoff, and thus the force and its derivatives are continuous there. The potential takes the form

$$U(r_{ij}) = \begin{cases} \left(U_{\mathrm{LJ}}(r) - U_{\mathrm{LJ}}(r_c)\right) g\left(\dfrac{r - r_c}{h}\right), & r \leq r_c, \\ 0, & r > r_c. \end{cases} \tag{3.17}$$

A smoothing function $g(\zeta) = \frac{\zeta^4}{1+\zeta^4}$ is multiplied on the shifted potential in this equation. h controls the smoothing range and is much smaller than σ and is typically chosen to be 0.005σ. The resulting force $\mathbf{F} = -\nabla U$ is continuous and has the magnitude

$$|\mathbf{F}(\mathbf{r})| = |\mathbf{F}_{\mathrm{LJ}}(\mathbf{r})| g\left(\frac{r - r_c}{h}\right) - \frac{1}{h} U(r) g'\left(\frac{r - r_c}{h}\right) \quad ; \quad r \leq r_c. \tag{3.18}$$

Calculation of the pair potentials of a system of N particles is of order (N^2). By considering a cutoff distance, the calculational expense is reduced to $\mathcal{O}(N{r_c}^3 \log N)$ [57].

On the GPU, each thread reads the indices of a particle's neighbors, then reads the coordinates and calculates the potential and force.

3.5.2 Tabulated external force

To meet the requirements of a method described in the following chapter, we need to apply an external one-body force $F(\mathbf{r})$ in the simulation box. This force, as well as the potential from which it is extracted, are position dependent. For more flexibility, the values of force and potential are tabulated on a regular grid in space referred to as "knots". The values between the knots are then calculated using cubic Hermite spline interpolation. The result of the interpolation, as well as its first derivative, are then continuous. The Hermite interpolation has the advantage of working well with periodic boundary conditions.

For simplicity, we will explain the method in one space dimension. A number of knots are determined and each has two neighbors. Consider the first two points with values x_0 and x_1. The known potential values of these points are $U(x_0)$ and $U(x_1)$ and we aim to find the potential and force values for point x located between them, $x_0 < x < x_1$. The interval is mapped to $[0,1]$ with

$$t = \frac{x - x_0}{x_1 - x_0} \quad , x_1 > x_0. \tag{3.19}$$

The potential in x is approximated by the third order polynomial

$$\begin{aligned} U(x) = {} & h_{00}(t)U(x_0) + h_{10}(t)(x_1 - x_0)\partial_x U(x_0) \\ & + h_{01}(t)U(x_1) + h_{11}(t)(x_1 - x_0)\partial_x U(x_1) \end{aligned} \tag{3.20}$$

In this equation, $h_{ij}(t)$ are the Hermite basis functions

$$\begin{aligned} h_{00}(t) &= 2t^3 - 3t^2 + 1, \quad h_{10}(t) = t^3 - 2t^2 + t, \\ h_{01}(t) &= -2t^3 + 3t^2, \quad h_{11}(t) = t^3 - t^2. \end{aligned} \tag{3.21}$$

In two and three dimensions, each point has four and eight neighboring knots respectively, and the same interpolation is done in the other directions as well.

3.6 Local groups of particles

It will be necessary to treat a group of particles differently than others, for example, to track some specified particles in the system, to calculate an observable for a group of particles only, or to apply a thermostat to the particles of a region in the box rather than to all the particles. These are all available in HALMD package, and I had a contribution in implementing the region groups, which select all or those particles with a special chemical species that are either inside or outside of a region.

Because particles move continuously and may enter or leave the region, the list of IDs of the particles in the region and region-species groups change during the simulation, so the particle selection should be constantly updated. The possible geometries include spheres and cuboids. After updating particle positions, they are checked to see if they are in or out of the region, and the group selection is updated accordingly. This is checked for a spherical geometry by the center coordinate $\mathbf{r}_o$ and radius d. If $|\mathbf{r}-\mathbf{r}_o| < d$, the particle is inside. The criteria for the cuboid region are checked using the position of the region's lowest left corner $\mathbf{r}_{\mathrm{cr}}$ and the edge lengths $\mathbf{d}$. If for each dimension i, $0 < (\mathbf{r}[i]-\mathbf{r}_{\mathrm{cr}}[i]) < \mathbf{d}[i]$, the particle is inside the cuboid region. The chemical species can also be checked before finalising the selection.

3.7 Monte-Carlo simulation in grand canonical ensemble

For future reference, the grand canonical Monte Carlo method is described below. To derive the proper equations, we start with a canonical system of particles and develop the grand canonical partition function and probability densities from there [58].

Grand canonical ensemble from canonical ensemble

In a cubic box of volume $V = L^3$, at temperature T and with N particles, the partition function is given by

$$Q(N,V,T) = \frac{1}{\Lambda^{3N} N!} \int_0^L \cdots \int_0^L d\mathbf{r}^N \exp\left(-\beta U(\mathbf{r}^N)\right), \tag{3.22}$$

where $\Lambda = \sqrt{h^2/(2\pi k_B T)}$ is the thermal de Broglie wavelength and h is Planck's constant. Then the position can be rewritten as $\mathbf{r}_i = L\mathbf{s}_i$ for $i = 1,2,...,N$. This changes equation 3.22 to

$$Q(N,V,T) = \frac{V^N}{\Lambda^{3N} N!} \int_{[0,1]^{3N}} d\mathbf{s}^N \exp\left(-\beta U(\mathbf{s}^N; L)\right), \tag{3.23}$$

Now, going toward the grand canonical ensemble, we assume this box is embedded in a reservoir of ideal gas with volume V'. Assume the universe has a volume V_0 and contains M particles, N of which are inside the smaller box and $M-N$ particles outside and in the reservoir.

This means there is volume V accessible to N interacting particles and a volume $V' = V_0 \setminus V$ accessible to $M-N$ non-interacting particles. For each of these systems, a partition function as in eq. (3.23) can be assigned. The partition function of the combined system is the product of these two independent subsystems:

$$Q(N,M,V,V_0,T) = \frac{V^N (V')^{M-N}}{\Lambda^{3M} N!(M-N)!} \int d\mathbf{s}'^{M-N} \int d\mathbf{s}^N \exp\left(-\beta U(\mathbf{s}^N; L)\right). \tag{3.24}$$

The particles in the reservoir are non-interacting and there is no dependence on $\mathbf{s}'$. If the subsystems are allowed to exchange particles, N can change from 0 to M and thus the partition function of the system, including all possible distributions of the M particles over the two subvolumes, is

$$Q(M,V,V_0,T) = \sum_{N=0}^{M} \frac{V^N (V')^{M-N}}{\Lambda^{3M} N!(M-N)!} \int d\mathbf{s}^N \exp\left(-\beta U(\mathbf{s}^N; L)\right). \tag{3.25}$$

The probability distribution of the M particles with N particles in the subvolume V is given by

$$p(\mathbf{s}^M; N) = \frac{V^N (V')^{M-N}}{Q(M,V,V',T)\Lambda^{3M} N!(M-N)!} \exp\left(-\beta U(\mathbf{s}^N)\right). \tag{3.26}$$

In the limit of a large reservoir, $V' \to \infty$ and $M \to \infty$, such that the density is $\rho = M/V' = \text{const.}$. On the other hand, the chemical potential μ^{id} of the ideal gas depends on density as $\mu^{\text{id}} = k_B T \ln \Lambda^3 \rho$. These will change the probability density to

$$p(\mathbf{s}^N; N) \sim \frac{V^N \exp(\beta \mu^{\text{id}} N)}{\Lambda^{3N} N!} \exp\left(-\beta U(\mathbf{s}^N)\right). \tag{3.27}$$

The process in the Metropolis algorithm is done by the random choice of adding or removing a particle with equal weight. Then a particle is selected randomly from all N particles and the acceptance probabilities of the change are checked for the final decision.

Add or remove 1 particle

The acceptance probability of adding one particle to the subvolume V is calculated as follows:

$$\mathrm{acc}(N \to N+1) = \frac{p(\mathbf{s}^{(N+1)}; N+1)}{p(\mathbf{s}^N; N)} = \frac{V \exp(\beta\mu^{\mathrm{id}})}{\Lambda^3} \exp(-\beta[U(\mathbf{s}^{(N+1)}) - U(\mathbf{s}^{(N)})). \tag{3.28}$$

defining reduced fugacity , $\zeta = \frac{V \exp(\beta\mu^{\mathrm{id}})}{\Lambda^3}$. Specialising to the ideal gas (our final purpose is to apply MC on the TR regions), the potential terms vanish and the equation is simplified. The acceptance probability of removing one particle is calculated in a similar way, and it holds

$$\mathrm{acc}(N \to N+1) = \min(1, \frac{\zeta}{N+1}), \qquad \mathrm{acc}(N \to N-1) = \min(1, \frac{N}{\zeta}). \tag{3.29}$$

The Monte-Carlo Markov chain should be symmetric which means the probability to move a particle from V' to V is equal to the probability of the reverse move. This detailed balance condition reads:

$$P(N+1)\,\mathrm{acc}(N+1 \to N) = P(N)\,\mathrm{acc}(N \to N+1), \tag{3.30}$$

where $P(N)$ is the probability that the system has N particles. Substituting eq. (3.29) into eq. (3.30) yields

$$P(N+1) = P(N)\frac{\min(1, \frac{\zeta}{N+1})}{\min(1, \frac{N+1}{\zeta})} = P(N)\frac{\zeta}{N+1}. \tag{3.31}$$

Considering $P(0) = P_0$, we get $P(N) = \frac{\zeta^N}{N!}P_0$. We also have $\sum_{N\geq 0} P(N) = 1$ and this determines $P_0 = \exp(-\zeta)$. With this, the equilibrium distribution is found as

$$P(N) = \frac{\zeta^N}{N!}\exp(-\zeta), \tag{3.32}$$

which is a Poisson distribution and thus $\langle N \rangle = \zeta$ (fig. 3.6).

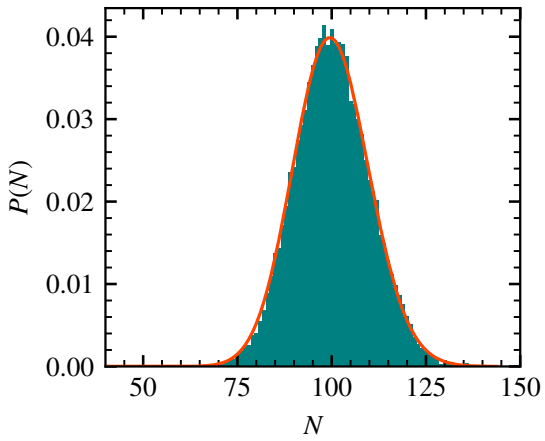

Figure 3.6: Probability distribution of particle numbers in a system of non interacting particles. The process is done for 10^6 MC steps and one particle is exchanged in each MC step randomly, so that the mean number of particles or equivalently ζ reaches 100. This results in $\overline{N} = 100.210$ with standard deviation $\Delta N = \sqrt{\mathrm{Var}[N]} = 9.913$, which accurately reproduces the expectations, $\overline{N} = \zeta$ and $\Delta N = \sqrt{\zeta}$. The solid line is the corresponding Poisson distribution.

Add or remove k particles

The probabilities of acceptance are calculated as in the previous section and are as follows:

$$\begin{aligned} \mathrm{acc}(N \to N+k) &= \min\left(1, \frac{\zeta^k}{\Pi_{j=1}^{k}(N+j)}\right), \\ \mathrm{acc}(N \to N-k) &= \min\left(1, \frac{\Pi_{j=0}^{k-1}(N-j)}{\zeta^k}\right) \end{aligned} \tag{3.33}$$

The important point here is that in order to get a Poisson like distribution, k must not be fixed and in each MC step and a random number of particle between 1 and k should be moved. We tested this for $\zeta = 1000$ and $1 < k < 100$. The result is $\overline{N} = 999.957$ with standard deviation $\Delta N = 31.57$.

Exchange of k particles between two subsystems

Eventually, we consider two subsystems and exchange k particles between them instead of adding or removing particles with the reservoir. The second subsystem has N' particles, with reduced fugacity ζ'. The acceptance probabilities are determined by multiplication of the two

trial probabilities.

$$\begin{aligned}
\mathrm{acc}(N \to N+k, N' \to N'-k) &= \min\left(1, \frac{\zeta_N^k \Pi_{j=0}^{k-1}(N'-j)}{\zeta_{N'}^k \Pi_{j=1}^{k}(N+j)}\right), \\
\mathrm{acc}(N \to N-k, N' \to N'+k) &= \min\left(1, \frac{\zeta_{N'}^k \Pi_{j=0}^{k-1}(N-j)}{\zeta_N^k \Pi_{j=1}^{k}(N'+j)}\right),
\end{aligned} \tag{3.34}$$

This was tested for $\zeta = 100, \zeta' = 50$. Up to 10 particles are exchanged randomly in each step and the results are shown in fig. 3.7.

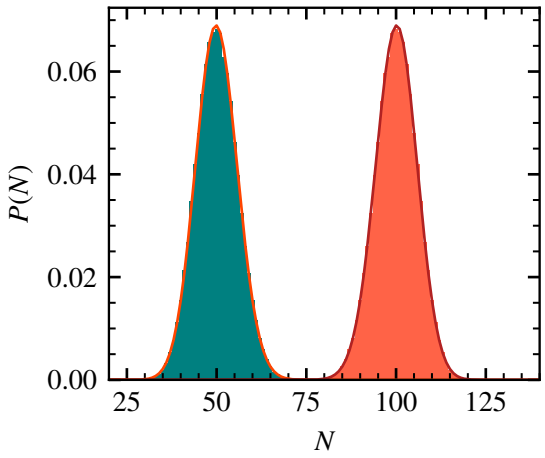

Figure 3.7: Probability distribution of particle numbers. A random number of particles between 1 and 10 are exchanged in each MC step randomly between two subsystems to set the number of particles to be 100 in one box and 50 in another. $\overline{N} = 100.0155$ and $\overline{N'} = 49.985$ with standard deviation to be 5.770. The solid lines are Poisson distributions for 50 and 100.

Exchange of k_1 and k_2 particles

If two independent exchanges occur in the system, the acceptance probabilities are modified to read

$$\begin{aligned}
&\mathrm{acc}(N \to N + k_2 - k_1, N' \to N' - k_2 + k_1) \\
&= \min\left(1, \frac{\Pi_{j=0}^{k_2-1}(N' - j)}{\zeta'^{k_2}} \frac{\Pi_{j=0}^{k_1-1}(N + k_2 - j)}{\zeta^{k_1}} \frac{\zeta^{k_2}}{\Pi_{j=1}^{k_2}(N + j)} \frac{\zeta'^{k_1}}{\Pi_{j=1}^{k_2}(N' - k_2 + j)}\right), \\
&\mathrm{acc}(N \to N + k_1 - k_2, N' \to N' - k_1 + k_2) \\
&= \min\left(1, \frac{\Pi_{j=0}^{k_2-1}(N - j)}{\zeta^{k_2}} \frac{\Pi_{j=0}^{k_1-1}(N + k_2 - j)}{\zeta'^{k_1}} \frac{\zeta'^{k_2}}{\Pi_{j=1}^{k_2}(N' + j)} \frac{\zeta^{k_1}}{\Pi_{j=1}^{k_1}(N - k_2 + j)}\right),
\end{aligned} \tag{3.35}$$

which is supported by numerical tests.

4 Open Systems Out of Equilibrium

In the first part of this chapter, we consider the BL theoretical model for open systems out of equilibrium and translate its principles to the AdResS technique. The model claims the linear summation of the action of different reservoirs and this was tested with Lennard-Jones fluids imposed to thermal gradients. In the second part, more details on the theoretical model are presented, the range of validity of this linear summation approximation is tested and a formulation of an extension of this model in order to account for nonlinear effects is discussed.

Section 4.1 is published as "Communication: Theory and simulation of open systems out of equilibrium" in the Journal of Chemical Physics (2020) [22], and was selected by editor as a Featured article.

Section 4.2 is published as "Nonequilibrium induced by reservoirs: Physico-mathematical model and numerical tests" in Advanced Theory and Simulation (2021) [23].

The content has been brought here unchanged and contains some information that has already been explained.

4.1 Open systems exposed to thermal gradients

We consider the theoretical model of Bergmann and Lebowitz for open systems out of equilibrium and translate its principles in the adaptive resolution molecular dynamics technique (AdResS). We simulate Lennard-Jones fluids with open boundaries in a thermal gradient and find excellent agreement of the stationary responses with results obtained from the simulation of a larger, locally forced closed system. The encouraging results pave the way for a computa-

tional treatment of open systems far from equilibrium framed in a well-established theoretical model that avoids possible numerical artifacts and physical misinterpretations.

Many applications of modern nanotechnology rely on processes that are far from equilibrium and their efficient control requires insight into their principles. Long-standing and relevant problems with recent progresses in experiment and simulation include fluid flow through nanopores [2, 59–61], gas storage in microporous hosts [62, 63], and the diffusion and permeability in random media [64–67]. Thermal gradients, in particular, are of ongoing interest in molecular nanoscience as they give rise to a variety of nonequilibrium phenomena such as the evaporation of liquids [3, 68], the thermomolecular orientation of nonpolar fluids [69], effects of thermo-phoresis [70, 71] and osmosis [5], separation in liquid mixtures [72, 73], diffusion of polymers in a solvent [74, 75], heat transfer in protein–water interfaces [76], and the polarization of water [77] to cite but a few.

Molecular simulation can provide techniques that may both support our understanding of the detailed mechanisms responsible for the observed phenomena and guide the design and optimization of future applications. However, Molecular simulation, and its most popular variant molecular dynamics (MD) in particular, faces two interconnected problems when dealing with systems out of equilibrium. MD techniques were developed originally for equilibrium situations, whereas out-of-equilibrium simulations not only have a more complex mathematical description but also call for related, more complex computational protocols. Nonequilibrium MD (NEMD) techniques have been desired and developed by the MD community since 50 years and various conceptual approaches and efficient techniques are available today [6]. Most of these techniques rely on the simulation of systems with a fixed and typically large number of particles, thereby simultaneously representing the—generally limited—region of physical interest and the surrounding environment.

In the present work, we describe instead a nonequilibrium extension of the adaptive resolution simulation (AdResS) approach, which was developed in the past decade [25, 26, 78] for systems in equilibrium. The goal of the approach is the reduction of the computational complexity of a molecular simulation by focusing the main efforts, with full details and high accuracy, only on those regions in which the physics of interest is taking place. The surrounding environment is, in contrast, simplified to the essential degrees of freedom that are required to avoid undue losses of physical information relevant to the region of interest. The region of high resolution is effectively reduced to an open sub-domain of the total system that exchanges energy and particles with its environment, the latter playing the role of a thermodynamic reservoir at prescribed macroscopic conditions [79].

The new conceptual challenge in developing a nonequilibrium extension to this approach

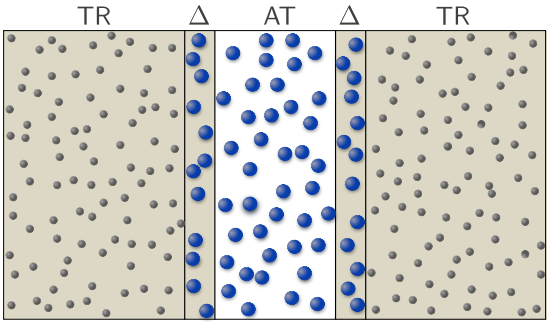

Figure 4.1: Schematic illustration of the typical AdResS set-up. The atomistically resolved region AT is the region of interest, in which particles evolve under Hamiltonian dynamics without artificial forcing. The AT region is interfaced with the Δ regions where molecules have atomistic resolution and are, in addition, subject to a thermostat and to the one-particle "thermodynamic force", which assures the proper equilibrium in the AT region. Each Δ region is interfaced on the other side with a reservoir of tracers, i.e., with non-interacting particles whose thermal state is controlled by the same thermostat and thermodynamic force that act in the Δ region. Extreme repulsions between tracer particles whose centers are unphysically close upon entering the Δ region are controlled by capping the forces on these particles at a certain threshold.

is the proper representation of the statistical mechanics of an open system that is out of equilibrium with its given surroundings. The aim is to show that the model of Bergmann and Lebowitz (BL) for open systems far from equilibrium [33, 34] provides a theoretical framework that justifies the use of the AdResS approach as a simulation protocol for nonequilibrium situations, here specifically applied to a liquid with open boundaries [15] in a thermal gradient.

4.1.1 Adaptive resolution technique

AdResS in its latest version [17, 35] consists of a simulation set-up in which space is divided in two parts, a region of interest where molecules have an atomistic resolution (AT), and a larger region (TR), serving as a reservoir, where molecules are represented by non-interacting point particles (tracers) thermalized at a prescribed temperature by an imposed thermostat. At the interface between these two regions lies a region (Δ) where molecules have atomistic resolution and are subject to the action of a thermostat and a one-particle force, $\vec{F}_{\text{th}}(\vec{r})$, named thermodynamic force (see also the pictorial representation in fig. 4.1). In an equilibrium set-up, the latter enforces the expected thermodynamic, structural, and dynamic equilibrium properties within the atomistic subdomain, without noticeable artifacts. The derivation of the method is based on the equality in equilibrium of the grand potential of the atomistic region and the rest of the system [24]. $\vec{F}_{\text{th}}(\vec{r})$, in essence, induces a local balancing of the pressure, $p(\vec{r})$, to the fully atomistic value of reference. Related studies [79, 80] have shown that the work due to $\vec{F}_{\text{th}}(\vec{r})$ balances, together with the work of the thermostat, the difference in chemical potential between the atomistic region and the rest of the system. For practical applications

$\vec{F}_{\rm th}(\vec{r})$ is calculated via an iterative procedure with the aim of eliminating in Δ local variations of the density with respect to the value at the desired thermodynamic state point as it would be obtained from a full atomistic simulation [24, 38, 78]. The converged function, $\vec{F}_{\rm th}(\vec{r})$, is then employed in subsequent production runs without further amendments.

At the technical level, in the set-up of fig. 4.1, molecules of the AT region interact through atomistic force fields among themselves and with molecules in Δ, whereas there is no direct interaction with the tracers. The two contributions yield the potential energies $U_{\rm AT-AT}$ and $U_{\rm AT-\Delta}$, respectively. Second, the thermodynamic force derives from a potential, $\vec{F}_{\rm th}(\vec{r}) = -\nabla\varphi_{\rm th}(\vec{r})$, with the convention that $\varphi_{\rm th} = 0$ in the AT region [17]. The total potential energy of the system is thus $U_{\rm tot} = U_{\rm AT-AT} + U_{\rm AT-\Delta} + \sum_{j\in\Delta\cup{\rm TR}}\varphi_{\rm th}(\vec{r}_j)$, where $\vec{r}_j$ denotes the position of particle j. A relevant conceptual step in the elaboration of the method reported above is the mapping of the AdResS protocol onto a well established theoretical framework for the statistical mechanics of an open system [32, 38, 78, 81]. In fact, all the principles of the AdResS protocol have been put in direct relation with the principles of the stochastic model of open systems developed by Bergmann and Lebowitz [33, 34].

4.1.2 Bergmann-Lebowitz model of open system

In the BL model the open system is embedded in an environment of one or more reservoirs ($r = 1,\ldots,m$) with which the system exchanges energy and particles. The coupling between the system and reservoir r consists of an impulsive interaction at discrete points in time, which is mathematically formalized by a suitable kernel $K^r_{nn'}(X'_{n'}, X_n)$. This represents the probability per unit time that, due to the interaction, the n-particle open system with phase space configuration X_n makes a transition to n' particles with phase space configuration $X'_{n'}$. In the evolution equation for the n-particle phase-space probability $f_n(X_n,t)$,

$$\frac{\partial f_n(X_n,t)}{\partial t} = \{f_n(X_n,t), H_n(X_n)\} + I_n(X_n, f(t))\,, \tag{4.1}$$

the last term

$$I_n(X_n,f(t)) := \sum_{r=1}^{m}\sum_{n'=0}^{\infty}\int dX'_{n'}\left[K^r_{nn'}(X_n,X'_{n'})f_{n'}(X'_{n'},t) - K^r_{n'n}(X'_{n'},X_n)f_n(X_n,t)\right], \tag{4.2}$$

depends on the full hierarchy $f(t) = \{f_{n'}(\cdot,t)\}_{n'=0,1,\ldots}$ at time t and expresses the interaction between the system and the m reservoirs. Equation (4.1) is the equivalent of Liouville's equation for an open system in contact with several reservoirs. The development of a systematic

procedure for deriving an analytic form of $K^r_{nn'}(X_n, X'_{n'})$ for complex many-particle systems represents, until now, a formidable task. For this reason, in molecular simulations one can only design algorithms which mimic, as close as possible, the expected action of the kernel, $K^r_{nn'}(X_n, X'_{n'})$, without knowing its exact analytic expression. Along these lines we now proceed with a discussion of the analogy between the AdResS protocol and the BL model.

4.1.3 Analogy of AdResS and the BL model

The AT region in the AdResS scheme can be interpreted as an open system in the sense of the BL model under the approximation that the reservoir (TR and Δ region) is large enough and that $U_{\mathrm{AT-AT}} \gg U_{\mathrm{AT-}\Delta}$, i.e., that the interaction energy between the particles in the atomistic region and the particles in Δ is negligible. Furthermore, the action of the transition kernel in the BL model, in AdResS corresponds to (i) the force which particles in Δ impose on particles in AT and (ii) to the exchange of particles between AT and Δ. The former impose changes of momentum and energy of the particles residing in AT, the latter allows for changes of the number of particles inside the AT region. The combined action of the thermodynamic force and the thermostat in Δ guarantees that the statistics of the Δ-particles is maintained at the desired reservoir state [32, 38, 78, 81].

In its general form, the BL model allows for the instantaneous exchange of an arbitrary number of particles through the action of the stochastic exchange kernels. At the same time the system state can undergo arbitrary changes in phase space as well. In contrast, in the situation we consider in AdResS, i.e., that of a dynamically evolving open system, instantaneous changes of the particle number larger than one and state changes that involve particles far away from the system boundaries are extremely unlikely. Therefore, a specification of the BL kernel to this situation would call for setting $K_{nn'} = 0$ whenever $|n - n'| > 1$. Similarly, for substantial transition probabilities $K_{nn'}(X_n, X_{n'})$, X_n and $X_{n'}$ should be nearly identical for all particles far away from the boundaries [82, 83]. Conceptually, the AdResS approach implements these constraints in that (i) number changes are induced by a dynamical process continuous in time for which simultaneous crossing of the boundaries by more than one particle is extremely unlikely and (ii) particles entering or leaving the open system would at this instant influence only their immediate surroundings but not the entire system domain. In this sense, one way to interpret the AdResS set-up is as a dynamic-like approximation of the BL stochastic process or vice versa. Numerical simulations showed that indeed under such a framework AdResS follows the grand canonical behaviour predicted within the BL model for equilibrium (see e.g. Refs. [17, 18, 32]).

4.1.4 Nonequilibrium of an open system

Bergmann and Lebowitz [34] pointed out that, according to their model, a system connected to two (or more) reservoirs with different thermodynamic conditions, e.g., different temperatures, in the stationary state will have heat (and mass) currents flowing through the system. Formally, such currents are produced by the interaction terms I_n ($n = 0, 1, \ldots$) of the extended Liouville equation 4.1, with I_n defined in eq. (4.2). For the AdResS simulation the equivalent effect, according to the analogy with the BL model, is produced by coupling the region AT of interest to two reservoirs that are at different thermodynamic state points of the fluid, specified for example by their temperature and density, (T_1, ρ_1) and (T_2, ρ_2), respectively (fig. 4.2). For simplicity, we restrict to set-ups with planar interfaces; then the thermodynamic force $\vec{F}_{\text{th}}(\vec{r})$ depends only on the position x along the interface normal and consists only of the vector component F_{th} along the x direction. In a prepratory step, one needs to pre-compute $F_{\text{th}}^{(1)}(x)$ at the state point (T_1, ρ_1) and, separately, $F_{\text{th}}^{(2)}(x)$ at the other state point (T_2, ρ_2); the result may be stored in a "dictionary" mapping pairs (T_i, ρ_i) to $F_{\text{th}}^{(i)}(x)$ for later reference. The nonequilibrium AdResS set-up is then realized by employing $F_{\text{th}}^{(1)}(x)$ together with a thermostat at the temperature T_1 in the Δ_1 and TR_1 regions and correspondingly for the second reservoir using $F_{\text{th}}^{(2)}(x)$ and a thermostat at T_2.

To demonstrate that this protocol will indeed approximate the behavior of a large molecular system with spatially separated thermodynamic forcings, we performed numerical experiments on Lennard-Jones (LJ) fluids that are subject to a temperature gradient (see below). If a set of relevant physical observables, computed from the AT region of the set-up only, agrees with the results of a full atomistic simulation, it is corroborated that the BL model with localized exchange kernels provides a solid theoretical reference for AdResS simulations far from equilibrium and we can conclude that the combination of the BL model with the AdResS protocol provides a promising basis for further development in the theory and simulation of open systems, in and out of equilibrium [82, 83].

4.1.5 Nonequilibrium simulations

Motivated by a recent study [84], we simulated the stationary response of a LJ fluid to an applied temperature gradient using the nonequilibrium AdResS set-up described above (fig. 4.2). The stationary state of the analogous full atomistic simulation is characterized by mechanical equilibrium, in which pressure gradients are balanced. We have accounted for this fact by choosing the reservoir states 1 and 2 along an isobar of the fluid: for given temperatures T_1 and T_2, we determined the densities ρ_1 and ρ_2 that yield equal pressures, $p(T_1, \rho_1) = p(T_2, \rho_2)$, according to the equation of state. For the initial equilibrium state, we

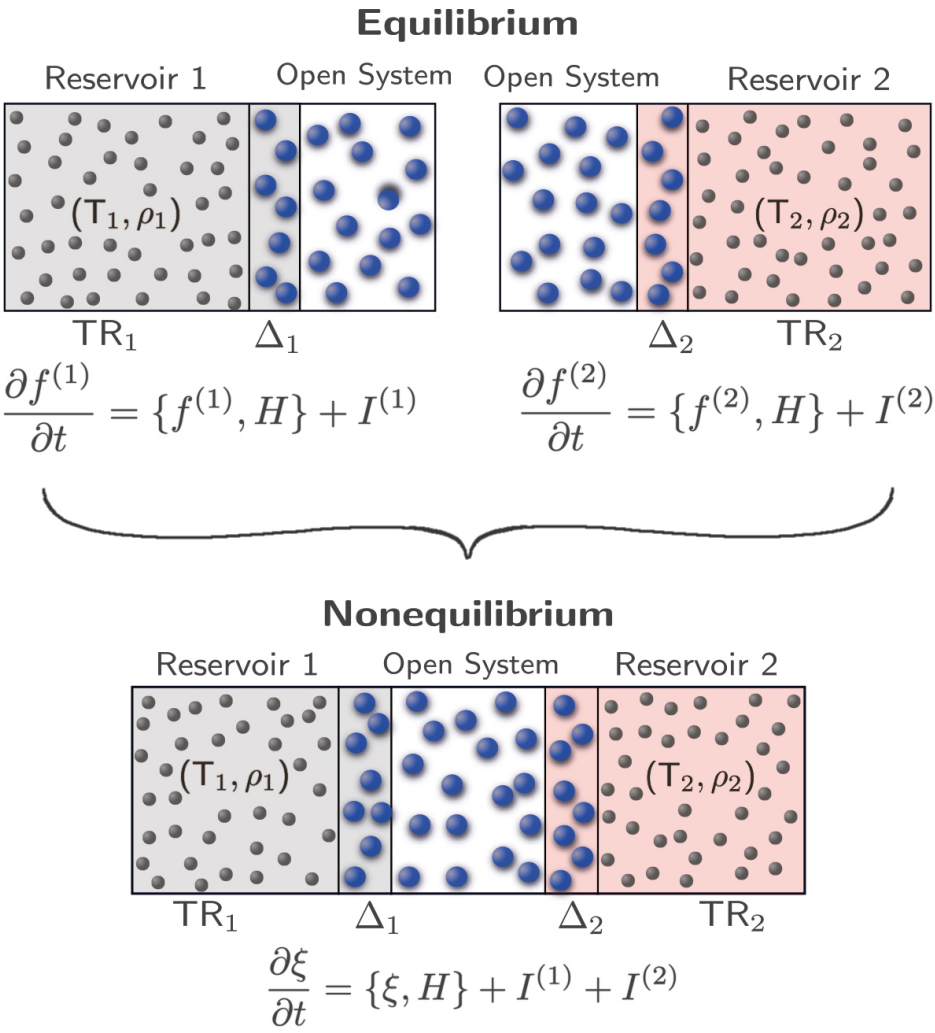

Figure 4.2: Schematic illustration of the meaning of a thermal gradient in the BL model and its corresponding mapping into the AdResS set-up. When interacting only with one reservoir the system equilibrates at the thermodynamic condition of the reservoir. In the BL model [eqs. (4.1) and (4.2)], this is equivalent to defining the transition term $I^{(i)}$ for system $i = 1$ or 2, while in AdResS it means that the Δ_i and TR_i regions are subject to a thermostat with target temperature T_i and the corresponding thermodynamic force, $F^{(i)}_{\text{th}}(x)$. Once the system is in contact with two different reservoirs, then in the BL model one has the combined effect of $I^{(1)} + I^{(2)}$, which, in the AdResS set-up, translates into a region $\Delta_1 \cup TR_1$ forced at temperature T_1 and by $F^{(1)}_{\text{th}}(x)$ and a region $\Delta_2 \cup TR_2$ with parameters T_2 and $F^{(2)}_{\text{th}}(x)$.

used a state point in the liquid phase with number density $\overline{\varrho} = (\varrho_1 + \varrho_2)/2 = 0.65\,\sigma^{-3}$ and temperature $\overline{T} = (T_1 + T_2)/2 \approx 0.91\,\varepsilon/k_\mathrm{B}$; the symbols σ and ε serve as units of length and energy and refer to the parameters of the LJ potential, which was truncated at $r_c = 2.5\,\sigma$ (see also Supplementary Material). A temperature difference of $\Delta T = T_2 - T_1 = 0.125\,\varepsilon/k_\mathrm{B}$ was then imposed symmetrically. To this end, the AdResS set-up was first equilibrated at $(\overline{T}, \overline{\varrho})$ using the same, suitably adjusted reservoir parameters on both sides, which yields a uniform density and temperature across the whole set-up comprised of AT, Δ, and TR regions. Then, the states of the two reservoirs were switched to (T_1, ϱ_1) and (T_2, ϱ_2) by (i) replacing the thermodynamic force of the equilibrium set-up by the forces $F_\mathrm{th}^{(1)}(x)$ and $F_\mathrm{th}^{(2)}(x)$, respectively (see above), and by (ii) changing the thermostat temperatures to T_1 and T_2. The system evolves under this non-equilibrium forcing to a stationary state of inhomogeneous density and temperature; concomitantly, the pressure adjusts from its initial value to the common value of the reservoirs.

Both the nonequilibrium AdResS set-up and the full atomistic simulation, serving as a benchmark for reference, were implemented in the simulation framework "HAL's MD package" [20, 21], which features large systems due to massive parallelization provided by high-end graphics processors and, concomitantly, excellent numerical long-time stability of Hamiltonian dynamics; the technical details can be found in the Supplementary Material. We have verified that the AT regions of the equilibrium set-ups of AdResS for the calculation of $F_\mathrm{th}^{(1)}(x)$ and $F_\mathrm{th}^{(2)}(x)$, satisfy the conditions of an open system (see Supplementary Section II.B). The resulting thermodynamic forces can be found along with their potentials in Supplementary Fig. S2. Nonequilibrium averages were computed as in Ref. [84] using the D-NEMD approach developed by [85]. It consists of running MD simulations for an equilibrium (or, at least, stationary) state of reference, e.g., a fluid at temperature $\overline{T}$. Along the obtained system trajectory a series of uncorrelated samples is selected, from which an ensemble of nonequilibrium trajectories is branched off by taking these samples as initial configurations of the NEMD simulations with, e.g., an imprinted thermal gradient.

Following [84], we have considered the observables density, temperature, and heat flux and calculated their spatial profiles $\varrho(x)$, $T(x)$, and $J(x)$, respectively, which emerge as the stationary response to the nonequilibrium forcing by the reservoirs. The absence of many-body interactions permits the calculation of the heat flux in a slab-like control volume Ω centered at position x^* as [84, 86] $J(x^*) = V_\Omega^{-1} \sum_{j\in\Omega} (e_j + tr\vec{\sigma}_j)\vec{v}_j$; therein, e_j, $\vec{\sigma}_j$, and $\vec{v}_j$ denote the total energy, the potential part of the stress tensor, and the velocity of the j-th particle, respectively, and V_Ω is the volume of Ω. Within the AT region, where the molecular dynamics evolves freely without a thermostat nor a thermodynamic force, all three profiles obtained from the AdResS set-up show excellent agreement with the results of the corresponding full atomistic simulation (fig. 4.3). In particular, the density profile interpolates non-linearly between the

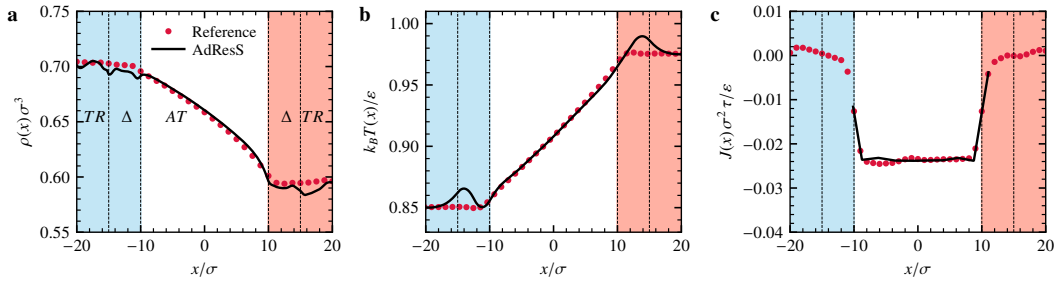

Figure 4.3: Results of open-system simulations for a Lennard-Jones (LJ) liquid in a thermal gradient obtained from the nonequilibrium AdReS set-up (solid lines, fig. 4.2) and from a full atomistic simulation serving as reference (dots). Both set-ups share the same geometry of the simulation box, in particular, the same size of the region of interest (AT) and the same box length $120\,\sigma$ along the x-axis; parts of the tracer regions (TR) have been omitted for clarity. The units of energy, length, and time are given by the LJ parameters ε, σ, and τ, respectively. The panels display spatial profiles of (a) the particle number density $\varrho(x)$, (b) the temperature $T(x)$, and (c) the heat flux $J(x)$, as stationary responses to the nonequilibrium forcing.

reservoir densities, a feature that is already present in the full atomistic simulations and that is well reproduced by the AdResS set-up. In the Δ region, the system is artificially forced so that an agreement with the reference is neither required nor expected; most importantly, the small peaks of the temperature profile $T(x)$ near the Δ/TR boundary decay within the Δ region. These peaks originate from the instantaneous change of resolution at these boundaries, which introduces heat into the system that needs to be removed by the thermostat. The peak height depends on details of the thermostat and can be adjusted, see supplementary material and fig. 4.6.

As a second test, we performed simulations along the same lines for a supercritical LJ fluid at moderate density $\overline{\varrho} = 0.3\,\sigma^{-3}$ and elevated temperature $\overline{T} = 1.5\,k_B/\varepsilon$, well above the liquid–vapour critical point, with a symmetric temperature difference of $\Delta T = 0.2\,k_B/\varepsilon$. This fluid is more compressible and exhibits a six-fold higher pressure than the above liquid. The obtained profiles are reported in Supplementary fig. 4.8 and show the same high degree of agreement as found for the liquid case.

4.1.6 Conclusions

We have introduced a generic MD framework that is designed to simulate open systems out of equilibrium and have demonstrated its use for an open-boundary LJ fluid in a thermal gradient. We have shown that an AdResS set-up that follows a tight analogy to the BL stochastic model of open systems out of equilibrium can accurately reproduce the full atomistic simulations with large reservoirs serving as benchmark reference. Such results allow one to employ AdResS and the BL model with localized exchange kernels as a prototype theoretical and numerical model

of reference in the development and application of open system approaches in molecular simulation. In particular, the proposed method enables the explicit control over the reservoir states and delivers great flexibility with respect to the simulated scenarios. The price to pay is the need to determine the thermodynamic force for the reservoir states in a preparatory step, which, however, can be automated and tabulated. As a computational advantage, it allows cutting the load on the simulation of the reservoirs, which can amount to 90% of the system size [15, 18]. An appealing perspective offered by the method concerns its possible use in particle-continuum approaches and the possibility of performing simulations involving mass flow which so far have required problem-specific, tailored solutions not transferable to other situations (see Refs. [83, 87, 88] and references therein).

4.1.7 Supplementary material

4.1.7.1 Simulation details

Physical parameters The simulated Lennard-Jones (LJ) fluids consist of point particles of mass m interacting via the smoothly truncated and shifted pair potential $U(r) = [U_{\mathrm{LJ}}(r) - U_{\mathrm{LJ}}(r_c)]f((r-r_c)/h)$ for $r \leqslant r_c$, and $U(r) = 0$ otherwise, with $U_{\mathrm{LJ}} = 4\varepsilon\left[(r/\sigma)^{-12} - r/\sigma)^{-6}\right]$, the cutoff radius $r_c = 2.5\sigma$, the truncation function $f(x) = x^4/(1+x^4)$, and $h = 0.005\sigma$ [20, 21, 89, 90]. The parameters ε and σ serve as units for energy and length, $\tau = \sqrt{m\sigma^2/\varepsilon}$ defines the unit of time, and dimensionless quantities are given by $\varrho^* = \varrho\sigma^3$ and $T^* = k_{\mathrm{B}}T/\varepsilon$. The tracer particles in the AdResS set-up do not interact with each other and not with the LJ particles in the AT and Δ regions, which is achieved by setting $\varepsilon = 0$ for the interactions involving tracers.

The simulation results reported in Fig. 3 of the main text were obtained for two liquid states along the same isobar. The first point was chosen at temperature $T_2^* = 0.975$ and density $\varrho_2^* = 0.5987$, right at the liquid–vapour coexistence line [91], yielding a (reduced) pressure of $p^* := p\sigma^3/\varepsilon = 0.052$. For the second point, we used the lower temperature $T_1^* = 0.850$ and, from a small sequence of simulations, determined the density $\varrho_1^* = 0.7047$ at which the two liquids have the same pressure, $p(T_1, \varrho_1) = p(T_2, \varrho_2)$. An accurate equation of state and the phase diagram for the truncated LJ potential can be found in Ref. [92].

A second set of simulations was carried out for LJ fluids in the supercritical regime, at moderate density and well above the liquid–vapour critical temperature ($T_c^* \approx 1.08$). Specifically, we have chosen the two state points $(T_1^*, \varrho_1^*) = (1.40, 0.350)$ and $(T_1^*, \varrho_1^*) = (1.60, 0.248)$, corresponding to a pressure of $p^* = 0.32$.

Implementation and algorithmic parameters For AdResS set-ups in its most recent form as employed here [17], the following capabilities are needed beyond standard MD techniques:

(i) partitioning of the the simulation domain into the regions AT, Δ, and TR and unions thereof,

(ii) a stochastic thermostat acting on such subdomains,

(iii) a mechanism for the change of resolution that flips molecules (here: LJ beads) into tracers and back,

(iv) the thermodynamic force calculated from an external, one-particle potential parametrized on a grid,

(v) the capping of excessively large forces between molecules in the Δ region.

We have implemented these requirements into the simulation framework "HAL's MD package" [20, 21], which has proven as an efficient and accurate tool for large-scale MD studies of the dynamics in liquids [90, 93]. Data sets for particle trajectories and time series of thermodynamic observables were stored in the binary and compressed hierarchical file format H5MD [94].

In all nonequilibrium simulations performed, we used a cuboid simulation box of size $120\sigma \times 20\sigma \times 20\sigma$, where the first dimension refers to the direction along which molecules change their resolution, denoted as x-axis. Periodic boundary conditions were applied on all faces of the box, and to this end, the set-up was extended by its mirror image (fig. 4.4). The final set-up contained two independent AT regions (the regions of interest), which separately entered the ensemble average for the calculation of the observed profiles. For the AdResS set-up, each AT region of width 20σ was sandwiched along the x-axis by two transition regions Δ of width 5σ, the remaining space was divided in two equally sized tracer regions (TR) of width 30σ each.

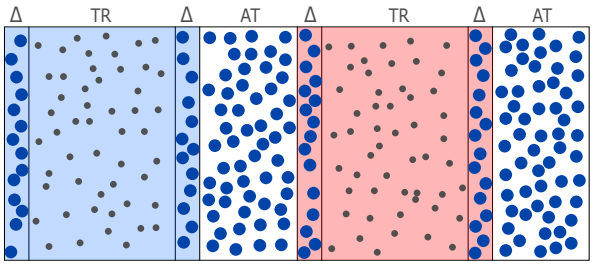

Figure 4.4: Extending the nonequilibrium AdResS set-up (Fig. 2 of the main text) by its mirror set-up facilitates periodic boundary conditions on all faces of the simulation box. The two mirror-symmetric AT regions yield independent samples of the observables.

The total number of particles in the system (LJ beads and tracers) was such that it matches the average density $\overline{\varrho} = (\varrho_1 + \varrho_2)/2$ of the corresponding nonequilibrium states, e.g., 31,282 particles for the liquid case, and the same number of particles was used in the corresponding full atomistic simulation. Non-equilibrium trajectories over a duration of $15{,}000\tau$ were generated with the velocity Verlet integrator with timestep 0.002τ. The first quarter of each trajectory ($3{,}750\tau$) was discarded for the data accumulation of the stationary profiles.

Particles in the AT region are subject to the unmodified Hamiltonian dynamics due to the atomistic force fields. The Δ and TR regions were thermalized with the Andersen thermostat [47], with the update rate set to $\nu_{\text{coupl}} = 50\tau^{-1}$, i.e., a particle's velocity is re-sampled from the Maxwell–Boltzmann distribution every 10 integration steps on average. The choice of the rate influences the peaks of the temperature profiles in the Δ region (Fig. 3b of the main text), which are diminished by a tighter coupling of the thermostat to the system (fig. 4.6).

The thermodynamic force $F_{\text{th}}(x)$ was parametrized on a uniform grid along the x-axis with a knot spacing of 0.25σ using an interpolation in terms of a cubic Hermite spline for the potential $\varphi_{\text{th}}(x)$. The total force on a particle was capped at a threshold of $500\,\varepsilon/\sigma$ for each Cartesian vector component while preserving the sign of the component. After every integration step, LJ beads whose centers entered the TR region were changed into tracers, and tracers that entered the Δ region where changed into LJ beads.

Nonequilibrium simulation protocol For the nonequilibrium simulations, we made use of the D-NEMD technique [84, 85] to generate an ensemble of trajectories from uncorrelated initial conditions. Both the AdResS and the full atomistic reference simulations followed the same protocol:

(i) Perform one equilibrium simulation at temperature $\overline{T} = (T_1 + T_2)/2$ and density $\overline{\varrho} = (\varrho_1 + \varrho_2)/2$. It yields the trajectory of a homogeneous fluid along which configurations are sampled every 40τ after an initial equilibration phase of $2{,}000\tau$.

(ii) Start non-equilibrium simulations from these samples. In the AdResS set-up, the two reservoirs for the equilibrium set-up at $(\overline{T}, \overline{\varrho})$ are replaced by one reservoir at (T_1, ϱ_1) and one at (T_2, ϱ_2), i.e., the thermostat temperature and the parameters of $F_{\text{th}}(x)$ are changed. For the full atomistic reference, only the thermostat is modified.

In the case of AdResS, the thermodynamic force was pre-computed for the three state points used. Note that the full atomistic simulations are not needed for AdResS simulations according to this protocol, they served as a benchmark reference merely.

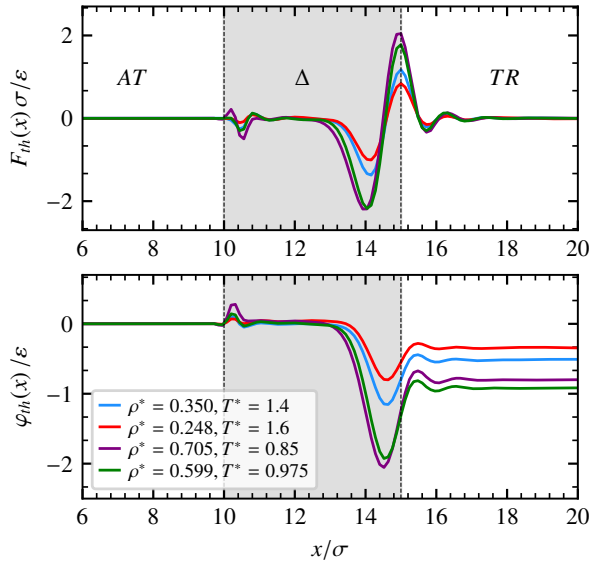

Figure 4.5: The thermodynamic forces $F_{\text{th}}(x)$ (top) and their corresponding potentials $\varphi_{\text{th}}(x)$ (bottom) along the x-axis for the four reservoir states used in the nonequilibrium simulations. It holds $F_{\text{th}}(x) = -\partial_x \varphi_{\text{th}}(x)$. By construction, $F_{\text{th}}(x) = 0$ in the AT region. The thermostat coupling rate was chosen as $\nu_{\text{coupl}} = 15\tau_{\text{LJ}}^{-1}$ for all four states.

Observables For the calculation of the spatial profiles of thermodynamic observables, the simulation box was partitioned into slab-like control volumes Ω_k of width 2.5σ and volume V_Ω along the x-axis ($k = 1,\ldots,48$). The temperature $T(x_k)$ at the position x_k in the center of Ω_k follows from the kinetic energy of the particles in Ω_k. The heat flux was obtained as $J(x_k) = V_\Omega^{-1} \sum_{i\in\Omega_k} (e_i + tr\vec{\sigma}_i)\vec{v}_i$ [84, 86] with $\vec{v}_i$ denoting the velocity of the i-th particle, e_i the sum of its kinetic and potential energies, and $tr\vec{\sigma}_i = -\frac{1}{2}\sum_{j\neq i} r_{ij}\, U'(r_{ij})$ the trace of the potential contribution of particle i to the stress tensor; $r_{ij} = |\vec{r}_i - \vec{r}_j|$ is the distance of separation between particles i and j.

After giving ample time for relaxation of the non-equilibrium setup ($3{,}750\tau$), the profiles were computed as time averages over samples taken every 0.3τ. The data shown in Fig. 3 (main text) and fig. 4.8 are averages over time, over the 4 independent nonequilibrium trajectories and the two independent AT regions in the simulation box.

4.1.7.2 AdResS simulations in equilibrium

In this section, we describe the procedure to calculate the thermodynamic force used in the AdResS set-ups and we give numerical evidence that the AT region of the set-up properly represents a grand canonical open system.

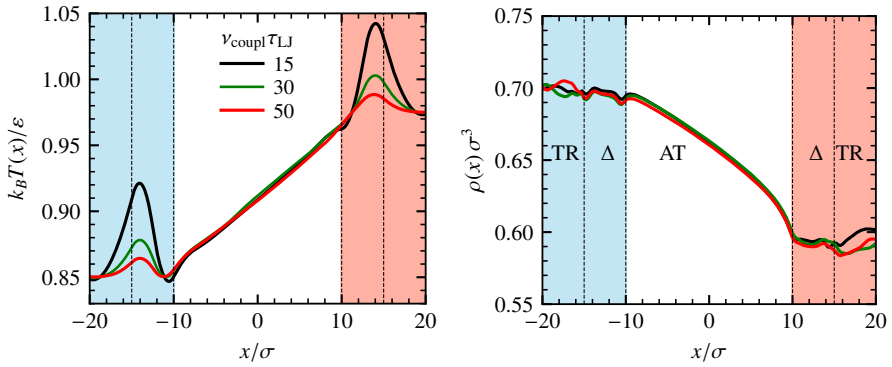

Figure 4.6: Profiles of temperature (left) and density (right) of the investigated LJ liquid in a stationary non-equilibrium state for three different coupling rates ν_{coupl}. The data for $\nu_{\mathrm{coupl}} = 50\tau_{\mathrm{LJ}}^{-1}$ are the same as shown in Fig. 3 of the main text.

Computation of the thermodynamic force The reservoirs of the AdResS set-up need to be calibrated to the fluid state they represent. To this end, a sequence of short equilibrium simulations is needed to self-consistently determine the thermodynamic force $F_{\mathrm{th}}(x)$ for the pair (T,ρ) of temperature and density of the fluid. The calculation occurs iteratively, starting from $F_{\mathrm{th}}(x) = 0$. The stationary density profile $\varrho(x)$ is computed across the AT, Δ, and TR regions for a given form of $F_{\mathrm{th}}(x)$, which is then updated to reduce gradients of the density (see Ref. [**advtsres**]). The iteration ends when the deviation of $\varrho(x)$ from the target density is within a prescribed tolerance. In this work, each iteration step consisted of an MD simulation over $4{,}000\tau$, where the first quarter was skipped in the calculation of $\varrho(x)$, allowing the fluid to adjust to the modified value of $F_{\mathrm{th}}(x)$. Whereas after about 7 iterations the deviation of the density profile from a constant had dropped below 3%, we ran about 50 iterations to achieve convergence within 1.5%. The resulting functional forms of $F_{\mathrm{th}}(x)$ and their corresponding potentials $\varphi_{\mathrm{th}}(x)$ are shown in fig. 4.5 for the four state points involved in the nonequilibrium AdResS set-ups used here. Finally, as $F_{\mathrm{th}}(x)$ depends on the thermostat coupling rate it was calculated separately for every value of ν_{coupl} used in fig. 4.6.

Validation of the AdResS set-up as an open system Here we report details for the AdResS simulations of the equilibrium fluids and corroborate numerically that the AT region of AdResS is indeed representing a physically well-defined open system. To this end, the following three conditions must be met by the AT region [38, 78]. Data are shown exemplarily for one fluid state only, the results of the other simulations are similar.

(1) The particle number density and the temperature must be uniform across the AT and Δ regions and, within a certain tolerance, be equal to their values of the desired thermodynamic state (fig. 4.7a).

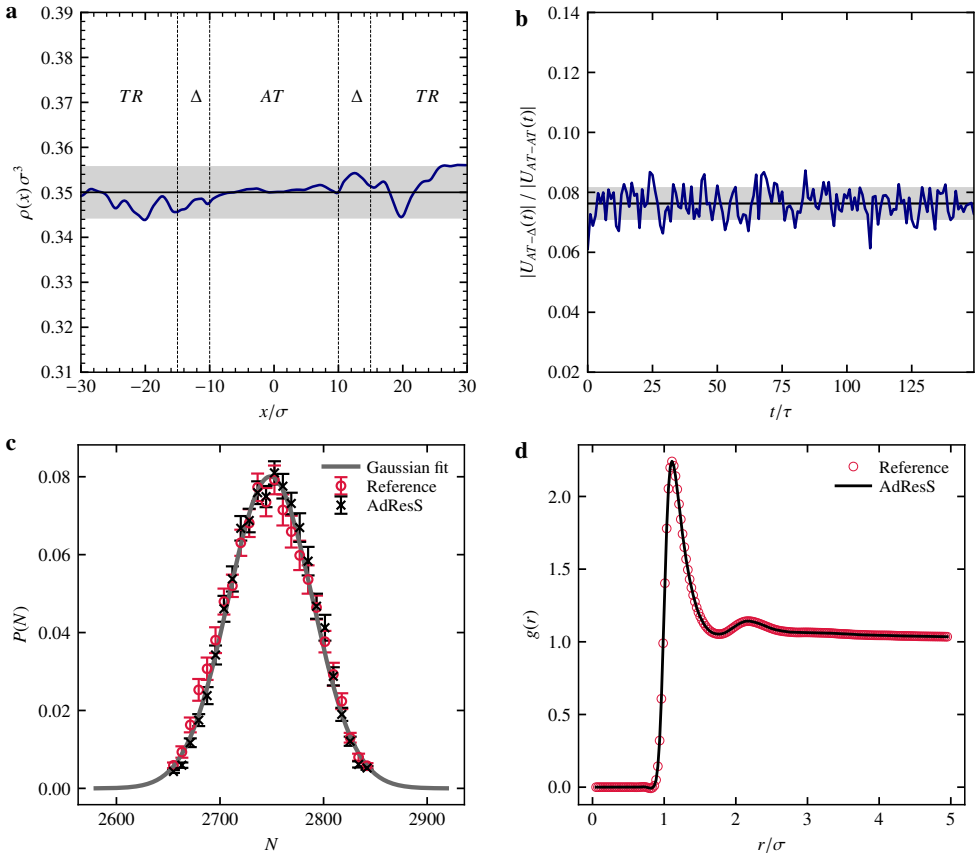

Figure 4.7: Numerical test of the equilibrium AdResS set-up for open-system simulations of a LJ fluid at temperature $T^* = 1.40$ and density $\varrho^* = 0.350$. Red circles refer to results of the full atomistic reference simulation, where the calculation was restricted to a subdomain that is equivalent to the AT region of the AdResS set-up. The panels follow the criteria described in Supplemental section 4.1.7.2: (a) stationary profile $\varrho(x)$ of the number density across the AdResS set-up (blue line) compared to the target density ϱ^* (black). The shaded area indicate a tolerance of ±1.5% around ϱ^*, which was the convergence criterion for the computation of the thermodynamic force. (b) Interaction energy $U_{\mathrm{AT}-\Delta}(t)$ of the AT region of interest with the reservoir relative to the potential energy $U_{\mathrm{AT}-\mathrm{AT}}$ due to the interactions within the AT subsystem, as a function of time. The energy contribution from the reservoir to the AT region is below 8% on average, with a standard deviation of 0.5%. (c) Probability distribution $P(N)$ of the fluctuating particle number in the AT region of the AdResS set-up (black crosses) compared with results of the reference simulation (red circles). The solid line is a Gaussian fit to the data. (d) Comparison of the radial distribution function $g(r)$ computed from the AT region of the AdResS set-up (black solid line) and from the full atomistic reference; here, the relative deviation is less then 0.3%.

(2) The interaction energy $U_{\mathrm{AT}-\Delta}$ of the particles in the AT region with the particles in the Δ region must be negligible relative to the interaction energy $U_{\mathrm{AT}-\mathrm{AT}}$ amongst the particles in the AT region (fig. 4.7b).

(3) The probability distribution $P(N)$ of the number of particles in the AT region must reproduce the distribution $P(N)$ obtained from an equivalent, open subdomain of the full atomistic reference simulation (fig. 4.7c).

From condition (1), we can conclude that, due to the combined action of the thermodynamic force and the thermostat in the Δ region, the AT region is at the same thermodynamic state point as the reference fluid of a full atomistic simulation. If condition (2) is satisfied, there are no sizable energy contributions in the AT region stemming from the reservoir. This criterion is usually employed in statistical mechanics texts in the definition of the grand canonical-like ensemble (see, e.g., [95]). As a consequence of condition (3), the particle statistics in the AT region is consistent with that of the reference case; in particular, the density (first moment of $P(N)$) and the compressibility (proportional to the variance) are the same. As a further cross-check, usually automatically fulfilled when conditions (1–3) are met, we have tested that the radial distribution function $g(r)$, obtained within the AT region, agrees tightly with the one calculated in the full atomistic simulation (fig. 4.7d). The quantitative criterion used in this work for the equivalence of the data from the AdResS and the full atomistic reference simulation is a tolerance of 1.5%, which is well met by the data shown in fig. 4.7.

4.1.7.3 Results for the supercritical fluid

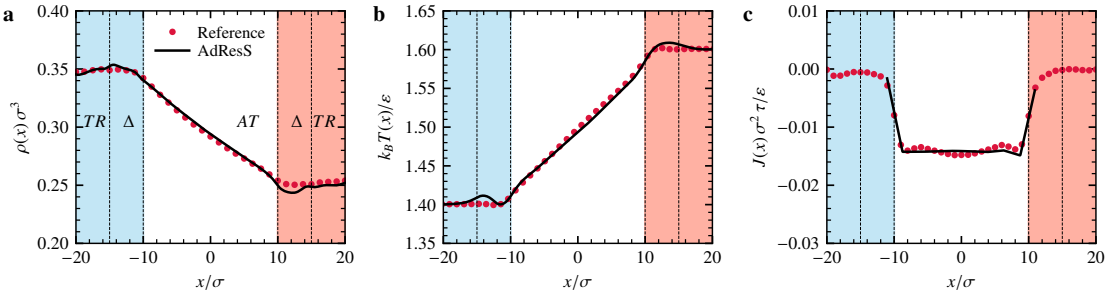

Figure 4.8: Results of the open-system simulation for a supercritical LJ fluid in a thermal gradient obtained from the nonequilibrium AdReS set-up (solid lines) and from a full atomistic simulation serving as reference (dots). Only a single AT region is shown, and parts of the tracer regions (TR) have been omitted for clarity. The panels display spatial profiles of (a) the particle number density $\varrho(x)$, (b) the temperature $T(x)$, and (c) the heat flux $J(x)$ as stationary responses to the nonequilibrium forcing.

4.2 Physio-mathematical model and numerical tests

Content reprinted from [23] (https://doi.org/10.1002/adts.202100071).

In a recently proposed computational model of open molecular systems out of equilibrium the action of different reservoirs enters as a linear sum into the Liouville-type evolution equations for the open system's statistics. The linearity of the coupling is common to different mathematical models of open systems and essentially relies on neglecting the feedback of the system onto the reservoir due to their interaction. In this paper, we test the range of applicability of the computational model with a linear coupling to two different reservoirs, which induces a nonequilibrium situation. To this end, we studied the density profiles of Lennard-Jones liquids in large thermal gradients using nonequilibrium molecular dynamics simulations with open boundaries. We put in perspective the formulation of an extension of the mathematical model that can account for nonlinear effects.

4.2.1 Introduction

Theory and modeling of open systems are becoming increasingly prominent since they allow one to focus on the relevant regions where a process of interest is taking place. The exterior can be instead simplified in the form of thermodynamic reservoirs of particles and energy and is controlled by few macroscopic variables [78]. In particular, open molecular systems are of relevance because of their occurrence in a variety of current cutting edge technologies, thus they require well-founded numerical algorithms for their efficient and accurate numerical simulation [38].

In this perspective, physico-mathematical models of open systems represent a guideline protocol for the development of simulation algorithms. Established models such as the one by Bergmann and Lebowitz [33, 34] (BL) express the combined actions of the reservoirs in the Liouville-like equation of the statistical evolution of the open system by adding the contributions of each single reservoir linearly and independently [cf. eq. (4.3) below]. The linearity for the coupling is a direct consequence of the assumption of impulsive interactions between system and reservoirs, that is each interaction is considered a discrete event in time so that the open system interacts separately in time with each reservoir. The linearity of action is also an assumption in the thermodynamic-based model presented by [96] (GBY). There, the system interacts with different external "ports" each of which is a source of energy and mass and mechanical work, and the resulting model is built by adding up the contribution of each port. Both models are based on a drastic *a priori* simplification of the reservoirs,

whose microscopic origin is neglected, thus ruling out the possibility of nonlinear effects in the coupling.

Two of the authors[97] have recently proposed a model, inspired by a simulation protocol for open systems, where the microscopic character of the reservoir is taken into account. In a large system (Universe) the degrees of freedom of the particles of the reservoir are analytically integrated out and an equation for the statistical evolution of the open system is derived. The original derivation considers an open system embedded in a single homogeneous reservoir, but the extension to more than one reservoir is straightforward and is reported in the appendix. Also in this model the combined actions of the reservoirs in the equation of statistical evolution of the open system enters as the sum of action of each single reservoir. Differently from the other models reported above, this model is not constructed on an *a priory* choice of a linear sum of reservoir actions. Rather, the latter originates from the hypotheses of (i) two-body short range interactions between the particles and (ii) of statistical independence of the states of reservoir particle residing close to the open system boundary. As a consequence the coupling between the open system and each reservoir occurs only at the interface regions and thus the contribution of each reservoir is reduced to a surface integral at the interface region.

In a recent work, we have embedded the idea of adding the actions of independent, concurrent reservoirs in the Adaptive Resolution Simulation approach (AdResS) [17, 25, 98] and treated the case of an open system interfaced with two distinct and disjoint reservoirs at different temperatures [22]. The encouraging results of Ref. [22] raise the question about the range of validity of the linear approximation of the reservoir action. In this paper, we test the quality of the numerical approach based on the AdResS technique, which rests solely on the additivity of the reservoir contributions. The test consists in simulating a Lennard-Jones (LJ) liquid in an open domain set up such that there is a feedback of the open system onto a sizable part of two attached reservoirs. We compare the results of our model with the results of a reference simulation of the Universe in which all particles are explicitly treated with all their degrees of freedom, but are thermalized at different temperatures in subregions equivalent to the reservoir domains of our model. With such a comparison we conclude about the numerical applicability of the linear approximation. Surprisingly, for a LJ liquid at thermodynamic and gradient conditions common to a large variety of situations in chemical physics, it is shown that the linear hypothesis holds and nonlinear effects are numerically negligible. This is a promising insight in the perspective of developing accurate and efficient simulation algorithms.

While encouraging from the numerical point of view, our conclusions also call for a further development of the mathematical models. The BL and the GBY models by construction cannot

implement a boundary response of the reservoir, instead generalizations to nonlinear and memory effects are within the scope of the other model when less restrictive conditions on the range of particle–particle interactions and on the statistics of reservoir states close to the open system boundary are adopted. For example, it is known rigorously [99] that, just as a consequence of multidimensional wave propagation in the reservoir, a nonreflecting acoustic boundary condition *must* entail memory effects. Moreover, when the single- and two-particle statistics involving reservoir particles close to the system boundary are permitted to depend on the state of the open system as a whole, then nonlinear effects will arise in addition as discussed in section 4.2.5. Such nonlinear and memory effects of the reservoirs are covered only qualitatively here, while a detailed analysis is left for future work.

4.2.2 Mathematical models of open system

4.2.2.1 Bergmann-Lebowitz model

The linear coupling of the open system to distinct reservoirs is the starting point of relevant mathematical models that describe the exchange of matter and energy of a system with its surroundings (see, e.g., Refs.[33, 34, 96] and references therein). For example, in the well-established BL model [33, 34], the Liouville equation for the phase space density $f_n(\boldsymbol{X}_n, t)$ of the open system with n particles assumes *a priori* the linear sum of the action of m different reservoirs:

$$\frac{\partial f_n(t,\boldsymbol{X}_n)}{\partial t} + \{f_n(t,\boldsymbol{X}_n), H_n(\boldsymbol{X}_n)\} = \sum_{r=1}^{m} I_{n,r}^{(\mathrm{BL})}[\boldsymbol{X}_n, \{f_{n'}(t)\}], \tag{4.3}$$

where $\{\cdot,\cdot\}$ denotes the Poisson bracket, $H_n(\boldsymbol{X}_n)$ is the n-particle Hamiltonian, and the action of the r-th reservoir depends on the family $\{f_{n'}(t)\}_{n'\geqslant 0}$ of phase space densities at time t and is given by the functional

$$I_{n,r}^{(\mathrm{BL})}[\boldsymbol{X}_n, \{f_{n'}(t)\}] = \sum_{n'=0}^{\infty} \int \left[K_{nn'}^{r}(\boldsymbol{X}_n, \boldsymbol{X}'_{n'}) f_{n'}(\boldsymbol{X}'_{n'}, t) - K_{n'n}^{r}(\boldsymbol{X}'_{n'}, \boldsymbol{X}_n) f_n(t, \boldsymbol{X}_n)\right] d\boldsymbol{X}'_{n'}. \tag{4.4}$$

Each system–reservoir coupling is assumed to consist of an impulsive interaction formalized by a Markovian kernel, $K_{nn'}(\boldsymbol{X}'_{n'}, \boldsymbol{X}_n)$, i.e., a transition probability per unit time from an n-particle (open system) and phase space configuration $\boldsymbol{X}_n$ to n' particles and phase space configuration $\boldsymbol{X}'_{n'}$. The overall global effect resulting from the interactions of the open system with its surrounding is assumed to be linear as expressed by the sum over the $I_{n,r}^{(\mathrm{BL})}$ in eq. (4.3) and each term being linear in the f_n. This linearity is actually implicit in the assumption of impulsive and independent interactions. [33, 34] also note that the model of impulsive interaction represents only an asymptotic limit which is not always realized.

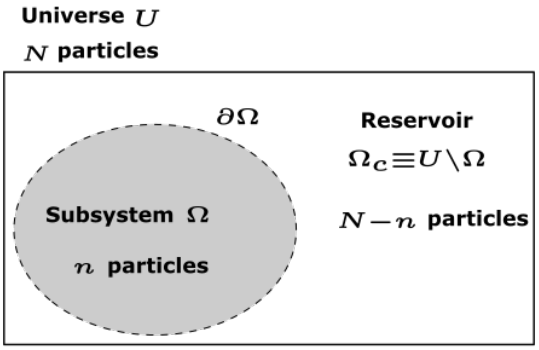

Figure 4.9: The partitioning of the "Universe" into the open system Ω and the reservoir $\Omega_c \equiv U \setminus \Omega$. The number of particles in the universe is fixed to N, but it can fluctuate in the domain Ω due to exchange with the reservoir.

4.2.2.2 The thermodynamic model of Gay-Balmaz and Yoshimura

A thermodynamic perspective to justify a linear coupling is instead employed by Gay-Balmaz and Yoshimura [96], using a Lagrangian formulation of the dynamic many-particle system. In their model, the system interacts with different "ports" each of which is a source of energy and mass and mechanical work that can be injected into or adsorbed from the system. The resulting global model is built by adding up the contribution of each port. Such a modeling approach is justified by the application of the first principle of thermodynamics expressed by a time-dependent energy of the system due toehe action of the ports:

$$\frac{dE}{dt} = \sum_{r=1}^{m} \left(P_{W,r}^{\text{ext}} + P_{H,r}^{\text{ext}} + P_{M,r}^{\text{ext}} \right), \tag{4.5}$$

where $P_{W,r}^{ext}$ is the power corresponding to the work done by the r-th reservoir on the system and $P_{H,r}^{ext}$ and $P_{M,r}^{ext}$, respectively, are the power corresponding to the heat and matter transfer from the r-th reservoir to the system.

4.2.2.3 Model with marginalization of the degrees of freedom of the reservoir

In this section we report the essential features of the model developed in Ref. [97], which are required for the discussion about the linear action of concurrent reservoirs. An extended explanation of the model and its extension to the case of many concurrently acting reservoirs at different thermodynamic conditions are reported in section 4.2.7 and section 4.2.8. The model considers a large closed system of N particles, the "Universe" U (fig. 4.9). The Universe is statistically described by its phase space density function $F_N(t, \boldsymbol{X}^N)$, where t is the time variable and $\boldsymbol{X}^N$ are the $6N$-dimensional coordinates in phase space $S^N = \Omega^N \times \mathbb{R}^{3N}$. The time

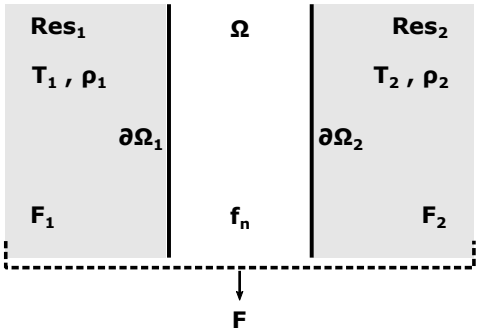

Figure 4.10: The partitioning of the "universe" in two large reservoirs, Res_1 and Res_2, and the subsystem of interest, Ω. The boundary of the open system splits according to $\partial\Omega \equiv \partial\Omega_1 \cup \partial\Omega_2$ into the boundary surface $\partial\Omega_1$ between Res_1 and Ω and the boundary surface $\partial\Omega_2$ between Res_2 and Ω. The two reservoirs are set up at different thermodynamic conditions, e.g., different densities, ϱ_1 and ϱ_2, and different temperatures, T_1 and T_2.

evolution of $F_N(t, \boldsymbol{X}^N)$ follows the corresponding Liouville equation. A subsystem $\Omega \subset U$ of the Universe with n particles is described by the probability distribution function, $f_n(t, \boldsymbol{X}^n)$, obtained by marginalizing $F_N(\boldsymbol{X}^N)$ w.r.t. the $N-n$ particles located in the reservoir $\Omega_c = U \setminus \Omega$:

$$f_n(t, \boldsymbol{X}^n) = \binom{N}{n} \int\limits_{S_c^{N-n}} F_N(t, \boldsymbol{X}^n, \boldsymbol{\Xi}_n^N)\, d\boldsymbol{\Xi}_n^N; \tag{4.6}$$

$\boldsymbol{\Xi}_n^N$ indicates the degrees of freedom in the reservoir phase space $S_c^{N-n} = \Omega_c^{N-n} \times \mathbb{R}^{3(N-n)}$. The binomial factor is chosen such that the hierarchy of phase space densities $\{f_n\}_{0 \leqslant n \leqslant N}$ satisfies the normalization condition $\sum_{n=0}^{N} \int_{S^n} f_n(t, \boldsymbol{X}^n)\, d\boldsymbol{X}^n = 1$. The procedure of marginalization is then applied to the Liouville equation of $F_N(\boldsymbol{X}^N)$, leading to a hierarchy of equations for the $f_n(t, \boldsymbol{X}^n)$:

$$\frac{\partial f_n}{\partial t} + \{f_n, H_n\} = \Psi_n + \Phi_n^{n+1}; \quad 0 \leqslant n \leqslant N, \tag{4.7}$$

where the r.h.s. represents the coupling between the system Ω and the exterior. Specifically, $\Psi_n = \Psi_n[\boldsymbol{X}^n, f_n]$ stems from the forcing of the system particles by the reservoir and $\Phi_n^{n+1} = \Phi_n^{n+1}[\boldsymbol{X}^{n+1}, f_n, f_{n+1}]$ describes the exchange of one particle between the system and the reservoir.

The derivation above is done under the assumption that the reservoir is thermodynamically uniform. However, one can imagine that the exterior of Ω is formed by m disjoint regions at different thermodynamic conditions (see fig. 4.10 for an example for two regions). Let us assume that the two regions acting as reservoirs are large enough so that we can consider each

of them to be in a stationary state within the time scale of observation that we are considering. In such a case, eq. (4.7) becomes:

$$\frac{\partial f_n}{\partial t} + \{f_n, H_n\} = \sum_{r=1}^{m} \left(\Psi_{n,r} + \Phi_{n,r}^{n+1}\right), \tag{4.8}$$

where the sum over r expresses the additive effect of the m reservoirs. The detailed derivation of (4.8) along the lines of Ref.[97] is conceptually simple, but involves few specific modifications of the model at the different boundaries of Ω; a step by step derivation is given in section 4.2.8. Most importantly, the contributions Ψ_n, r and $\Phi_{n,r}^{n+1}$ are linear in the f_n and (4.8) formally resembles eq. (4.3).

4.2.3 The AdResS setup with the linear combination of reservoirs

In a recent work [22], we have employed the Adaptive Resolution Simulation technique (AdResS) for molecular dynamics [17] to test the concept of a linear combination of reservoir actions on an open system. The AdResS setup consists of partitioning the simulation box in three regions: the region of interest AT, at full atomistic resolution, the interface region Δ, at full atomistic resolution, but with additional coupling features to the large reservoir, and TR, the large reservoir of noninteracting particles (fig. 4.11). Particles can freely cross the boundaries between the different regions and automatically acquire the molecular resolution that characterize the region in which they are instantaneously located.

Regarding the coupling conditions, molecules of the AT region interacts with atomistic potentials among themselves and with molecules in Δ, and vice versa, while there is no direct interaction with the tracer particles. Tracers and molecules in Δ are subject to an additional one-body force, named thermodynamic force, which acts along the direction $\vec{n}$ perpendicular to the Δ/TR interface, $\vec{F}_{\rm th}(\vec{q}) = F_{\rm th}(\vec{q})\vec{n}$ for positions $\vec{q}$. In essence, this is the coupling condition between the Δ region and the reservoir TR, amended by a thermostat in these regions. As a consequence the total potential energy reads: $U_{\rm tot} = U_{\rm tot}^{\rm AT} + \sum_{\vec{q}_j \in \Delta \cup {\rm TR}} \varphi_{\rm th}(\vec{q}_j)$ with the potential $\varphi_{\rm th}(\vec{q})$ such that $\vec{F}_{\rm th}(\vec{q}) = -\nabla\varphi_{\rm th}(\vec{q})$ and $\varphi_{\rm th}(\vec{q}) = 0$ in the AT region, $\vec{q} \in$ AT. The thermodynamic force is derived by basic principles of statistical mechanics; in essence, of relevance for this paper, it assures that the particle density in the atomistic region is equal to a value of reference. As it is shown in Refs.[24, 79, 98, 100] the constraint on the particle density in AdResS implies the equilibrium of the atomistic region w.r.t. conditions of reference of a fully atomistic simulation.

The setup of AdResS resembles the partitioning employed in the mathematical models of open system and, in particular, it is very well suited for a numerical test of the idea of a linear action

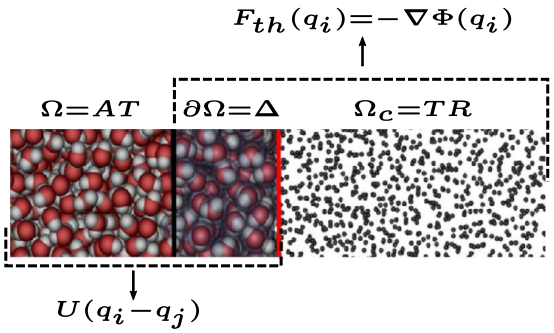

Figure 4.11: The AdResS setup consists of an atomistic region AT and an interface region Δ, both where molecule i interacts with molecule j through the pair potential $U_{ij} = U(\vec{q}_i - \vec{q}_j)$. The Δ region is interfaced (to the right) with a large reservoir TR of noninteracting particles (tracers). In the $\Delta \cup$ TR region, the thermodynamic force, $F_{\text{th}}(\vec{q}_i)$, acts on all particles individually to enforce the desired thermodynamic equilibrium. The correspondence with the mathematical model of open systems is illustrated by identifying each region of AdResS with the equivalent region of figs. 4.9 and 4.10.

of reservoirs. In fact, in AdResS one can implement a setup as that of fig. 4.10, where the action of the two distinct reservoirs, Res_1 and Res_2, is encoded in two distinct coupling conditions at the corresponding interfaces. The coupling terms, which correspond to the thermodynamic forces, are calculated separately; that is, the system first interacts only in the presence of Res_1, which is at temperature T_1 and density ϱ_1, and one obtains the thermodynamic force needed at the interface with Res_1. Next, the system interacts only in the presence of Res_2, at $T = T_2$ and $\varrho = \varrho_2$, and one obtains the thermodynamic force needed at the interface with Res_2. A nonequilibrium situation is then achieved by running a simulation setup with distinct thermodynamic forces applied in the corresponding interface regions (fig. 4.12).

4.2.4 Numerical tests of the linear approximation of the reservoir action

The AdResS approach to open systems out of equilibrium was applied to simulate a LJ liquid in a temperature gradient [22]. The results of this earlier study showed that indeed the model accurately reproduces data from fully atomistic reference simulations in the presence of a thermal gradient. Specifically, an isobaric setup was employed, that is the temperature gradient is applied at constant pressure by choosing reservoir densities along an isobar for prescribed reservoir temperatures. Here we go further and consider situations where the idea of linearity is pushed to its edge of validity. To this aim, we numerically test what happens in the atomistic region of interest when at the interface regions one has a feedback from the rest of the system. We performed nonequilibrium simulations (i) along an isobar with increasing temperature gradients, whose largest value exceeds the one of our earlier work [22] by a factor of 3 and (ii) in an isochoric setup, that is, the thermodynamic forces are calculated at the same

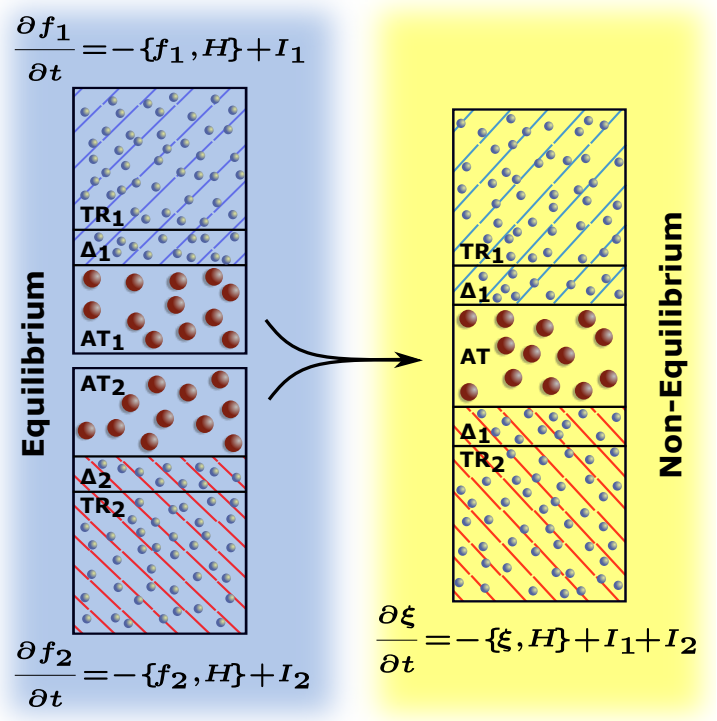

Figure 4.12: Schematic illustration of the simulation of a thermal gradient in the AdResS setup and its correspondence to the mathematical models. First, the open system is equilibrated at the thermodynamic condition of each reservoir (left). In AdResS, this corresponds to running the equilibration procedure twice to determine the thermodynamic force $F_{\text{th},1}(\vec{q})$ and $F_{\text{th},2}(\vec{q})$ separately. Once the system is in contact with two different reservoirs (right), then the mathematical models predict a linear action of the reservoirs as is apparent from the r.h.s. $I_1 + I_2$ of the extended Liouville equation eqs. (4.3) and (4.8). The reservoir coupling terms I_r $(r = 1,2)$ translate in AdResS to the combined action of $F_{\text{th},1}(\vec{q})$ and a thermostat that maintains the temperature at T_1 in the region $\Delta_1 \cup \text{TR}_1$ and analogously for the second reservoir; in this sense, I_r is a function of $F_{\text{th},r}(\vec{q})$ and the thermostat at T_r.

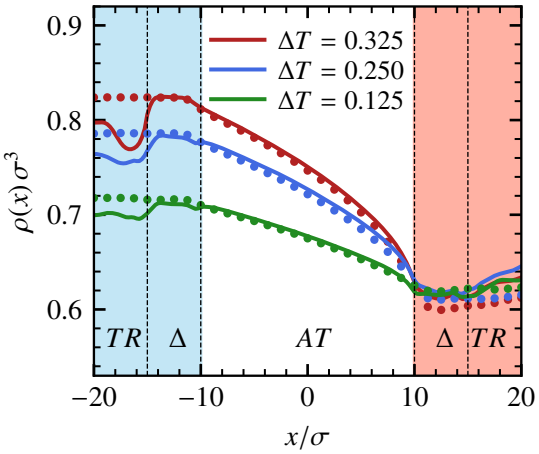

Figure 4.13: Density profiles of a LJ liquid in different thermal gradients, simulated with the isobaric setups of nonequilibrium AdResS (solid lines). The temperature difference ΔT between the hot (red) and cold (blue) reservoirs increases from bottom to top as indicated in the legend. The temperature and density of the hot reservoir are kept fixed at $T_{\text{hot}} = 0.95\varepsilon/k_B$ and $\varrho_{\text{hot}} = 0.622\sigma^{-3}$, respectively, while the state points of the cold reservoir are chosen along the corresponding isobar. Here, ε and σ refer to the parameters of the LJ potential, see section 4.2.9. Reference results from full atomistic simulations are given by disc-shaped symbols. Only the parts of the TR regions close to the coupling boundary are shown.

density $\bar{\varrho} = \varrho_1 = \varrho_2$, but different reservoir temperatures $T_1 < T_2$. We note that the reservoir states are chosen in the liquid phase and are close to the liquid–vapour binodal curve; here, the LJ fluid is almost incompressible and is characterized by low pressure. The technical details of the simulations are given in section 4.2.9.

For the isobaric setup, case (i), the density profiles across the simulation box obtained for different thermal gradients (fig. 4.13) follow closely the results of the corresponding, fully atomistic reference simulations (which involves the atomistic simulation of a huge reservoir), in particular in the region AT of interest. The highly satisfactory agreement is qualitatively similar for all temperature gradients investigated, despite $\Delta T := T_2 - T_1$ increasing from 14% to 40% relative to the respective mean temperature, $\bar{T} = (T_1 + T_2)/2$. In the $\Delta \cup$ TR there are noticable effects due to a feedback of the system onto the reservoir, without repercussions on the region of interest.

For the isochoric nonequilibrium setup, case (ii), one expects that the thermal gradient induces a pressure gradient in the AT region. Interestingly, our simulation results (fig. 4.14) instead exhibit a density gradient that closely follows the one of the isobaric AdResS setup and the full atomistic reference. A possible explanation is that the pressure gradient induces a mass flux, which builds up a density gradient until the pressure differences are compensated. The interpretation is corroborated by the large density difference between the two TR regions,

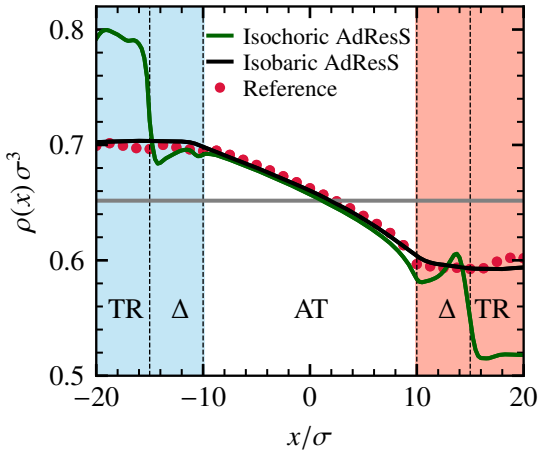

Figure 4.14: Density profiles of a LJ liquid in a fixed thermal gradient ($\Delta T = 0.125\varepsilon/k_B$) simulated with the isochoric (green line) and isobaric (black line) setups of nonequilibrium AdResS; reference data from full atomistic simulations are given by red symbols. The temperature of the hot reservoir is $T_{\text{hot}} = 0.975\varepsilon/k_B$, and the mean particle density, averaged over the whole setup, is $\bar{\varrho} \approx 0.65\sigma^{-3}$ (grey line). Only parts of the TR regions are shown.

reflecting tracers that were moved in excess from the hot to the cold reservoir. This mechanism introduces a feedback on the two reservoirs and yields a sizeable shift of their intended densities. Nevertheless, also the isochoric AdResS setup provides a meaningful (and simpler) approach to nonequilibrium simulations. It shall be added that the temperature profiles of all AdResS setups considered in figs. 4.13 and 4.14 agree extremely well with the simulations of reference and are not shown here, see Ref.[22] for an example.

4.2.5 Theoretical perspectives

From the physical point of view, both the BL and GBY models rely on neglecting any feedback of the system onto the reservoirs. The former model also predicts a linear combination of the action of different reservoirs as long as the condition of short range pair interactions and the explicit assumption of statistical independence of reservoir states from the open system states apply. However, such constraints can be relaxed and nonlinear and memory effects can be introduced into the derivation. Both types of effects are expected in general, as the following examples demonstrate:

1. Memory effects: We are dealing with thermodynamically compressible systems supporting sound waves. It is known from the theory of fluid dynamics that the modelling of acoustic waves that exit an open domain without reflection at its boundary demand that one keeps track of the system's history to properly capture the wave dynamics in the reservoir[99].

2. Nonlinearities: When the open system is at a higher pressure than the reservoir(s) initially, then the velocity statistics of outer particles near the open system boundary is clearly biased towards the outward pointing normal. This effect could be modelled by introducing single- and two-particle statistics $f^{\circ}_{n,1}$ and $f^{\circ}_{n,2}$ that depend explicitly on the particle number n of the open system and by coupling these functions to thermodynamic averages of the entire hierarchy of phase space densities f_ν, $\nu \in \{0,...,N\}$. This ansatz will render the terms Ψ_n and Φ_n^{n+1} in eq. (4.8) nonlinear functions of the f_n. If nonlinear effects are to arise in the presence of long-range interactions, then the model would similarly be able to account for these.

3. Long-range correlations: Another possibility is that, in the vicinity of a critical point, the correlation length of the fluid is of the order of the linear size of the open system. In this case, the presence of the open boundaries (i.e., the finite size of the subsystem) unavoidably modifies the observed fluid properties, e.g., its thermodynamics [101] and the strength of local density fluctuations [15, 102], and one anticipates a direct correlation between the reservoirs. Truncating such a correlation spectrum is known to give rise to critical Casimir forces: an effective, non-additive interaction between the boundaries, which was found for (binary) fluids between solid and periodic boundaries near criticality [103–105], but also transiently after a temperature quench [106]. Capturing such an extreme situation by a model of open systems would require that detailed information about the reservoir states is kept, with the degree of detail depending on the observables of interest.

Yet, the model of Ref.[97] tells something more. Even within the assumption of short-range interactions, one still needs basic information about the reservoirs at the interface, e.g., one- and two-particle distributions. These latter are assumed to be stationary, under the approximation that the reservoir, due to its size, fully controls the particle distribution at the surface. Such an approximation is no more valid if the range of interaction is extended because the system itself starts to significantly influence the distribution of particles near the boundary and a generally nonlinear feedback between the reservoirs is to be expected.

4.2.6 Conclusions

We have discussed models of open systems that rely on the linear combination of the actions of several reservoirs. From the general discussion emerges the necessity of considering the scenario in which nonlinear effects arise once the hypotheses of short range potentials and statistical independence of the reservoirs becomes less strict. In such a perspective, a model recently proposed by two of the authors offers the possibility of automatically including the

feedbacks between the open system and the attached reservoirs by generalizing the pertinent models of the reservoir statistics at each interface. Such a possibility is ruled out in the other models of an open system covered here. An analytic derivation of such a generalization is, however, left to future research. Instead we have focused on the numerical consequences of such nonlinear effects and reported a numerical test where the reference simulation automatically includes nonlinear effects while the simulation mimicking the mathematical model of eq. (4.8) does not include such a nonlinearity. The results show that even under such conditions, the approximation of a linear combination of actions yields numerically satisfying results for a range of systems of interest. This is good news for the numerical simulations, in particular, it removes the need to fine-tune the reservoir states of the isobaric setup. At the same time, our findings also call for an extension of the concepts and its numerical counterpart to nonlinear effects. In fact in this paper we have validated the model for a molecular system with Lennard-Jones-like short-ranged potentials, however the current conclusions may not apply to systems characterized by long-ranged interactions. In such a case, non-linear effects at the coupling boundary may become relevant. One example are ionic liquids, where electrostatics plays a major role. The AdResS approach was shown to describe such liquids in equilibrium in a highly satisfactory manner [107–109], and it will be interesting, in perspective, to test whether the current non-equilibrium set up of AdResS would be directly applicable to ionic liquids in a thermal gradient, or whether modifications at the coupling boundaries are needed.

4.2.7 Appendix A: Liouville-type equations for an open system

In this appendix, we summarize the key steps of the modeling procedure adopted in Ref.[97] for an open system embedded in a single uniform reservoir. This serves as basis for the extension of the model to several independently acting reservoirs in section 4.2.8.

4.2.7.1 Topological definition of an open system

Let us consider the open system schematically illustrated in fig. 4.9. The total system, here called "Universe", is characterized by the number N of particles (fixed) and a spatial domain U. A subdomain $\Omega \subset U$ defines the open system, which may contain any number $n \in \{0, ..., N\}$ of particles, while the region of the reservoir corresponds to the complement $U \setminus \Omega \equiv \Omega_c$ with $N - n$ particles. The phase space of the N particles in U is $S^N = U^N \times \mathbb{R}^{3N}$ (positions in U^N, momenta in $\mathbb{R}^{3N}$), the phase space of the open system is in case of n particles is $S^n = \Omega^n \times \mathbb{R}^{3n}$, and the phase space of the reservoir is $S_c^{(N-n)} = \Omega_c^{(N-n)} \times \mathbb{R}^{3(N-n)}$.

4.2.7.2 Relevant quantities that characterize U

The Universe is characterized by the Hamiltonian

$$H_N(\mathbf{q}^N, \mathbf{p}^N) = E_{\text{kin}}(\mathbf{p}^N) + V_{\text{tot}}(\mathbf{q}^N) \equiv \sum_{i=1}^{N} \frac{(\vec{p}_i)^2}{2M} + \frac{1}{2} \sum_{\substack{i,j=1 \\ j \neq i}}^{N} V(\vec{q}_j - \vec{q}_i) \tag{4.9}$$

where $\left(\mathbf{q}^N, \mathbf{p}^N, \right) = (\vec{q}_1, ..., \vec{q}_N, \vec{p}_1, ..., \vec{p}_N)$ and $(\vec{q}_i, \vec{p}_i)$ are the position and momentum of the i-th particle, respectively, M is the particle mass, assumed to be the same for all particles here, and V is the two-body interaction potential (as typical for, e.g., molecular dynamics simulations). The statistical mechanics description of the system in phase space is achieved through its probability density defined as

$$F_N : \mathbb{R}^+ \times S^N \to \mathbb{R}, \quad (t, \boldsymbol{X}^N) \mapsto F_N(t, \boldsymbol{X}^N), \tag{4.10}$$

with normalization $\int_{S^N} F_N \, d\boldsymbol{X}^N = 1$. The probability density of the Universe is subject to the transport equation of the phase space density (Liouville equation)

$$\frac{\partial F_N}{\partial t} = \sum_{i=1}^{N} \left[\nabla_{\vec{q}_i} \cdot \left(\vec{v}_i F_N \right) + \nabla_{\vec{p}_i} \cdot \left(-\nabla_{q_i} V_{\text{tot}}(\vec{q}^N) F_N \right) \right] \equiv -\{F_N, H_N\} \tag{4.11}$$

where the r.h.s. is a Poisson bracket and $\vec{v}_i = \vec{p}_i / M$ the velocity of the i-th particle.

4.2.7.3 Relevant quantities that characterize Ω

The open system Ω containing n particles is characterized by the Hamiltonian

$$H_n = \sum_{i=1}^{n} \frac{(\vec{p}_i)^2}{2M} + \frac{1}{2} \sum_{\substack{i,j=1 \\ j \neq i}}^{n} V(\vec{q}_j - \vec{q}_i); \qquad (\vec{q}_i, \vec{q}_j \in \Omega). \tag{4.12}$$

The statistical mechanics description of the open system in phase space is given by the collection of all its n-particle probability densities

$$f_n : \mathbb{R}^+ \times S^n \to \mathbb{R}, \quad (t, \boldsymbol{X}^n) \mapsto f_n(t, \boldsymbol{X}^n), \tag{4.13}$$

for $n \in \{0, ..., N\}$. Consistent with the fact that Ω is a subsystem of U, f_n is explicitly given by [97]:

$$f_n(t, \boldsymbol{X}^n) = \binom{N}{n} \int_{(S_c)^{N-n}} F_N(t, \boldsymbol{X}^n, \boldsymbol{\Xi}_n^N) \, d\boldsymbol{\Xi}_n^N \tag{4.14}$$

with $\Xi_n^N \equiv [X_{n+1}, ...X_N]$ collecting the reservoir's degrees of freedom, $X_i = (\vec{q}_i, \vec{p}_i) \in S_c$, and the normalization condition: $\sum_{n=0}^{N} \int_{S^n} f_n(t, \boldsymbol{X}^n)\, d\boldsymbol{X}^n = 1$. The binomial factor counts the number of ways to pick n particles out of N.

4.2.7.4 Derivation of a Liouville-like equation for Ω

The starting point is eq. (4.11) and the strategy to achieve a Liouville-like equation for f_n consists in the marginalization of eq. (4.11) w.r.t. the degrees of freedom of the $N-n$ particles in Ω_c. The procedure can be schematized by the following two steps

I) Marginalization of the term $\sum_{i=1}^{N} \nabla_{\vec{p}_i} \cdot \left(-\nabla_{q_i} V_{\text{tot}}(\vec{q}^N) F_N\right)$. Since $V_{\text{tot}}(\vec{q}^N)$ is a sum over all index pairs $1 \leqslant i, j \leqslant N$, one needs to analyze three specific situations:

$$(a) \quad i, j \in \Omega_c; \qquad (b) \quad i, j \in \Omega; \qquad (c) \quad i \in \Omega, j \in \Omega_c. \tag{4.15}$$

II) Marginalization of the term $\sum\limits_{i=1}^{N} \nabla_{\vec{q}_i} \cdot \left(\vec{v}_i F_N\right)$, where two specific situations need to be distinguished:

$$(a) \quad i \in \Omega \qquad \text{and} \qquad (b) \quad i \in \Omega_c\,. \tag{4.16}$$

Results of step I

(a) For all particle indices i in the reservoir, $n+1 \leq i \leq N$, Gauss' theorem implies:

$$\int\limits_{B_r(0)} \nabla_{\vec{p}_i} \cdot \left(\nabla_{q_i} V_{\text{tot}}(\boldsymbol{q}^N) F_N(t, \boldsymbol{q}^N, \boldsymbol{p}^N)\right) d^3 p_i$$
$$= \int\limits_{\partial B_r(0)} \vec{n} \cdot \left(\nabla_{q_i} V_{\text{tot}}(\boldsymbol{q}^N)\right) F_N(t, \boldsymbol{q}^N, \boldsymbol{p}^N)\, d\sigma_{p_i} \to 0 \tag{4.17}$$

as $r \to \infty$, where $B_r(0)$ is the sphere of radius r in momentum space centered at the origin and $\vec{n}$ the surface normal on $\partial\Omega$ pointing outwards. It is assumed that F_N decays sufficiently rapidly for large $|\vec{p}_i|$ for the boundary integral to vanish in the limit. This is certainly true, e.g., for the Boltzmann distribution of the momenta, $F_N \propto \exp\left(-(\vec{p}_i)^2/2Mk_BT\right)$. Actually, it is sufficient that F_N decays to zero at all for large momenta and this is a consequence of F_N being a probability density and thus integrable.

(b) If both particles i, j are in the open system Ω, $1 \leqslant i, j \leqslant n$, marginalization over the

reservoir yields:

$$\binom{N}{n}\int\limits_{(S_c)^{N-n}} \nabla_{\vec{p}_i}\cdot\Big(\nabla_{q_i}V(\vec{q}_i-\vec{q}_j)F_N(t,\boldsymbol{X}^n,\boldsymbol{\Xi}_n^N)\Big)d\Xi_n^N$$
$$=\nabla_{\vec{p}_i}\cdot\Big(\nabla_{q_i}V(\vec{q}_i-\vec{q}_j)f_n(t,\boldsymbol{X}^n)\Big). \quad (4.18)$$

(c) If particle i is in the open system, $1\le i\le n$, but particle j is in the reservoir, $n+1\le j\le N$, then choosing $i=n$ and $j=n+1$ for the ease of notation, one finds:

$$\binom{N}{n}\int\limits_{S_c}\int\limits_{(S_c)^{N-n-1}} \nabla_{\vec{p}_i}\cdot\Big(-\nabla_{q_i}V(\vec{q}_i-\vec{q}_j)F_N(t,\boldsymbol{X}^{n-1,},X_i,(\vec{q}_j,\vec{p}_j),\boldsymbol{\Xi}_{n+1}^N)\Big)d\boldsymbol{\Xi}_{n+1}^N dp_j dq_j$$
$$=\nabla_{\vec{p}_i}\cdot\Big(\vec{F}_{\mathrm{av}}(\vec{q}_i)f_n(t,\boldsymbol{X}^{n-1},X_i)\Big) \quad (4.19)$$

with

$$\vec{F}_{\mathrm{av}}(\vec{q}_i)=-\int\limits_{S_c}\nabla_{\vec{q}_i}V(\vec{q}_i-\vec{q}_j)f_2^\circ(X_j|X_i)dX_j \quad (4.20)$$

denoting the mean-field force exerted by the outer particles onto the i-th inner particle under the assumptions that

(1) pair interactions $V(\mathbf{q}_i-\mathbf{q}_j)$ are short-ranged so that pair interactions are relevant only close to the open system's boundary,

(2) the probability density of finding n particles in states $\left(\boldsymbol{X}^{n-1},X_i\right)\in S^n$ and one other outer particle in X_j, given by marginalization over $\boldsymbol{\Xi}_{n+1}^N$, can be factorized as

$$\binom{N}{n}\int\limits_{(S_c)^{N-n-1}} F_N(t,\boldsymbol{X}^{n-1,},X_i,X_j,\boldsymbol{\Xi}_{n+1}^N)d\boldsymbol{\Xi}_{n+1}^N \approx f_2^\circ(X_j|X_i)f_n\left(t,\boldsymbol{X}^{n-1},X_i\right). \quad (4.21)$$

(3) $f_2^\circ(X_{\mathrm{out}}|X_{\mathrm{in}})$ is a known or modelled conditional distribution for joint appearances of an outer particle given the state of an inner one.

Here we consider assumption (1) as a physical necessity for assumptions (2) and (3) to be justifiable in the first place, while the latter two encode the more general assumption that the statistics of the reservoir is independent of the instantaneous state of the open system for the present purposes.

Results of step II

(a) For all particles i in Ω, $i \in \{1,\dots,n\}$, it holds

$$\binom{N}{n} \int\limits_{(S_c)^{N-n}} \nabla_{\vec{q}_i} \cdot \left(\vec{v}_i F_N(t, \boldsymbol{X}^n, \boldsymbol{\Xi}_n^N)\right) d\boldsymbol{\Xi}_n^N = \nabla_{\vec{q}_i} \cdot \left(\vec{v}_i f_n\right). \tag{4.22}$$

(b) In the reservoir, $n+1 \leqslant i \leqslant N$, one of the integrals will be over $\Xi_i \in S_c$ which, after summing over the respective terms and utilizing the indistinguishability of the particles, leads to an integral over the boundary $\partial\Omega$ of the open system:

$$\begin{aligned}\binom{N}{n}(N-n) \int\limits_{S_c} \int\limits_{(S_c)^{N-n-1}} \nabla_{\vec{q}_i} \cdot \left(\vec{v}_i F_N(t, \boldsymbol{X}^n, (\vec{q}_i, \vec{p}_i), \boldsymbol{\Xi}_{n+1}^N\right) d\boldsymbol{\Xi}_{n+1}^N \, d\Xi_i \\ = -(n+1) \int\limits_{\partial\Omega} \int\limits_{\mathbb{R}^3} \left(\vec{v}_i \cdot \vec{n}\right) \widehat{f}_{n+1}(t, \boldsymbol{X}^n, (\vec{q}_i, \vec{p}_i)) \, d^3 p_i \, d\sigma_i \,, \end{aligned} \tag{4.23}$$

where we employed the identity $\binom{N}{n}(N-n) = \binom{N}{n+1}(n+1)$ and the notation assumes $i = n+1$.

Here, guided by the theory of characteristics, we distinguish the relevant forms of $\widehat{f}_{n+1}$ for outgoing and incoming particles as follows: Under the assumption of statistical independence of the reservoir particle states from those of the inner particles, we have

$$\widehat{f}_{n+1} = \begin{cases} f_{n+1} & \left(\vec{v}_i \cdot \vec{n} > 0\right), \\ f_n f_1^\circ & \left(\vec{v}_i \cdot \vec{n} < 0\right), \end{cases} \tag{4.24}$$

where f_1° is the single particle (equilibrium) density of the reservoir. Alternatively, assuming a grand canonical (GC) distribution for state space trajectories that enter the open system from outside one could write down as a plausible model:

$$\widehat{f}_{n+1} = \begin{cases} f_{n+1} & \left(\vec{v}_i \cdot \vec{n} > 0\right), \\ f_{n+1}^{\mathrm{GC}} & \left(\vec{v}_i \cdot \vec{n} < 0\right). \end{cases} \tag{4.25}$$

Note that we do not intend to promote the closure assumptions regarding the reservoir statistics introduced above (through the functions f_1° and f_2°) as being optimal or preferable over alternative formulations. Instead, these closures are meant to be placeholders that highlight the principal necessity of explicitly formulating assumptions on the reservoir behavior in the context of the present derivations.

Final equation

Combining the results of Steps I and II, one obtains a hierarchy of Liouville-type equations for f_n:

$$\frac{\partial f_n}{\partial t} + \{f_n, H_n\} = \Psi_n + \Phi_n^{n+1} \tag{4.26}$$

with boundary terms on the r.h.s. describing the action of the reservoir, namely the interaction term due to a mean-field forcing by the reservoir particles

$$\Psi_n[\boldsymbol{X}^n, f_n] = -\sum_{i=1}^{n} \nabla_{\vec{p}_i} \cdot \left(F_{\mathrm{av}}(\vec{q}_i) f_n(t, \boldsymbol{X}^{i-1}, X_i, \boldsymbol{X}_i^{n-i})\right), \tag{4.27}$$

and an exchange term due to particles entering and leaving the domain Ω:

$$\begin{aligned}\Phi_n^{n+1}[\boldsymbol{X}^n, f_n, f_{n+1}] = \\ (n+1) \int_{\partial\Omega} \int_{(\vec{p}_i \cdot \vec{n})>0} (\vec{v}_i \cdot \vec{n}) \left(f_{n+1}\left(t, \boldsymbol{X}^n, (\vec{q}_i, \vec{p}_i)\right) - f_n\left(t, \boldsymbol{X}^n\right) f_1^{\circ}\left(\vec{q}_i, -\vec{p}_i\right)\right) d^3 p_i \, d\sigma_i \,.\end{aligned} \tag{4.28}$$

4.2.8 Appendix B: the case of two distinct reservoirs at different thermodynamic conditions

Let us consider a prototype situation as that illustrated in fig. 4.10 where Ω is a region that separates the Universe in two distinct (large) reservoirs, (Res_1 and Res_2), and, as anticipated before, we assume that the two reservoirs are in stationary thermodynamic conditions in the time scale considered. Straightforward physical considerations lead to the conclusion that Ω has a spatially asymmetric exchange with the Universe and may thus possess a nonequilibrium stationary state. Formally one can proceed as for the case of a single reservoir and derive an equation for f_n in this situation. The total probability distribution function F_N describes the entire Universe including the thermodynamic states of Res_1 and Res_2. From F_N, by marginalizing w.r.t. $N-n$ degrees of freedom of particles in Ω_c, one obtains the distribution function f_n of the open system. Furthermore, the Liouville equation for F_N applies as before, and thus by marginalizing the Liouville equation for F_N w.r.t. the degrees of freedom of the particles in Ω_c one would obtain the corresponding Liouville-type equation for f_n ($n \in \{0, ..., N\}$) as for the case of one reservoir of Ref.[97]. This means an analytic derivation of the conditions of nonequilibrium induced by the concurrent action of the two reservoirs. In the sections below we will follow the marginalization procedure adopted in the previous section and adapted to the setup illustrated in fig. 4.10

4.2.8.1 Step I revised with Res_1 and Res_2

(a) Again, the boundary integral in eq. (4.17) will vanish in the limit of the radius of the ball tending to infinity because F_N will decay rapidly for large momenta, i.e., one can expect a decay as $\exp[-(\vec{p}_i)^2/2Mk_BT_1]$ in Res_1 and $\exp[-(\vec{p}_i)^2/2Mk_BT_2]$ for Res_2 (assuming they are both much larger than Ω). As said before, it is sufficient that F_N is a probability density and thus integrable.

(b) If both particles i, j of the pair are inside of Ω, nothing changes. In particular, the marginalization w.r.t. the particles outside [eq. (4.18)] implies that the whole information about the particles of the reservoirs is integrated out.

(c) Here emerges the first substantial difference. In the case that particle i is inside of Ω and particle j in one of the reservoirs, eq. (4.19) remains formally the same, but the calculation of the mean force changes [eq. (4.20)]. One needs to carefully consider the dependency of the pair's potential energy on the position of the particle in each of the two distinct reservoirs. The modified expression of $\vec{F}_{\text{av}}(\vec{q}_i)$ carries the fact that the boundary with Res_1 has different thermodynamic and statistical mechanics properties than the boundary with Res_2, depending on the specific subdomain of S_c over which the integration in the variable X_j is carried out. This implies that the assumed probability density of finding n particles in states $\left(\boldsymbol{X}^{n-1}, X_i\right) \in S^n$ and one other outer particle in X_j is now given by $f_n\left(\boldsymbol{X}^{n-1}, X_i\right) f_2^{\circ,R1}(X_j|X_i)$ if $X_j \in \text{Res}_1$ and by $f_n\left(\boldsymbol{X}^{n-1}, X_i\right) f_2^{\circ,R2}(X_j|X_i)$ if $X_j \in \text{Res}_2$. The integration of X_j over the whole $S_c = \text{Res}_1 \cup \text{Res}_2$ splits into the sum of two integrals over the domains Res_1 and Res_2, respectively:

$$\vec{F}_{\text{av}}(\vec{q}_i) = -\int\limits_{\text{Res}_1} \nabla_{\vec{q}_i} V(\vec{q}_i - \vec{q}_j) f_2^{\circ,R1}(X_j|X_i)\, dX_j - \int\limits_{\text{Res}_2} \nabla_{\vec{q}_i} V(\vec{q}_i - \vec{q}_j) f_2^{\circ,R2}(X_j|X_i)\, dX_j\,. \tag{4.29}$$

Specifically, the assumption that the statistics of both reservoirs are independent of each other yields the additive form $\vec{F}_{\text{av}}(\vec{q}_i) = \vec{F}_{\text{av}}^{R1}(\vec{q}_i) + \vec{F}_{\text{av}}^{R2}(\vec{q}_i)$.

4.2.8.2 Step II revised with Res_1 and Res_2

(1) Similarly as in step I, for the particles $i \in \{1, \ldots, n\}$ inside of the domain Ω the terms in eq. (4.22) remain the same because the marginalization w.r.t. the particles outside implies that any information about the reservoirs is integrated out.

(2) Otherwise, for $n+1 \leqslant i \leqslant N$, the effects of the two distinct reservoirs entering eq. (4.23) clearly emerges in the definition of $\widehat{f}$ [eq. (4.24)], because one needs to define $\widehat{f}$ differ-

ently on the two reservoirs. For $\Xi_i \in \mathrm{Res}_1$, one has $\widehat{f}^{R1}_{n+1} = f_n f_1^{\circ,R1}$ with $f_1^{\circ,R1}$ being the single particle (equilibrium) density in reservoir 1 and equivalently $\widehat{f}^{R2}_{n+1} = f_n f_1^{\circ,R2}$ for the other reservoir. Or, equivalently, $\widehat{f}^{R1}_{n+1} = f^{GC}_{R_1}$ (same for R_2,) if one makes the modeling choice of the grand canonical distribution for each reservoir.

Moreover, the decomposition of the boundary $\partial\Omega = \partial\Omega^1 \cup \partial\Omega^2$ implies the splitting of the surface integral:

$$-(n+1)\int\limits_{\partial\Omega}\int\limits_{\mathbb{R}^3} \left(\vec{v}_i\cdot\vec{n}\right)\, \widehat{f}_{n+1}(t,\boldsymbol{X}^n,(\vec{q}_i,\vec{p}_i)\, d^3p_i\, d\sigma_i = \sum_{r=1}^{2} I_{\partial\Omega^r} \tag{4.30}$$

where

$$I_{\partial\Omega^r} = -(n+1)\int\limits_{\partial\Omega^r}\int\limits_{\mathbb{R}^3} \left(\vec{v}_i\cdot\vec{n}\right)\, \widehat{f}_{n+1}(t,\boldsymbol{X}^n,(\vec{q}_i,\vec{p}_i)\, d^3p_i\, d\sigma_i\,. \tag{4.31}$$

In the case $\vec{v}_i\cdot\vec{n} < 0$, one has to replace $\widehat{f}^{n+1}$ with $f_n f_1^{\circ,R1}$ in the integral over $\partial\Omega^1$ and with $f_n f_1^{\circ,R2}$ in the integral over $\partial\Omega^2$.

After collecting the results of the previous steps, we straightforwardly obtain:

$$\frac{\partial f_n}{\partial t} + \{f_n, H_n\} = \sum_{r\in\{R1,R2\}} \left(\Psi_{n,r} + \Phi^{n+1}_{n,r}\right) \tag{4.32}$$

where the terms on the r.h.s. closely resemble those for a single reservoir and read, e.g., for $r = R1$:

$$\Psi_{n,R1}[\boldsymbol{X}^n, f_n] = -\sum_{i=1}^{n} \nabla_{\vec{p}_i}\cdot\left(F^{R1}_{\mathrm{av}}(\vec{q}_i) f_n(t,\boldsymbol{X}^{i-1},X_i,\boldsymbol{X}_i^{n-i})\right) \tag{4.33}$$

and

$$\Phi^{n+1}_{n,R1}[\boldsymbol{X}^n, f_n, f_{n+1}] = \\ (n+1)\int\limits_{\partial\Omega^1}\int\limits_{(\vec{p}_i\cdot\vec{n})>0} \left(\vec{v}_i\cdot\vec{n}\right)\, \left(f_{n+1}\left(t,\boldsymbol{X}^n,(\vec{q}_i,\vec{p}_i)\right) - f_n\left(t,\boldsymbol{X}^n\right) f_1^{\circ,R1}\left(\vec{q}_i,-\vec{p}_i\right)\right) d^3p_i\, d\sigma_i\,. \tag{4.34}$$

The setup of fig. 4.10 and the marginalization procedure can be straightforwardly extended to an arbitrary number of m disjoint reservoirs, interfaced with Ω:

$$\frac{\partial f_n}{\partial t} + \{f_n, H_n\} = \sum_{r=1}^{m} \left(\Psi_{n,r} + \Phi^{n+1}_{n,r}\right), \tag{4.35}$$

which describes a linear and additive action of independent reservoirs.

4.2.9 Appendix C: technical details of the simulations

The setup of both the AdResS and the full atomistic reference simulations was the same as described in detail in Ref.[22] and its supplementary material. The investigated LJ fluids consist of point particles of mass m that interact via the shifted and smoothly truncated pair potential $U(r) = [U_{\mathrm{LJ}}(r) - U_{\mathrm{LJ}}(r_c)]f((r-r_c)/h)$ for $r \leqslant r_c$, and $U(r) = 0$ otherwise, with $U_{\mathrm{LJ}} = 4\varepsilon\left[(r/\sigma)^{-12} - r/\sigma)^{-6}\right]$, the cutoff radius $r_c = 2.5\sigma$, the smoothing function $f(x) = x^4/(1+x^4)$, and $h = 0.005\sigma$. The parameters ε and σ are taken to define the units for energy and length, $\tau = \sqrt{m\sigma^2/\varepsilon}$ is the unit of time. Dimensionless quantities are defined as $\varrho^* = \varrho\sigma^3$ and $T^* = k_B T/\varepsilon$ for density and temperature, respectively. For particle pairs involving at least one tracer particle of AdResS, the interaction is switched off, $\varepsilon = 0$.

For the simulations reported in fig. 4.13, we used reservoir states in the liquid phase along the same isobar, i.e., they have the same pressure $P(T,\varrho) = \text{const}$. The hot reservoir serves as reference state point and is chosen at temperature $T^*_{\mathrm{hot}} = 0.95$ and density $\varrho^*_{\mathrm{hot}} = 0.622$, which results in a (reduced) pressure of $P^* := P\sigma^3/\varepsilon \approx 0.045$. The state points of the cold reservoir were determined such that they are at the same pressure as the hot reservoir. We used the following points in the temperature–density plane: $(T^*_2, \varrho^*_2) = (0.825, 0.72)$, $(T^*_3, \varrho^*_3) = (0.7, 0.791)$, and $(T^*_4, \varrho^*_4) = (0.625, 0.828)$, leading to temperature differences between the reservoirs of $\Delta T^* = 0.125$, 0.250, and 0.325, respectively.

For the isobaric results shown in fig. 4.14, state points along a slightly different isobar were used, namely $(T^*_{\mathrm{hot'}}, \varrho^*_{\mathrm{hot'}}) = (0.975, 0.5987)$ and $(T^*_{\mathrm{cold}}, \varrho^*_{\mathrm{cold}}) = (0.85, 0.7047)$, both at a pressure of $P^* = 0.051$. The data for the isochoric setup were obtained with reservoir states that represent the same, average density, $\bar{\varrho}^* = (\varrho^*_{\mathrm{hot'}} + \varrho^*_{\mathrm{cold}})/2 = 0.6517$, but different temperatures $T^*_{\mathrm{hot'}}$ and T^*_{cold} as before; the corresponding pressures differ widely: $p^*_{\mathrm{hot'}} = 0.194$ and $p^*_{\mathrm{cold}} = -0.140$. The negative pressure implies that in equilibrium such a reservoir would phase separate. This is not necessarily the case in the non-equilibrium situation. In our case it is found that the pressure gradient is balanced by a density gradient so that effectively the reservoir is no longer in the unstable state (but at a higher density, i.e., liquid again). So in essence, the example makes sense in the non-equilibrium case and it represents a challenging condition for testing our model. For all nonequilibrium simulations, a cuboid domain of size $120\sigma \times 20\sigma \times 20\sigma$ was used for the "Universe", with the long edge corresponding to the direction along which molecules change their resolution in AdResS. Periodic boundary conditions were applied at all faces of the cuboid, and a mirrored setup with in total two AT boxes, four Δ regions, and two TR regions was employed as in Ref. [22]. The Hamiltonian dynamics of the systems

was integrated with the velocity Verlet scheme for a timestep of 0.002τ. No further measures were applied to the AT regions; the Δ and TR regions in AdResS and the reservoir regions in the full atomistic reference simulation were thermalized with the Andersen thermostat [47] with the update rate set to $\nu_{\text{coupl}} = 50\tau^{-1}$ for fig. 4.13 and $20\tau^{-1}$ for fig. 4.14. The AdResS setups contained typically 16 000 LJ particles on average, whereas about 31 000 LJ particles were used for the reference simulations. At each state point, nonequilibrium trajectories over a duration of $15\,000\tau$ each were generated, the first quarter of which ($3\,750\tau$) was discarded for the calculation of stationary time averages. For the data analysis, the simulation box was divided at the mirror plane of the setup and the results were averaged over both halves. The averages are done over one long trajectory for the isobaric case and over three different trajectories for the isochoric case.

4.3 Conclusion

AdResS is a suitable framework for numerically simulating open systems of molecules embedded in a reservoir, similar to the Bergmann-Lebowitz model for open systems, which is a generalization of Liouville's equation. The desired domain is coupled to distinct reservoirs using a linear combination of thermodynamic forces and thermostats, while any nonlinearities are ignored. By exposing a LJ fluid with open boundaries to temperature gradients and enlarging the temperature gradient to determine the applicability range, the correctness of this approximation in linking separate reservoirs was confirmed. The results indicate a high level of agreement with the full resolution molecular simulation, indicating that this simplification is acceptable. We also discovered that, even if the reservoir conditions aren't fully set as in the full resolution case, the framework can still produce the correct result in the open system region. We can conclude from these studies that the setup can successfully mimic non-equilibrium situations (at least temperature gradients), that the range of validity is clear, and that the right protocol for performing these types of simulations is also verified. These findings pave the way for future applications in which a more realistic system is subjected to temperature gradients.

5 Mass Flux in AdResS

This chapter includes different attempts to create and maintain a steady mass current in an AdResS setup, as well as the challenges we have faced. The goal of providing these results is to give the reader an understanding of some possible approaches, the AdResS' response, and the potential reasons behind them. This may help to find a consistent simulation procedure to generate a steady mass flux in an AdResS setup in future studies.

5.1 Pressure gradient

The most common way of establishing mass flux in a physical system is to create a pressure gradient and then observe the system's response to it, which is a flow of particles from regions of higher pressure to the lower pressure.

This can be challenging in the AdResS, because the system has a strong desire to maintain a consistent pressure throughout the box and opposes any attempts to create a pressure difference. We tested this in section 4.2 by exposing the system to two reservoirs at different pressures and temperatures, but equal densities. The Andersen thermostat was used in the reservoir regions to control the heat, and thermodynamic forces were used to control the density. The system does not respond to this isochoric configuration as prescribed (see fig. 4.14) and adjusts the density in order to obtain equal pressure everywhere in the system. In other words, the reservoirs have densities that can considerably deviate from what was imposed, whereas in an isobaric simulation, the densities are exactly as specified. In this section, we try to keep the pressure difference in the system, first by changing the thermodynamic force and then by using the grand canonical Monte Carlo approach.

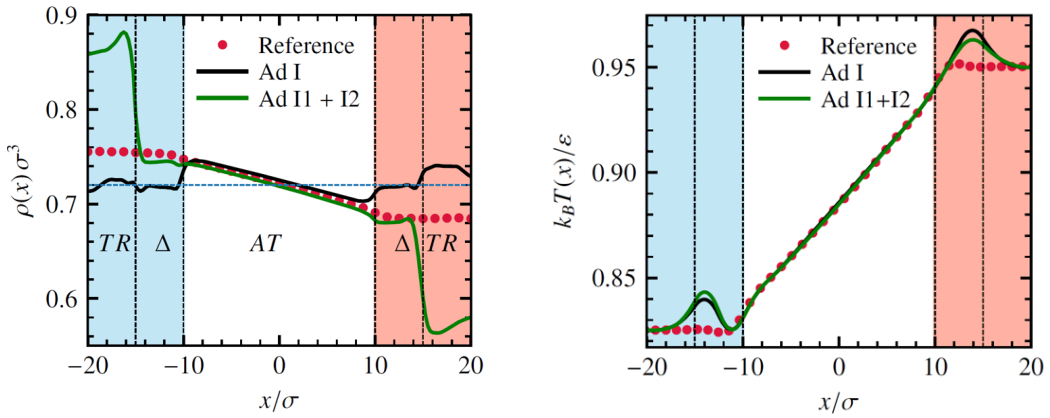

Figure 5.1: Densities (left) and temperatures (right) for a fluid with an average density of $0.72\sigma^{-3}$ exposed to two reservoirs in $T_h = 0.95\varepsilon/k_B$ and $T_c = 0.825\varepsilon/k_B$. The red dots represent the reference simulation data, the green curve represents the outcome of two thermodynamic forces computed independently and added up linearly, and the black curve represents one thermodynamic force calculated simultaneously using two different reservoir states.

Thermodynamic force

We have considered the linear summation of reservoir actions in non-equilibrium settings using the BL model [33, 34]. We changed this, and instead of calculating two different thermodynamic forces for the two different states separately and adding them afterwards, we calculated one thermodynamic force with two reservoirs acting on the system simultaneously, to account for possible nonlinear relations between the two reservoirs' actions and see if the resulting density gradient can be avoided this way. We observed that the density in the TR regions approaches the mean density (prescribed by the thermodynamic force), but the density gradient in the AT region remains unchanged as shown in figure 5.1. The pressure is still constant in the box and no mass current is created.

The regions where thermodynamic forces are applied are another factor that could make a difference. To keep the Hamiltonian dynamics, AdResS sets $\mathbf{F}_{\text{th}}(x)$ to zero in the AT region. We applied thermodynamic force everywhere in the box and found that this helped to decrease the density gradient in the AT region, but not totally eliminate it, as shown in fig. 5.2. So it is not possible to keep the pressure gradient.

Monte-Carlo particle movements

We combine the setup with a grand canonical Monte Carlo step to re-balance the reservoirs, adjust the densities, and keep the pressure difference in the system. The goal is to balance mass transport across the AT region by moving particles from one TR region to the other in a

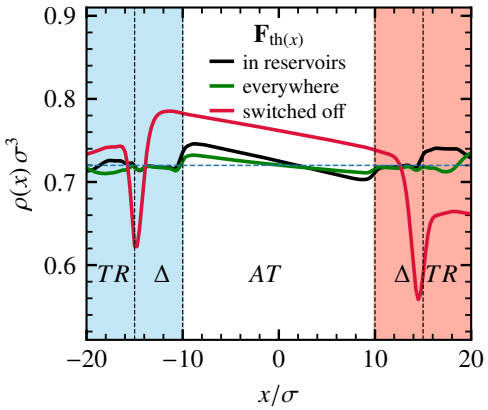

Figure 5.2: The role of applied thermodynamic force in different regions The presence of the thermodynamic force is unavoidable as the density shows non-physical deviations without it (red curve) according to the difference in the number of degrees of freedom. The black curve depicts the case in which Hamiltonian dynamics are maintained in the AT region and no thermodynamic force is applied there, but it is applied as usual in the TR and Δ regions. The thermodynamic force was also applied to the AT area, resulting in the green curve.

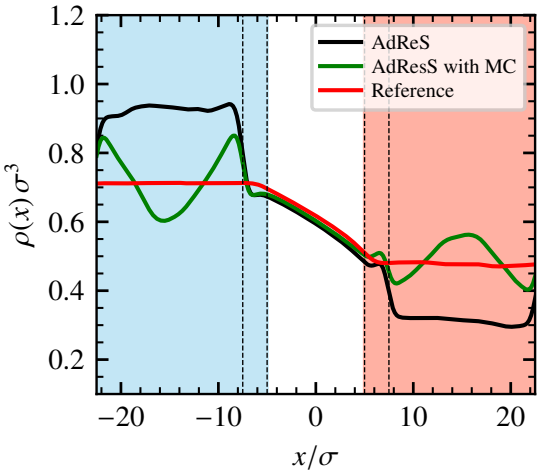

Figure 5.3: Non-equilibrium density profiles in three different simulations. Reservoirs have different temperatures, but the same density. The AdResS resists this pressure difference by creating a density difference. MC moves are used to counteract and prevent the creation of density difference.

systematic manner. The equations and details of the grand canonical Monte Carlo approach are explained in section 3.7.

We calculate two $\mathbf{F}_{\text{th}}(x)$s, both in the same density ($\rho = 0.6\sigma^{-3}$), but at different temperatures ($T = 1\varepsilon/k_B$, $T = 1.5\varepsilon/k_B$) set with Andersen thermostat, and combined them to run the non-equilibrium, isochoric simulation, which leads to density deviations. In the same setup and with the same thermodynamic forces, using MC, we check if we can prevent the system from equalizing the pressure by manipulating the densities.

In the x direction, the TR regions are 15σ wide. Stripes of size 4σ are considered in the center of the TR regions, and the particles to be swapped are chosen from these stripes. The prescribed pressure value is used to calculate the expected mean number of particles (reduced fugacities) in the two TR regions. During the MD integration, after each 10 MD steps, a MC step is applied, and a random number of particles between 1 and 100 are swapped between the stripes.

The results of the reference simulation, the isochoric simulation without the MC step, and the identical simulation with MC swaps are presented in fig. 5.3. In the TR regions, the number of particles, $\overline{N}$, reached the reference result, and the stationary density profile has a peak on one side and a valley on the other. The application of the MC in the TR regions had no effect on the density profile in the AT region, and no flux was observed.

5.2 Constant external force

Applying a constant external force such as gravity, all over the simulation box should result in a stationary mass current across the periodic setup. The role of thermostat type when dealing with mass currents is important, so we tested external forces in an AdResS configuration with a number of thermostats, and the results are presented below.

Andersen thermostat

In our first attempt, we used LJ fluid with $T = 2\varepsilon/k_B$ and $\rho = 0.46\sigma^{-3}$, as well as an Andersen thermostat acting on the reservoirs (Δ and TR regions). A constant external force was applied globally in addition to the thermodynamic force. We observed that as the external force is increased, the AT region is increasingly depleted (fig. 5.4), and only a transient mass flux occurs.

We also used the Andersen thermostat everywhere throughout the box. The AT region was

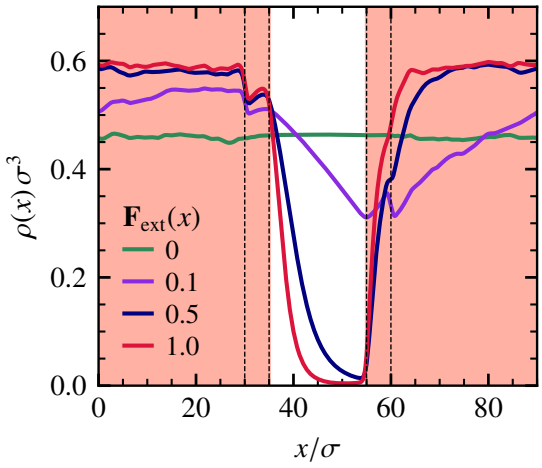

Figure 5.4: Density profile in a ($T = 2\varepsilon/k_B, \varrho = 0.46\sigma^{-3}$) system with an Andersen thermostat in the Δ and TR regions (colored regions). Constant external force is applied along the box in x direction.

no longer depleted; instead, a constant density profile along the box was created, and no stationary current was observed.

The fact that the regions where the thermostat is acting can change the response suggests that the type of the thermostat can have an impact as well. Replacing the Andersen thermostat with a momentum conserving thermostat can change the response of the system, and we have investigated this in the following.

Momentum conserving thermostats

The same configuration as before is employed, but instead of an Andersen thermostat, a velocity conserving Maxwell-Boltzmann thermostat (section 3.4.3) and a Lowe-Andersen thermostat (section 3.4.4) were used.

We observed that the system is unstable with these momentum conserving thermostats acting on Δ and TR regions. Even without applying an external force, a growing current was observed, and the temperature in the system increased without bounds.

Conclusion

We found that in order to maintain the current in the system, a momentum conserving thermostat is required. A momentum conserving thermostat, however, might cause instability in the AdResS transition region. This is due to the possibility that tracers may end up in an undesired place close to other particles when they enter the Δ region, resulting in an atypical

configuration with high energy. The thermostat in the Δ region is in charge of extracting this excess energy, but now that we use a momentum conserving thermostat, this excess energy may remain in the system, causing instability in long runs. In chapter 7, we propose a setup in which the system is stable and no energy blow-up occurs even in long simulations.

5.3 Custom flow

In this section, we describe another approach that aims to generate a prescribed non-equilibrium state by applying an appropriate external force. The so-called custom flow method introduced in ref. [49], can numerically construct the external force field required to get the desired non-equilibrium state in the system as defined by its mass current and density profiles. This force is calculated iteratively with the fields ϱ and $\mathbf{J}$ being the target density and mass currents, and $\dot{\mathbf{J}}$ being the partial time derivative of $\mathbf{J}$,

$$\mathbf{F}_{ext}^{(k+1)}(\mathbf{r},t) = \mathbf{F}_{ext}^{(k)}(\mathbf{r},t) + \alpha\left(\mathbf{J}(\mathbf{r},t) - \mathbf{J}^{(k)}(\mathbf{r},t)\right) + \beta\left(\dot{\mathbf{J}}(\mathbf{r},t) - \dot{\mathbf{J}}^{(k)}(\mathbf{r},t)\right) + \gamma\nabla\ln\frac{\varrho(\mathbf{r},t)}{\varrho^{(k)}(\mathbf{r},t)}. \quad (5.1)$$

Here, k denotes the iteration index, and α, β, and γ are free non-negative prefactors that can depend on time and position. The third term in eq. (5.1) is similar to what we used in the calculation of the $\varphi_{th}(x)$ eq. (2.12) in the AdResS scheme. The mass current and its time derivative will be set by the other two terms. ϱ, $\mathbf{J}$ and $\dot{\mathbf{J}}$ are corrected as the iterations progress, reducing their difference from the respective target values, and this procedure is repeated until a convergence within the specified tolerance is obtained.

The strength of corrections are determined with the prefactors. A possible choice for these prefactors are

$$\alpha(\mathbf{r},t) = \frac{m}{\varrho(\mathbf{r},t)\Delta t}, \qquad \beta(\mathbf{r},t) = \frac{m}{\varrho(\mathbf{r},t)}, \qquad \gamma = k_B T. \quad (5.2)$$

To check the approach, we test it for a LJ fluid in a closed system with $\varrho = 0.46\sigma^{-3}$ and $T = 2\varepsilon/k_B$ and without AdResS to impose the same density 0.46 and the same mass current $J = 0.2$ throughout the box. In some areas of the box, a Maxwell-Boltzmann velocity conserving thermostat (section 3.4.3) is used to fix the temperature. The outcomes are very good, the L^2 error in density is 0.3%, while the L^2 error of the current $J(x)$ is 0.8%.

To apply the custom flow method in AdResS, we try to calculate the proper external force for getting $J = 0.2$ in the same system as before. We applied Maxwell-Boltzmann velocity conserving thermostat in the reservoirs and observed that the velocity conserving thermostat

cannot be used in AdResS easily as the energy increases without bounds and the simulation becomes unstable.

5.4 Conclusion and suggestions

During various trials in creating a steady mass flux across the open system and observing the response, we discovered that a momentum conserving thermostat is required to maintain such a flux in the system. AdResS is very sensitive to this choice as it may lead to simulation instability and an energy blow up. The reason is that the excess heat in the transition region caused by the change of resolution cannot be removed efficiently using this type of thermostat. Coupling the AdResS to a momentum conserving thermostat has been done before, but with the original version of AdResS (without tracers and the abrupt change of particle type) [110–113].

Using a pump described in section 3.4.3, we could create a steady mass flux and saw no instabilities and will show the setup and results in chapter 7.

6 Blocking of liquid flow through nanoporous bead packings

The material in this chapter is the basis of a manuscript draft to be submitted for publication in a peer-reviewed journal: R. Ebrahimi Viand and F. Höfling: "Blocking of liquid flow through nanoporous bead packings".

We employ non-equilibrium molecular dynamics simulations to study the stationary flow of dense liquids through a model nanoporous medium, which is composed of obstacles arranged on an fcc lattice. The typical way to produce particle flow is to create a pressure gradient in the system and the particle flow appears as a response. We employ a different approach and use a "pump" to create a stationary flow of particles through the box, passing through the porous medium and observe the pressure drop as the response. The aim is to check to what extent the linear response regime (Darcy's law) is valid and when it breaks down. The dependence of the medium's permeability on its porosity is also of interest.

6.1 Model and simulation method

6.1.1 Model

The MD simulations and the data analysis were performed with the massively parallel software *HAL's MD package* [20, 114]. The setup consists of a slab of porous medium of width L, which is placed in the centre of the cuboid simulation domain, and the remaining space is filled initially with a dense Lennard-Jones (LJ) fluid (see fig. 7.1). We refer to the regions to the left and to the right of the medium as the *inlet* and the *outlet*, respectively. The porous medium is modelled as an array of obstacles located on a face-centered cubic lattice with lattice constant a_{lat}; the obstacles are soft, repulsive spheres of radius σ_o (see section 6.4 for details). For the fluid particles, we employ a smoothly truncated LJ pair potential; the corresponding LJ parameters

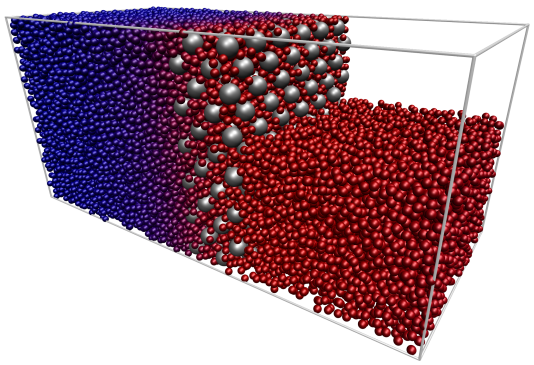

Figure 6.1: Snapshot of the simulation of liquid flow (from left to right) through a nanoporous medium. The medium is realised as a bead packing of obstacles (grey spheres) placed on an fcc lattice; here, it has a width of $n_x = 2$ unit cells. The temperature of the fluid particles increases from left to right (color code from blue to red). For clarity of the representation, the particles in the upper parts of the outlet region are not shown and the far ends of the simulation box have been omitted.

ε and σ serve as units of energy and length, respectively, and $\tau := (m\sigma^2/\varepsilon)^{1/2}$ defines the unit of time; m is the particle mass (section 6.4). Periodic boundary conditions are applied at all faces of the simulation domain, which has a length of $L_x = 100\sigma$ in the direction of flow and a quadratic cross section of area $A = (30\sigma)^2$. At the left boundary of the inlet, a region of width $L_{\text{th}} = 10\sigma$ is coupled to a stochastic thermostat which, in addition to the temperature control, acts as a "pump" by imposing a mean velocity on the particles and thereby creates and maintains a steady mass flux. Outside of this region, particle positions and momenta follow the unperturbed Hamiltonian dynamics. In response to the driving, a pressure difference ΔP develops between the inlet and outlet regions, which is a central observable of our study. The values for the temperature and number density of the fluid at the far end of the inlet were fixed at $T^* := k_{\text{B}}T/\varepsilon = 1$ and $\varrho_{\text{eq}} = 0.805\sigma^{-3}$ in the absence of driving, placing the LJ fluid in the liquid state.

The porous medium is composed of $N_o = 4n_x n_y n_z$ obstacles arranged on an fcc lattice with n_α unit cells along each Cartesian axis such that $n_y = L_y/a_{\text{lat}} = n_z$ are integer. The porosity of the medium is the fraction of free and total volumes, and here we use the nominal porosity $\varphi = (AL - N_o v_o)/AL$, where $v_o = (4\pi/3)\sigma_o^3$ is the excluded volume due to a single obstacle [I] and $L = (n_x - 1/2)a_{\text{lat}} + 2\sigma_o$ is the width of the medium. The porosity decreases by either decreasing the lattice constant a_{lat} or increasing the size σ_o of the obstacles; below we will choose $a_{\text{lat}} = 3\sigma$ and 5σ.

[I] With this definition, the values quoted for the porosity refer to the pore volume that is accessible to an ideal gas of point particles.

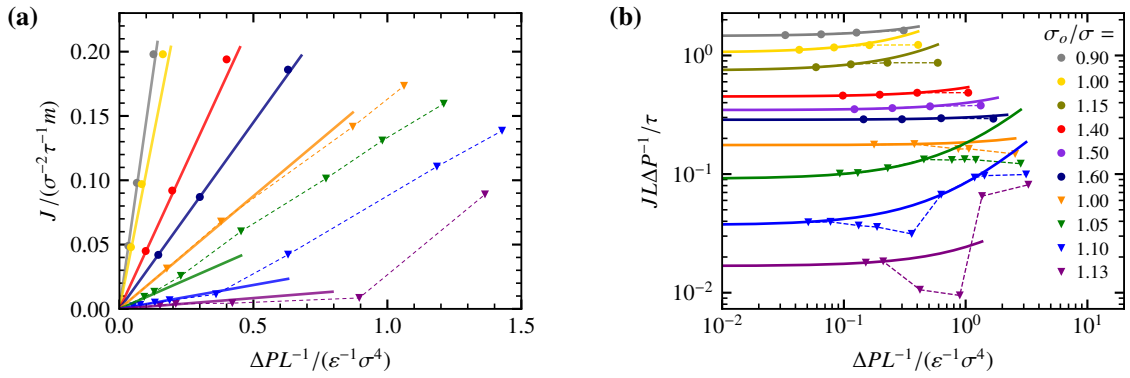

Figure 6.2: Simulation results (symbols) for the flow–pressure relations of regular bead packings. For each prescribed mass flux J, the pressure drop ΔP between inlet and outlet was observed and normalized by the width L of the porous medium. The medium was made of obstacles arranged on fcc lattices with either $n_x = 2$ and $a_{\mathrm{lat}} = 5\sigma$ (discs) or $n_x = 6$ and $a_{\mathrm{lat}} = 3\sigma$ (triangles); colors refer to different obstacle sizes σ_o as given in the legend of panel (b). For clarity, the data for some values of σ_o have been omitted in panel (a). Panel (a): solid lines test Darcy's law, $J = (k/\nu)\Delta P/L$, using the values of k/ν obtained from panel (b). Panel (b): the non-linear response is highlighted by showing $J/(\Delta P/L)$ vs. $\Delta P/L$ on double-logarithmic scales. Solid lines are fits to the asymptotic behaviour as $\Delta P/L \to 0$ using eq. (6.2), which includes the leading correction to Darcy's law; the intercepts at the left border yield k/ν, where k is the linear permeability. In both panels, dashed lines merely connect data points and serve as guide to the eye.

6.2 Results

6.2.1 Flow–pressure relation beyond Darcy's law

Fluid transport through a porous medium is characterized by the relationship between a steady mass flux J and the corresponding pressure drop ΔP applied across the medium. For small ΔP, the relation becomes linear and is known as Darcy's law [115]:

$$J = \frac{k\,\Delta P}{\nu L}, \tag{6.1}$$

where L is the width of the porous medium and k its permeability. The law is often stated for the volumetric flux in the case of incompressible liquids; the above form is obtained by multiplying with the mass density ϱ and then the kinematic viscosity $\nu = \eta/\varrho$ appears instead of the shear viscosity η. We use the mass flux J here as it is constant across the whole setup by mass conservation.

For a range of porous media, realized as bead packings, we have monitored the pressure drop ΔP that builds up when a certain mass flux J is imposed on the LJ liquid, using values for $J\sigma^2\tau/m$ between 0.002 and 0.2 (fig. 6.2a). With this choice, the Reynolds number $\mathrm{Re} = a_{\mathrm{lat}}J/\eta$ does not exceed values of $O(1)$.

Considering two different lattice constants and varying the obstacle size σ_o, we observe an approximately linear dependence, eq. (6.1), and thus Darcy flow in case of the larger lattice constant ($a_{\mathrm{lat}} = 5\sigma$) for all obstacle sizes studied ($\sigma_o \leqslant 1.6\sigma$). For the denser lattice ($a_{\mathrm{lat}} = 3\sigma$), however, we find a pronounced non-linear behavior for $\sigma_o \geqslant 1.05\sigma$, corresponding to porosities of $\varphi \leqslant 40\%$: the J–ΔP relation displays an affine increase, giving rise to an *apparent* permeability. However, this behavior sets in only after some threshold value of $\Delta P/L$ has been exceeded (the corresponding straight lines do not intersect the axis origin); for pressure gradients below this threshold, the flux increases only marginally as $\Delta P/L$ is increased.

In a less heuristic approach, we follow linear response theory, which suggests to amend Darcy's law by non-linear corrections. Including the leading term, [II]

$$J(F \to 0) \simeq \frac{k}{\nu} F(1 + cF), \quad F = \Delta P/L, \tag{6.2}$$

allowed us to fit the asymptotic behavior to the data as $\Delta P/L \to 0$ and to extract the actual linear permeability $k := \nu \lim_{F\to 0} dJ/dF$ (fig. 6.2b). For each obstacle size, only the two or three data points for the smallest $\Delta P/L$ were used for fitting. For $\sigma_o = 1.1\sigma$, the two points with $\Delta P/L$ between $0.7\varepsilon\sigma^{-4}$ and $3\varepsilon\sigma^{-4}$ were considered instead, and it is seen that the data for the smallest $\Delta P/L$ fall on the same curve. In the representation of fig. 6.2b, the apparent permeability is visible as a plateau at large pressure gradients, whereas the mentioned threshold behavior leads to a decrease of the *effective* or *local* permeability, $JL/\Delta P$. These trends combine into a non-monotonic behavior of $JL/\Delta P$ for the two lowest porosities studied, and the data suggest that the position of the minimum effective permeability shifts to larger pressure gradients as the obstacle size is increased. The further discussion of the rich J–ΔP relationship as it emerges for very strong driving and low porosities would exceed the present scope.

6.2.2 Linear permeability and critical porosity

For the range of bead packings studied, we observe a variation of the linear permeability k over two orders of magnitude (fig. 6.2b) and a monotonic decrease as a function of the porosity (fig. 6.3). The dependence of the permeability has some analogies with the diffusion problem in the Lorentz gas, i.e., the equilibrium motion of tracer particles in an obstacle array [117–121], which motivates the following arguments. At high porosity, one expects that the resistance of the medium to the flow is proportional to the obstacle density [117, 120, 122],

[II] Note that such analytic behaviour in the driving force, here ΔP, may break down at a critical point [116].

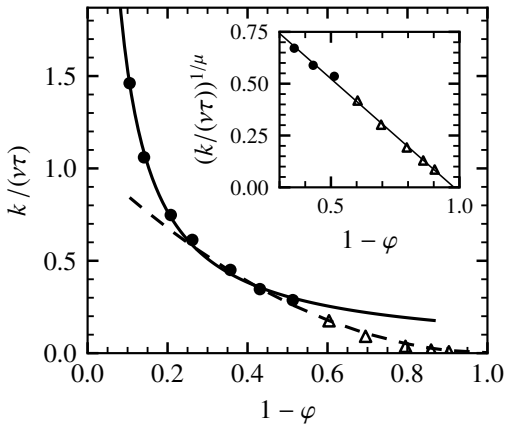

Figure 6.3: Dependence of the linear permeability on the porosity of the bead packings. Triangle and disc symbols refer to different lattice constants of the obstacle array: $a_{\mathrm{lat}} = 3\sigma$ and 5σ, respectively (see fig. 6.2). The high-porosity behavior, $k \sim 1/(1-\varphi)$, is indicated by the solid line, which was fitted to only those two data points where $\varphi > 0.85$. The dashed line shows Archie's law, i.e., the critical scaling at low porosity, $k \sim |\varphi - \varphi_c|^{\mu}$, anticipating $\mu = 2$ for the exponent. The latter dependence is rectified in the inset, and the linear extrapolation of the data points (solid line) yields the critical porosity $\varphi_c = (2.3 \pm 0.7)\%$.

equivalently, to the excluded volume fraction $1-\varphi$, and taking the reciprocal, one has

$$k \sim (1-\varphi)^{-1}, \quad \varphi \uparrow 1, \tag{6.3}$$

as for the diffusion constant, $D \sim (1-\varphi)^{-1}$. This relation describes the permeability data in fig. 6.3 very well for $\varphi \geqslant 50\%$, whereas at lower porosities, a stronger suppression of the permeability is observed, in line with the behavior of the diffusivity [119].

By geometrical considerations for the fcc lattice, the investigated porous medium can be decomposed into tetrahedral and octahedral pores with the corners given by the obstacle positions. The pores are connected by equilateral triangular ports of edge length $a_{\mathrm{lat}}/\sqrt{2}$, which suggests that the flow is blocked when the obstacle size exceeds a critical value where the ports close, e.g., $\sigma_{o,c} = a_{\mathrm{lat}}/\sqrt{6}$ in the case of hard-core exclusions. Indeed, our simulation results suggest that the linear permeability vanishes rapidly as a certain porosity φ_c is approached. Due to the soft repulsion between fluid particles and obstacles, fluid flow is still possible at lower porosities for sufficiently large pressure gradients, however, such a flow is beyond the linear response regime. Phenomenologically, the suppression of fluid flow near the percolation transition of a random medium is known as Archie's law [123, 124]:

$$k \sim |\varphi - \varphi_c|^{\mu}, \quad \varphi \downarrow \varphi_c, \tag{6.4}$$

introducing some exponent μ. Such a power-law suppression is well established for the

diffusivity, $D \sim |\varphi - \varphi_c|^{\mu'}$, and [125] proposed the general proportionality $k \propto D$, arguing that fluid flow and diffusion cease concomitantly near the percolation threshold. Although it is not clear *a priori* that different transport mechanisms share the same exponent [121], we anticipate that $\mu' = \mu$ for regular bead packings. Concerning the value of the diffusivity exponent, insight is gained from the mapping to random resistor networks, which yields $\mu' = (d-2)\bar{\nu} + \zeta$, [126, 127] where d is the dimension of space and the exponents $\bar{\nu}$ and ζ govern the critical divergence of the correlation length and the chain resistance, respectively. For periodic porous media, as investigated here, the correlation length does not diverge, and we put $\bar{\nu} = 0$. As a peculiarity of continuum percolation, the transition rate W between adjacent pores has a singular distribution due to narrow gaps, $p(W \to 0) \sim W^{-\alpha}$ with exponent $\alpha = (d-2)/(d-1)$ [128]. In $d \geqslant 3$ dimensions, this singularity determines the exponent of the chain resistance, $\zeta = (1-\alpha)^{-1}$ [129, 130]. In conclusion, we find $\mu = d - 1$ and thus $\mu = 2$ for $d = 3$. Indeed, rectification of the permeability data using this value of μ yields a straight line (see inset of fig. 6.3). The axis intercept renders the critical porosity as $\varphi_c = (2.3 \pm 0.7)\%$, and such a small value was expected [131, 132].

6.2.3 Non-isothermal flow

Aiming at insight into the non-equilibrium aspects of the permeability problem, we have computed the spatially resolved profiles of central thermodynamic observables, namely pressure $P(x)$, temperature $T(x)$, and mass density $\varrho(x)$, where the x-axis points along the direction of the flow (fig. 6.4). The resistance of the porous medium to the imposed fluid flow leads to a pronounced increase of the pressure in front of the medium. In agreement with mechanical equilibrium, the pressure is constant in both the inlet and outlet regions, so that the pressure drop across the medium is unambiguously defined, $\Delta P = P_{\text{in}} - P_{\text{out}}$. In a more refined argument, $\partial_x P = 0$, follows from local momentum conservation for small Mach number [eq. (6.6)] (section 6.4); the thermostatted region and the porous medium act as sources and sinks for the momentum density, respectively, which explains the linear variation of $P(x)$ in these regions. The outlet pressure equals to the equilibrium baseline pressure P_{eq} that is attained by the resting fluid ($J = 0$) at the same temperature and (mean) density. The slight difference observed in the data (fig. 6.4a) can be diminished by increasing the width of the thermostatted region; it does not affect the value of ΔP.

For the temperature, the situation is markedly different: as we will justify below, $T(x)$ increases exponentially fast in the inlet as the porous medium is approached and it increases further linearly inside of the medium. The maximum temperature is reached at the interface of the medium and the outlet; its value is the larger the larger the pressure drop ΔP. Due to the

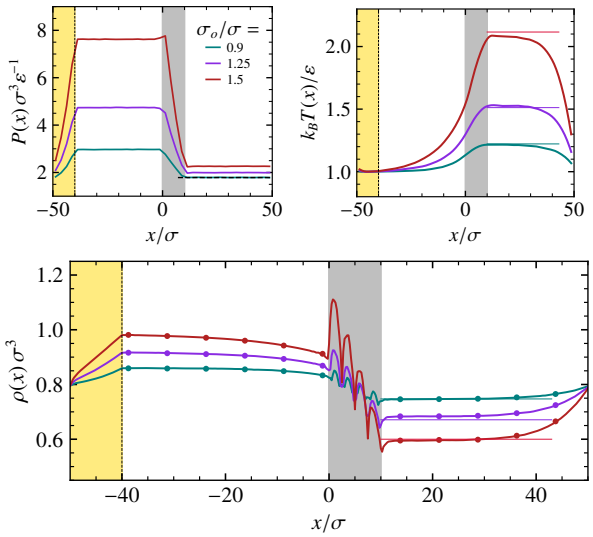

Figure 6.4: Simulation results for the spatially resolved thermodynamic observables pressure $P(x)$, temperature $T(x)$, and mass density $\varrho(x)$ obtained along the flow of a LJ liquid through a porous medium (grey region). The parameters of the obstacle lattice are $n_x = 2$ and $a_{\mathrm{lat}} = 5\sigma$ and the line colors refer to different obstacle sizes. A mass flux of $J = 0.2m\sigma^{-2}\tau^{-1}$ was imposed on the far end of the inlet using a pump-like thermostat (yellow region). The value of the equilibrium pressure (for $J = 0$) is marked in the outlet region by the black dashed line in the upper left panel. Solid horizontal lines indicate the plateaus of $T(x)$ and $\varrho(x)$ in the outlet that emerge for macorscopically large outlet regions. In the lower panel, symbols show the density that is predicted by the thermal equation of state, anticipating local equilibrium. In the calculation of the density profile $\varrho(x)$ within the porous medium, the excluded volume of the obstacles was partially accounted for (see main text).

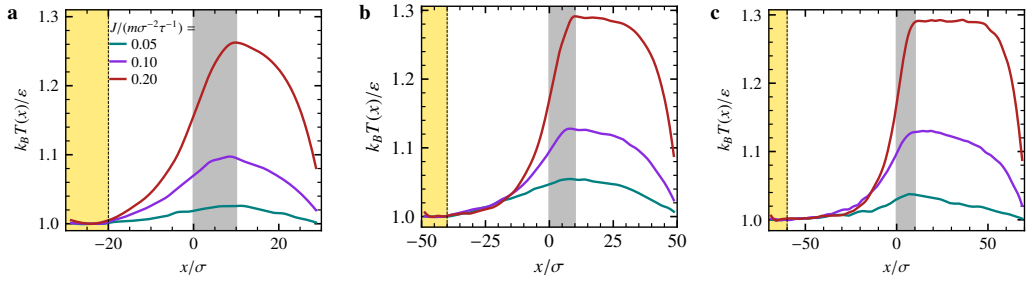

Figure 6.5: Temperature profiles for increasing sizes of the inlet and outlet regions (from left to right); line colors refer to different mass fluxes J. The total length of the simulation box L_x along the direction of flow is (a) 60σ, (b) 100σ, and (c) 140σ, whereas the widths of the porous medium (gray region, $L = 9.5\sigma$ for $n_x = 2$, $a_{\mathrm{lat}} = 5\sigma$, and $\sigma_o = \sigma$) and of the thermostated region (yellow region, $L_{\mathrm{th}} = 10\sigma$) are kept fixed.

periodic boundary conditions of the simulation box, $T(x)$ decreases again in the outlet region to match the thermostat temperature at the right boundary, $T(L_x/2) = T_{\text{in}}$. For macroscopically large inlet and outlet regions, $T(x)$ converges to a plateau T_{out} in the outlet (fig. 6.5); these outlet temperatures can reach high values, even several multiples of the inlet temperature (see also fig. 6.6).

Due to thermal expansion along the direction of the flow at constant pressure, the fluid density decreases in the inlet and also inside of the porous medium, reaching a low plateau value $\varrho_{\text{out}} < \varrho_{\text{eq}}$ in the outlet. The density variation along the flow is non-trivial; generally, it is larger for larger mass fluxes due to a higher inlet pressure and a larger temperature increase. When calculating $\varrho(x)$ inside of the porous medium, we have corrected for the excluded volume of the obstacle lattice, based on the density profile in equilibrium (see section 6.4). However, it appears that, for the strongly driven liquid, more fluid particles can be squeezed between the obstacles, leading to the spurious, residual oscillations of the density seen in fig. 6.4c. a complete correction would be flux-dependent. The density profile in the inlet and outlet regions neatly follows the predictions from the thermal equation of state, $P = P(\varrho, T)$ [133], using the simulation data for $P(x)$ and $T(x)$ as input and numerically inverting $P(x) = P(\varrho(x), T(x))$. We conclude that the flowing liquid is locally in thermal equilibrium, also for the largest mass flux considered here.

6.2.4 Non-equilibrium thermodynamics

The last observation allows us to rationalize the observed temperature profile in terms of conservation laws combined with thermodynamic properties of the liquid. In particular, we will focus on the exponential increase of $T(x)$ in the inlet region. Such an behavior of the temperature is known, e.g., for the compressible gas flow of a premixed laminar flame [134], which we extend here to the case of liquids.

By symmetry, vectorial quantities such as the flow velocity $\vec{u} = u\hat{e}_x$ point along the direction of the flow (which is chosen as the x-axis) and the problem reduces to an effectively one-dimensional one. Conservation of mass implies the continuity equation

$$\partial_t \varrho + \partial_x(\varrho u) = 0, \tag{6.5}$$

and thus a constant mass flux, $J(x) = \varrho u = const$, in a stationary situation. It yields a simple relation between the derivatives of density and velocity, $u\partial_x\varrho = -\varrho\partial_x u$.

The product ϱu is also interpreted as momentum density, and momentum conservation yields

the balance equation [135, 136]

$$\partial_t(\varrho u) + \partial_x(\varrho u^2 + P + \tau) = 0, \tag{6.6}$$

where τ is the only non-zero component of the deviatoric stress tensor for parallel flow; for a Newtonian fluid, it holds $\tau = -\eta\partial_x u$. We note that on the right hand side, appropriate sink or source terms have to be included in the thermostatted region and inside of the porous medium.

For an asymptotic dimensional analysis of the problem, we estimate the magnitudes of pressure and density by their equilibrium values, $\varrho_0 = \varrho_{\mathrm{eq}}$ and pressure $P_0 = P_{\mathrm{out}}$. We use a_{lat} as a typical length, which defines the Reynolds number $\mathrm{Re} = a_{\mathrm{lat}} J/\eta$, and introduce the Mach number $\mathrm{Ma} = u_0/c_s$, using $u_0 := J/\varrho_0$ and $c_s \approx (P_0/\varrho_0)^{1/2}$ as an approximation to the speed of sound. With this, eq. (6.6) can be written for stationary flow in terms of dimensionless fractions as

$$\partial_x \left(\frac{\varrho u^2}{\varrho_0 u_0^2} + \frac{1}{\mathrm{Ma}^2}\frac{P}{P_0} - \frac{1}{\mathrm{Re}}\frac{\partial_x u}{u_0/a_{\mathrm{lat}}} \right) = 0. \tag{6.7}$$

For the present simulations of a LJ liquid, one estimates that $\mathrm{Ma} \lesssim 0.2$ and $\mathrm{Re} \lesssim 2$ (see table 6.1), so that the second term is the dominant one. One concludes in agreement with our observations that $\partial_x P = 0$, the fluid is in mechanical equilibrium in the inlet and outlet regions.

The isobaric conditions along the flow suggest to use the specific enthalpy, $h(x) = e(x) + P(x)/\varrho(x)$, for the discussion of the balance of energy fluxes; here, $e(x)$ is the internal energy per unit mass of the quiescent fluid, which needs to be amended by the kinetic energy $u(x)^2/2$ of the flowing liquid. Local conservation of energy implies a continuity equation for $e(x)$, which in the stationary case reads [136]

$$\partial_x \left[\varrho u \left(h + \tfrac{1}{2}u^2 \right) + J_T + \tau u \right] = 0\,. \tag{6.8}$$

For the heat flux $J_T(x)$, we assume that Fourier's law holds,

$$J_T = -\kappa \partial_x T, \tag{6.9}$$

with the heat conductivity κ. We have verified eq. (6.8) numerically, showing that $\varrho u \left(h + \frac{1}{2}u^2 \right) + J_T \approx const$ along the flow, also across the porous medium (fig. 6.9); in particular, the viscous contribution τu is either constant or negligible. For the calculation of $J_T(x)$, see section 6.4.

In the next step, local thermal equilibrium allows us to express the enthalpy through the

variables P and T by means of the caloric equation of state, $h = h(P,T)$. For isobaric flow, the enthalpy gradient obeys

$$\partial_x h = c_P\,\partial_x T \qquad (\partial_x P = 0)\,, \tag{6.10}$$

where $c_P = (\partial h/\partial T)_P$ is the isobaric specific heat.

The kinetic term $Ju^2/2$ favourably combines with the flux of viscous stresses as follows. From eq. (6.6), it follows that $J\partial_x u = -\partial_x(P+\tau)$ and thus with $\partial_x P = 0$,

$$\partial_x\left(\tfrac{1}{2}Ju^2 + \tau u\right) = \tau\partial_x u\,. \tag{6.11}$$

Collecting terms, we obtain

$$Jc_P\partial_x T = \partial_x(\kappa\partial_x T) - \tau\partial_x u\,, \tag{6.12}$$

which, for a Newtonian fluid, reduces to

$$Jc_P\partial_x T = \kappa\partial_x^2 T + \eta(\partial_x u)^2. \tag{6.13}$$

Here, we have also assumed that $\partial_x\kappa = 0$, which we have verified numerically by plotting $-J_T(x)/\partial_x T(x)$ using eq. (6.9). Considering the thermal equation of state $P = P(\varrho,T)$, and the mechanical equilibrium, gradients of temperature and density are related as $(1/\varrho)\partial_x\varrho = -\alpha\partial_x T$, where α is the thermal expansion coefficient and is verified to be constant in inlet and outlet regions. This relation and the mass conservation eq. (6.5) in a constant J help to express the velocity gradient as a temperature gradient,

$$\partial_x u = -(u/\varrho)\partial_x\varrho = (\alpha J/\varrho)\partial_x T\,, \tag{6.14}$$

which leads to

$$c_P\,\partial_x T = \frac{\kappa}{J}\,\partial_x^2 T + \frac{\eta\alpha^2 J}{\varrho^2}\,(\partial_x T)^2. \tag{6.15}$$

The second term in r.h.s is negligible according to table 6.1 and the solution to remaining differential equation, under the boundary conditions $T(x\to-\infty) = T_{\text{in}}$ and $T(x_0) = T_{\text{in}} + \Delta T$ is

$$T(x) = T_{\text{in}} + \Delta T\,\mathrm{e}^{(x-x_0)/\ell}\,, \quad \ell = \frac{\kappa}{c_P J}\,, \tag{6.16}$$

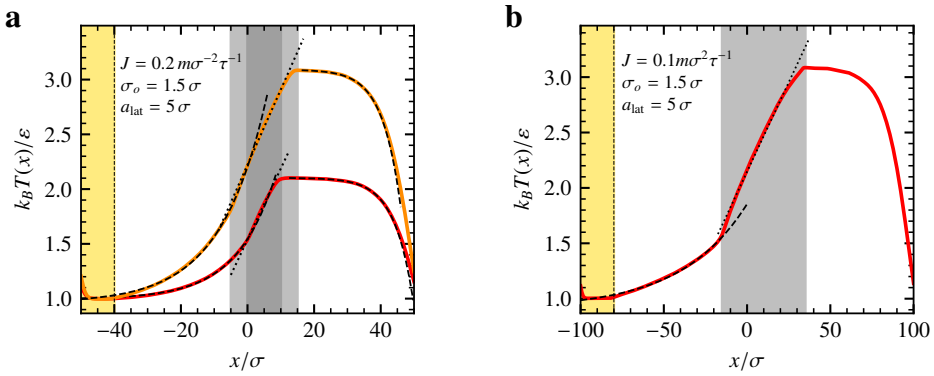

Figure 6.6: Temperature profiles, exponential (dashed) and linear (dotted) fitted curves for simulations with different width of the porous medium. Lattice parameters are (a) $n_x = 2$ (red), $n_x = 4$ (orange) and (b) $n_x = 10$. The box length in x direction in simulations of panel (a) is $100\,\sigma$, which is extended to $200\,\sigma$ in simulation of panel (b) to provide required inlet and outlet lengths.

which introduces the length scale ℓ. The behaviour is shown in fig. 6.6. It rises exponentially before the medium, following a linear increase inside the medium, creates a plateau as far as the outlet size permits and then falls again as it approaches the thermostat. The linear growth of temperature is better seen in wider media.

6.3 Conclusions

We have investigated the response of a boundary-driven LJ fluid flow through a model porous medium composed of bead packings located on an fcc lattice. The porosity of the medium affects the behavior of the passing fluid. The flow-pressure relation is examined and found to be linear for small pressure gradients, only in high porosities and the dependence of the linear permeability on the porosity of the medium is presented. It is observed that the linear response regime breaks down significantly for low porosities. The simulations further exhibit an exponential temperature rise in the inlet and a constant temperature profile in the outlet region. This behavior has been rationalized using thermal and caloric equations of state and conservation laws.

6.4 Supplemental information

6.4.1 Simulation parameters

The simulated fluid consists of particles of mass m interacting with Lennard-Jones potential $U_{\text{LJ}}(r) = 4\varepsilon((\sigma/r)^{12} - (\sigma/r)^6)$. The potential is shifted and smoothly truncated for $r < r_c$ as $U(r) = [U_{\text{LJ}}(r) - U_{\text{LJ}}(r_c)]g((r - r_c)/h)$, where r_c is the cutoff radius, the trucation funcation

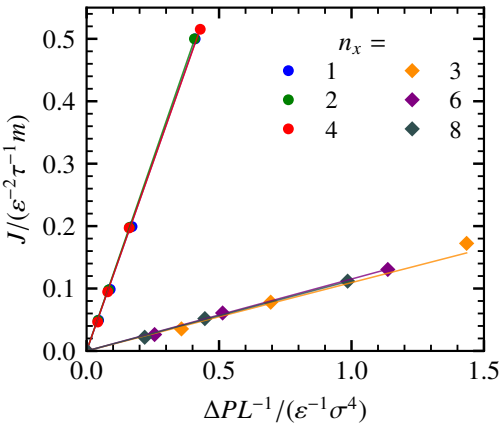

Figure 6.7: Dependence of mass current J on the length of the porous medium L. Simulations are done in the same state ($T_{\text{base}} = 1\varepsilon/k_B, \varrho = 0.8\sigma^{-3}$). Different mass currents J are generated to pass through the porous medium with obstacle size $\sigma_{obst} = 1\sigma$ and $a_{\text{lat}} = 5\sigma$ represented by discs and with obstacle size $\sigma_{obst} = 1.05\sigma$ and $a_{\text{lat}} = 3\sigma$ represented by diamonds. Different colors indicate n_x, changing the length of the medium. The slopes of the lines indicate k/ν.

$g(x) = x^4/(1+x^4)$ and $h = 0.005$. The cutoff radius in the interaction of particles with particles is $r_c = 2.5\sigma$ and in the interaction with obstacles is $r_c = 2^{1/6}\sigma$ to avoid the possibility of sticking particles to obstacles. The obstacles are not interacting with each other $\varepsilon_{\text{o-o}} = 0$. The simulations are done in a cubic box of size $100\sigma \times 30\sigma \times 30\sigma$ with periodic boundary conditions being applied in all directions. The box is symmetrical in the y and z directions and different regions are divided by planar interfaces with a normal vector in x direction.

The density of the fluid is $0.805\sigma^{-3}$ and the temperature is set to be $1\varepsilon/k_B$ with a thermostat and a pump located on the border of the box covering a region of size $10\sigma \times 30\sigma \times 30\sigma$. The stochastic thermostat resamples velocities with an update rate $\Gamma = 8\tau^{-1}$. The timestep is 0.002τ and this means the velocites are resampled approximately every 62 steps by generating random velocities with the target mean velocity $\vec{v}_i \sim \mathcal{N}(\vec{v}_t, k_B T/m)$. We covered velocities in the range of 2.5% to 62.5% of the thermal velocity.

The accessible volume to the particles changes with the number and size of the obstacles. The number of particles is set accordingly to keep the same density in all simulations. In absence of obstacles, the number of particles is 72000. The porous medium is created by placing a number of obstacles on a fcc lattice in the middle of the box, far enough from the pump. The length of the medium is $L = (n_x - 1/2)\, a_{\text{lat}} + 2\sigma_o$.

According to Darcy's law eq. (6.1), the length of the medium L should scale out when calculating the permeability in the limit of large L. Using different sizes, fig. 6.7 shows the effect of L is as expected by the equation. For the medium with low density, the simulations are done

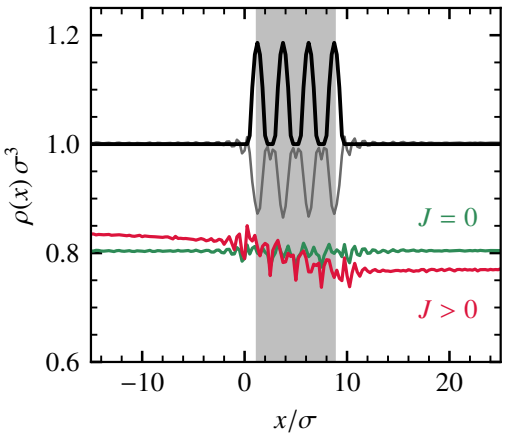

Figure 6.8: Density and the correction function. The density profile is multiplied by a correction function $f(x)$ shown with the black line which is determined due to the accessible space in the medium. The gray curve represents the equilibrium density profile before correction and is shifted ($\varrho(x)+0.2$) for clarity. The two remaining profiles are the results after the correction for equilibrium (green) and non-equilibrium (red).

with lattice parameters ($n_x = 2, a_{\text{lat}} = 5\sigma$) and we expect to get the same permeability for any medium size. For the medium with higher density, however, the behavior is a little different for the smaller medium size but not very noticiable in this plot. For the denser medium, our choice is ($n_x = 6, a_{\text{lat}} = 3\sigma$).

6.4.2 Correcting the density for the excluded volume

The density in the medium is corrected for the excluded volume by the obstacles. At each point in x direction, the modifier function f is determined by calculating the occupied area of the corresponding yx plane by obstacles. In this calculation, the effective radius of the obstacles are determined by comparing the density profile inside and outside the medium in equilibrium (more details in appendix B). In fig. 6.8, the effective radius of obstacles whose interaction with fluid particles has been considered $\sigma_o = 1\sigma$ is found to be $r = 0.79\sigma$ to get the best possible result. This difference is because particles are not hard spheres and they penetrate. Each obstacle makes a sphere of this determined radius inaccessible to the center of fluid particles.

6.4.3 Thermodynamic observables

For the calculation of thermodynamic observables, the simulation box is partitioned into a number of slabs of width $\delta L = 2.5\sigma$, and area $L_y L_z = (15\sigma)^2$ along the x-axis. In intervals of 300 steps ($\Delta t = 0.002 * 300 = 0.6\tau$), the thermodynamic properties are calculated in these slabs,

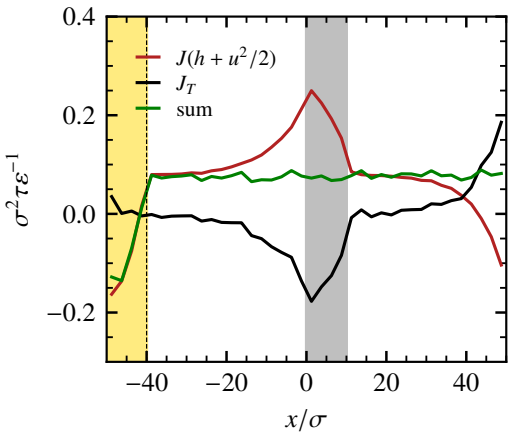

Figure 6.9: Enthalpy flux, heat flux and the summations as shown in the legend for a simulation with lattice constants ($a_{\text{lat}} = 5\sigma, n_x = 2$) and with $J = 0.2m\sigma^{-2}\tau^{-1}$ and $\sigma_o/\sigma = 1$.

but density is calculated in a fine grid (and not in slabs). Temperature is calculated from the kinetic energy of the particles. Pressure is calculated from the virial and we have validated it with the method of planes [137–139]. The mass flux was obtained as $J = (1/V)\sum_{i=0}^{N} \vec{p}_i$, where V is the volume of the slab. The heat flux J_T is calculated using the stress tensor, $J_T = (1/V) < \sum_{i=1}^{N} \vec{v}_i e_i + Q >$, where $Q = (1/2)\sum_{i=1}^{N}\sum_{i\neq j}(\vec{r}_{ij} \otimes \vec{F}_{ij}) \cdot \vec{v}_i$, and e_i is the total energy of particle i. As there is a net flux in one direction and this changes the calculated heat flux, J_T is corrected to eliminate the effect of center of mass velocity of the particles in each slab, $J_T^* = \frac{1}{V}\left\langle \sum_{i=1}^{N}(\vec{v}_i - \vec{v}_{cm})(u_i + \frac{m}{2}(\vec{v}_i - \vec{v}_{cm})^2) + (1/2)\sum_{i=1}^{N}\sum_{i\neq j}(\vec{r}_{ij} \otimes \vec{F}_{ij}) \cdot (\vec{v}_i - \vec{v}_{cm})\right\rangle$. And finally, the enthalpy is calculated as $h = e + P/\rho$.

6.4.4 Local conservation of energy

The sum of the enthalpy flux and the heat flux results in a constant value. This behavior could be expected from conservation of energy as in eq. (6.8). We have considered the last term τu negligible.

6.4.5 Material parameters

In table 6.1, the isochoric specific heat per particle c_V, the isothermal compressibility χ_T, and the shear viscosity η were calculated at the specified temperature and density using standard simulations for a homogeneous sample of bulk liquid [39, 90]. The heat conductivity κ and the thermal expansion coefficient α were obtained via eqs. (6.9) and (6.14) from the non-equilibrium simulations in presence of the porous medium, i.e., the x-dependence of α and κ

temperature	$T=$	1.0	1.51	2.12	ε/k_B
mass density	$\varrho=$	0.98	0.91	0.60	$m\sigma^{-3}$
pressure	$P=$	*7.79	7.710	2.371	$\varepsilon\sigma^{-3}$
internal energy	$e=$	*−4.81	−2.303	0.116	ε/m
enthalpy	$h=$	*3.56(± 0.4)	6.170	4.068	ε/m
isochoric specific heat	$c_V=$	*3.217	2.55	1.849	k_B/m
	=		2.568	1.895	k_B/m
isobaric specific heat	$c_P=$	*4.78	**3.96	**3.73	k_B/m
	=		3.90	3.76	k_B/m
compressibility	$\chi_T=$	*0.0194	*0.0235	*0.1431	σ^3/ε
	=		0.0247	0.145	σ^3/ε
thermal expansion coefficient	$\alpha=$	*0.173	*0.141	*0.277	k_B/ε
shear viscosity	$\eta=$		3.52(6)	0.89(2)	$\sigma^3\tau/\varepsilon$
heat conduction	$\kappa=$		9.86		
speed of sound	$c_s=$	*7.252	6.670	3.390	σ/τ
Mach number	Ma=	*0.028	0.033	0.064	

Table 6.1: Thermodynamic properties, material constants, and transport coefficients of the LJ liquid at the state point (ϱ, T). The first set of parameters are for the inlet far from the porous medium. The middle set is for the inlet and next to the medium and the last set is for the point, right after the medium in the outlet region. Numbers in parentheses give the uncertainty in the last digit. The numbers shown with $*$ are calculated from the thermal or caloric equations of state and in calculation of parameters with $**$, both the equation of state and the bulk results are used. For the state point in the inlet and far from the media, the parameters cannot be calculated from the bulk in equilibrium because of crystallization.

in the inlet region yields their values along an isobar of the fluid, within the approximation of local equilibrium.

7 Fluid Flow Through Porous Media in an Open System

We discussed the fluid flow through a model porous medium in chapter 6, and in this chapter, a similar setup will be simulated in AdResS to reproduce those results for an open system in contact with reservoirs of particles and energy. Additionaly, AdResS will be employed to decrease the outlet size by using open boundaries and coupling the system to appropriate reservoirs.

7.1 Simulation setup

As in the previous chapter, the fluid is driven at the boundary of the inlet by a thermostat pump (section 3.4.3). The system is coupled to reservoirs of particles and energy, where momentum-conserving Maxwell-Boltzmann thermostats are acting (section 3.4.3) to avoid the flux being suppressed. In other words, the thermostat in the left transition region (Δ) sets the prescribed velocity, whereas the thermostats in the other Δ region and in both TR regions conserve center of mass velocity in each thermostat region independently. The high-resolution region (AT) that represents the open subsystem has Hamiltonian dynamics and no thermostat is applied there (fig. 7.1). The reference full-resolution simulations are also performed in the same setup and with a dense LJ liquid with $\varrho = 0.8\sigma^{-3}$ and $T = 1\varepsilon/k_B$ to test the applicability of AdResS.

As explained in chapter 2 and applied in chapter 4, an external one-body force must be calculated prior to the main simulation and applied throughout the box, in order to get the desired state in the AdResS system. In the absence of particle flow, the macroscopic state of the system is specified by temperature and density . However, when a particle flow is present, the macroscopic state (T, ϱ) is extended to (T, ϱ, J) [49], and it is important to set J in addition

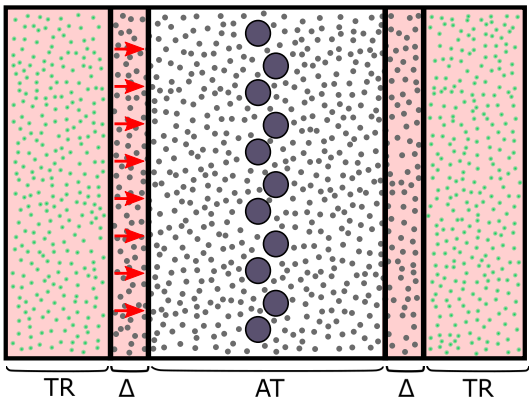

Figure 7.1: The AdResS simulation setup. The open system (white region) is embedded in the reservoirs connected to the thermostats (red shaded area). The pump is located in the left Δ region and the arrows show the direction of the center of mass velocity given to particles passing through the pump. The large particles in the middle of the open system represent the obstacles, and the smaller ones are the LJ particles. The very small particles in the shaded area are non-interacting tracer particles.

to T and ϱ when calculating the thermodynamic force. This changes the thermodynamic force profile, especially near the pump (fig. 7.2).

There are no obstacles in the box during the iterative computation of the thermodynamic force, and the obstacle will be located in the middle of the box in the main simulation. The medium length is $1.5a_{\text{lat}} + 2\sigma_o$, consisting of 288 obstacles, placed on a fcc lattice with a lattice constant of $a_{\text{lat}} = 5\sigma$ and different obstacle sizes σ_o (fig. 7.1).

7.2 Results

7.2.1 Periodic boundaries

In chapter 6, the Darcy's law, $J = (k/vL)\Delta P$, was examined for regular bead packings and found to be linear in low porosities and small pressure gradients.

To check the applicability of the AdResS approach, we reproduce those results with the same periodic boundaries by connecting the open system to the reservoirs at the same state. To that end, one thermodynamic force at $T = 1\varepsilon/k_B$, $\varrho = 0.8\sigma^{-3}$, and a J is calculated for each state. We tested four different mass currents ($J = 0.05, 0.1, 0.2$ and $0.5m\sigma^{-2}\tau^{-1}$) passing through three different mediums made up of the same number of obstacles but varying in size (σ_o).

The permeability calculated from the AdResS approach matches that calculated from the full resolution method. In particular, for smaller mass currents, the results are remarkably similar. There is a slight difference in large driving forces, and the produced current and pressure

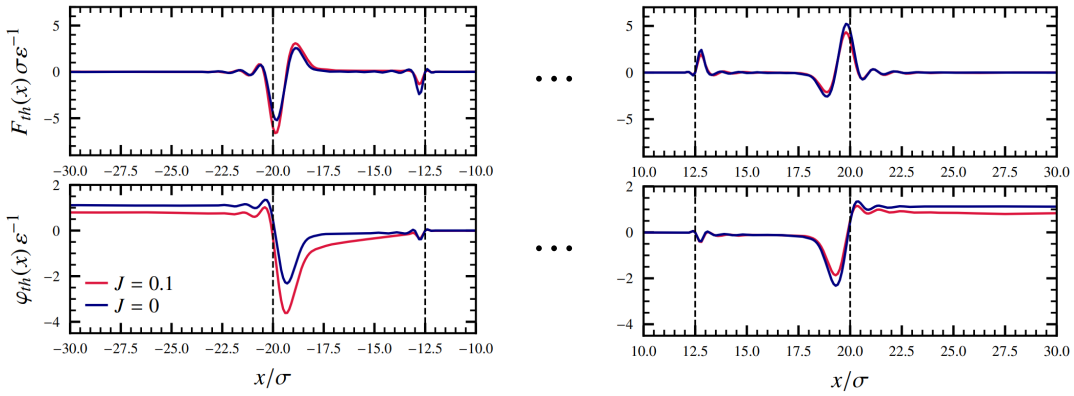

Figure 7.2: Thermodynamic forces and potentials in the same system with $J = 0$ and $J = 0.1\sigma^{-2}\tau^{-1}m$ in x direction. This one-body force is calculated once before the main simulation to guarantee that the proper temperature, density, and mass current are maintained throughout the box. The presence of J in the simulation alters this force and its associated potential.

gradient show a small difference, but the proportion remains close to the fitted line, and the permeability remains unchanged (fig. 7.3). The permeability k depends on the porosity φ as $k \sim (1-\varphi)^{-1}$ (chapter 6) and is well reproduced by AdResS.

The thermodynamic properties of the AdResS and full-resolution results are compared in fig. 7.4. As in the Δ region of the inlet, a steady mass flux is propagated through the box, leading to a pressure drop . The pressures are calculated with the method of planes [137] in the AdResS setup. The expected exponential increase in temperature in the inlet region (chapter 6) is reproduced with the AdResS. AdResS results show peaks in the temperature and near the boundary between the Δ and TR regions. This peak is due to the excess energy resulting from switching on the interactions of previously non-interacting tracers abruptly. The thermostat limits this excess energy and the temperature relaxes to the thermostat value ($T = 1\varepsilon/k_B$) within both the Δ and TR regions. The thermodynamic observables are very well reproduced by AdResS and in the worst case, which is for large obstacle sizes and driving forces, the error does not exceed 10% for $J = 0.5m\sigma^{-2}\tau^{-1}$. This reduces to 5% for $J = 0.2m\sigma^{-2}\tau^{-1}$.

7.2.2 Open boundaries

The pressure profiles in the outlet and inlet regions are constant, and there exists mechanical equilibrium in these regions. However, the inlet and outlet regions should be wide enough so that the convergence of the temperature and density profiles to the constant value can be reached in the outlet and the exponential increase in the temperature can be seen in the

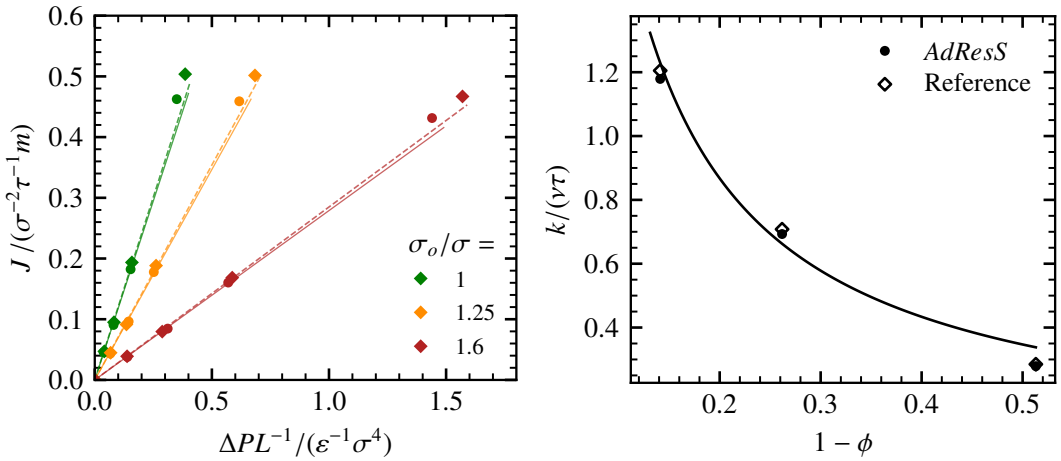

Figure 7.3: Flow–pressure relation (left) and dependence of permeability on porosity (right), in AdResS (diamonds and dashed lines) and full-resolution (discs and solid lines) simulations. As stated in the legend, different colors correspond to different obstacle sizes. In the right panel, the solid line is $k/\eta \sim 1/(1-\varphi)$.

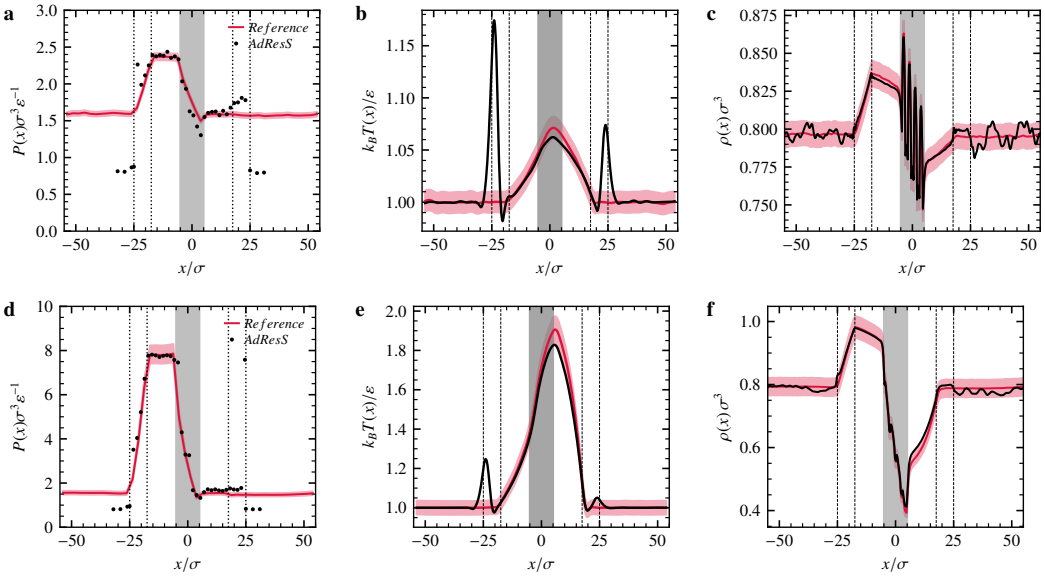

Figure 7.4: Spatial profiles of thermodynamic properties in AdResS (black) and full-AT (red) simulations. Panels (a), (b) and (c) are pressure, temperature and density profiles for $J = 0.1m\sigma^{-2}\tau^{-1}$ and $\sigma_o = 1\sigma$. Panels (d), (e) and (f) are for $J = 0.2m\sigma^{-2}\tau^{-1}$ and $\sigma_o = 1.6\sigma$. The gray region represents the model porous medium. The red shaded area around the profiles of temperature and density show 1% error around the reference simulation results in (b) and (c) and 3.5% in (e) and (f). For pressure profiles the shaded area shows 2% error in panel (a) and 5% in panel (d) in which the elevation in inlet region ($x < -5\sigma$) is much less than the elevation in outlet region ($x > 5\sigma$).

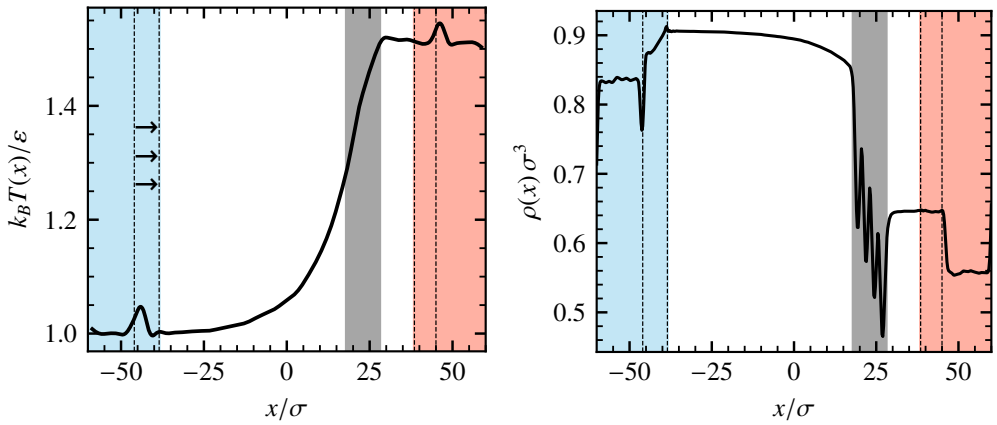

Figure 7.5: Temperature (left) and density (right) profiles of AdResS simulation of an open system in contact with two different reservoirs. The outlet region is $L = 10.5\sigma$ wide and is much smaller than than the outlet region in full resolution simulations. The TR and Δ regions are 14σ and 7.5σ in this simulation setup.

inlet, leading to the correct temperature inside the medium. The temperature drop in the outlet region is due to the connection of the outlet to the thermostat according to periodic boundaries, and it can be avoided near the medium by enlarging the outlet region. AdResS helps in reducing the outlet size by opening the boundaries and connecting the system to different reservoir states. This needs the tuning of the thermodynamic forces in the inlet and outlet regions for the state of the system after placing the medium. So new thermodynamic forces should be calculated for inlet and outlet regions and added linearly [22, 33, 34].

We need to know the reservoir states, so we run a full-resolution simulation in a small box to estimate the density and temperature values at the inlet, near the thermostat, and at the outlet, near the medium. Two thermodynamic forces at these temperatures and densities are calculated. Because the temperature and density values in the outlet and inlet are not accurate in small system sizes, an iterative change of $\mathbf{F}_{\text{th}}$ may be required.

We tested this with $J = 0.2m\sigma^{-2}\tau^{-1}$ and $\sigma_o = 1.25\sigma$ by running a small full resolution simulation and estimating the plateau values and correcting then iteratively. We found that the density and temperature plateaus are near ($\rho_1 = 0.91\sigma^{-3}$, $T_1 = 1\varepsilon/k_B$) and ($\rho_2 = 0.67\sigma^{-3}$, $T_2 = 1.51\varepsilon/k_B$). Connecting the open system to these reservoirs results in fig. 7.5.

To test the method, a reference simulation with very large oulet and inlet sizes was run, and the AdResS results were verified as satisfactory. The outlet size in the full resolution simulation to reach the appropriate temperature and density values is 60σ which is reduced to 10.5σ in AdResS simulation setup, and the clear temperature and density platesus are reproduced. The density profile in the TR regions are different from the prescribed value. This is due to the

periodic boundaries and connection of the thermostats at the border of the box. The inlet size cannot be changed as it is needed according to the physics of the system.

7.3 Conclusion

We identified a high level of consistency between AdResS simulation results and those of the reference simulation, showing that AdResS is capable of reproducing the reference results at a reduced computing cost and with a well-founded implementation of the open boundaries. In modeling fluid flow through the porous medium, examined in chapter 6, wide enough outlet and inlet regions are required in order for the proper temperature to emerge. AdResS can significantly decrease the outlet size while maintaining the right behavior.

8 Conclusions and Outlook

This thesis focuses on non-equilibrium molecular dynamics simulations of open systems. To this end, the grand canonical Adaptive Resolution Simulation (GC-AdResS) technique [17] has been extended to simulate out of equilibrium conditions along with the Bergmann-Lebowitz stochastic model of open systems [33, 34], which is based on adding the actions of independent, concurrent reservoirs. This enables the control of the reservoir states by applying thermodynamic forces prepared for the desired macroscopic states and combining them to drive the system out of equilibrium. This extension has been tested for open systems in non-equilibrium in the presence of heat and mass fluxes.

In the first test, the method has been used to simulate a Lennard-Jones fluid with open boundaries exposed to two different reservoirs along the same isobar, which are at the same pressure but different densities and temperatures [22]. As a result of applying this temperature gradient, a heat flux was generated and AdResS could accurately reproduce the full resolution simulations, where the system is in contact with large reservoirs of particles and energy, and all the particles of the system are considered in detail.

The approximations in the method and the theoretical model, which ignore the microscopic origin of the reservoirs and consider the linear combination of the reservoir actions, raise a question about the validity range of these approximations and the applicability of AdResS. By increasing the thermal gradient, it has been demonstrated that the method is applicable at least in the tested range which is temperature difference of 40% relative to the mean temperature, and that the results closely follow the results of the corresponding, full-resolution reference simulations. On the other hand, the method has been tested in an isochoric setup, where the reservoirs are at the same density but different temperatures, putting them at different pressures. The thermodynamic forces were calculated for these two states and combined. It has been shown that with the isochoric setup, the resulting densities in the reservoirs are not

as prescribed, but this does not affect the boundaries of the atomistic open system (*AT* region) and the behavior is similar to the isobaric and full resolution setups. These tests confirm the method, helping to simulate more realistic systems in connection to thermal gradients.

In the next step and before modeling the mass flux in AdResS, a non-equilibrium molecular dynamics simulation of a boundary driven fluid flow through a model porous medium has been performed, and the blocking of the flow has been examined in a full-resolution, closed system with periodic boundary conditions. The flow was generated by a "pump" in the boundary, giving the particles a velocity in the range of 6 to 60 % of their thermal velocity. The flow–pressure relation and its dependence on the porosity of the medium were studied and we have found that the Darcy's law is followed in low pressure gradients and mass currents and the linear permeability varies over two orders of magnitude and vanishes below a critical porosity. For porosities greater than this critical value and for high pressure gradients, there exist significant deviations from the linear regime. The simulations show an exponential increase in the temperature in the inlet region followed by a linear increase inside the medium, which has been rationalized via non-equilibrium thermodynamics, using conservation laws and the thermal and caloric equations of state.

Following this study, the fluid flow in an open system has been simulated with a similar setup in AdResS, with the pump being located at one border of the open system and connecting the open system to two reservoirs. The results of AdResS closely match the full resolution results, even under strong driving. On the other hand, AdResS has been used to simulate open boundaries instead of periodic boundaries, which allows one to decrease the size of the outlet significantly.

In this thesis, simulations were based on truncated, short-range Lennard-Jones interaction potentials, and one can expect different results with long-range potentials like electrostatic potential. Furthermore, the cuboid geometries of the high resolution open systems (*AT* regions) studied here can in principle be changed to spherical geometries to simulate e.g., droplet evaporation. Further, the simulation of hydrated membranes in thermal gradients is one of the method's possible applications. Experiment results show non-uniform temperature fields around the membranes of living cells [11], and controlling the thermal gradient may help to control the shape of the membrane. Additionally, the porous media have been simulated in this work using regular bead packings, which could be replaced with randomly located bead packings and nanochannels for future research. Some other applications which could be interesting include the investigation of species separations in gases moving through nanoporous media and osmotic flow across membrane proteins that function as channels.

A More Details on Lowe Andersen Thermostat

The Lowe-Andersen thermostat is a Galilean invariant version of the Andersen thermostat that conserves momentum [50]. It has a much smaller impact on the dynamics of the system than the Andersen thermostat. This method thermalizes the relative velocity of pairs of particles rather than the velocity of individual particles.

In the original Andersen thermostat, if the collision rate is high enough, the second momentum update is performed by selecting random numbers from the Maxwell distribution. The new velocity of ith particle $\mathbf{v}_i^*$ is

$$\mathbf{v}_i^* = \begin{cases} \mathbf{v}_i(t), & \Gamma\Delta t < \zeta \\ \lambda. & \Gamma\Delta t \geqslant \zeta \end{cases} \tag{A.1}$$

In this equation, Γ is the thermostat's collision rate, ζ is a random number from a uniform distribution with a range of $[0,1)$, and λ is a random vector with independent elements drawn from a Gaussian distribution with a mean of zero and a width of $\sqrt{K_B T/m}$.

The Lowe-Andersen thermostat is based on Andersen and adjusted step by step to conserve angular and linear momentum. The coordinates and momenta of a selected pair of particles in the system are shown with $(\mathbf{r}_i, \mathbf{p}_i)$ and $(\mathbf{r}_j, \mathbf{p}_j)$. If the distance between the two particles, $dr = |\mathbf{r}_i - \mathbf{r}_j|$, is larger than a specified radius, R_T, the process is deterministic; otherwise, the pair is selected and the stochastic update may be applied instead of deterministic update if the Andersen thermostat condition is met. For now we consider same mass for all particles for simplicity. For particles with the same mass, the center of mass velocity of the particles $\mathbf{v}_{cm}$

and their relative velocity $\mathbf{v}_{ij}$ is represented by

$$\begin{cases} \mathbf{v}_{cm} = \dfrac{\mathbf{v}_i + \mathbf{v}_j}{2}, \\ \mathbf{v}_{ij} = \mathbf{v}_i - \mathbf{v}_j. \end{cases} \tag{A.2}$$

The unit separation vector is $\hat{\boldsymbol{\sigma}}_{ij} = (\mathbf{r}_i - \mathbf{r}_j)/|\mathbf{r}_i - \mathbf{r}_j|$.

In order to conserve linear momentum, a random relative velocity related to the deterministic relative velocity $\mathbf{v}_{ij}$ is chosen. This random relative velocity is also chosen to be parallel to the separation vector in order to conserve angular momentum, so we consider

$$\mathbf{v}'_{ij} \cdot \hat{\boldsymbol{\sigma}}_{ij} = 2\lambda - \mathbf{v}_{ij} \cdot \hat{\boldsymbol{\sigma}}_{ij}. \tag{A.3}$$

where λ is a Gaussian random number. The new particle velocities are set to be the pair's shifted center of mass velocity in opposite directions,

$$\begin{cases} \mathbf{v}_i^* = \mathbf{v}_{cm} + \dfrac{1}{2}\mathbf{v}_{ij}^*, \\ \mathbf{v}_j^* = \mathbf{v}_{cm} - \dfrac{1}{2}\mathbf{v}_{ij}^*. \end{cases} \tag{A.4}$$

By inserting (A.3) into (A.4) we get

$$\begin{cases} \mathbf{v}_i^* = \dfrac{1}{2}(\mathbf{v}_i + \mathbf{v}_j) + \dfrac{1}{2}\left[\mathbf{v}_{ij} + (2\lambda - \mathbf{v}_{ij} \cdot \hat{\boldsymbol{\sigma}}_{ij})\hat{\boldsymbol{\sigma}}_{ij}\right] = \mathbf{v}_i + (\lambda - \dfrac{1}{2}(\mathbf{v}_i - \mathbf{v}_j) \cdot \hat{\boldsymbol{\sigma}}_{ij})\hat{\boldsymbol{\sigma}}_{ij}, \\ \mathbf{v}_j^* = \dfrac{1}{2}(\mathbf{v}_i + \mathbf{v}_j) - \dfrac{1}{2}\left[\mathbf{v}_{ij} + (2\lambda - \mathbf{v}_{ij} \cdot \hat{\boldsymbol{\sigma}}_{ij})\hat{\boldsymbol{\sigma}}_{ij}\right] = \mathbf{v}_j - (\lambda - \dfrac{1}{2}(\mathbf{v}_i - \mathbf{v}_j) \cdot \hat{\boldsymbol{\sigma}}_{ij})\hat{\boldsymbol{\sigma}}_{ij}. \end{cases} \tag{A.5}$$

This results in the following rules for updating the velocity of a pair of particles with different masses and reduced mass μ

$$\mathbf{v}_i^* = \begin{cases} \mathbf{v}_i(t), & \Gamma\Delta t < \zeta \\ \mathbf{v}_i + (\mu_{ij}/m_i)(\lambda - \dfrac{1}{2}(\mathbf{v}_i - \mathbf{v}_j) \cdot \hat{\boldsymbol{\sigma}}_{ij})\hat{\boldsymbol{\sigma}}_{ij}, & \Gamma\Delta t \geqslant \zeta \end{cases} \tag{A.6}$$

$$\mathbf{v}_j^* = \begin{cases} \mathbf{v}_j(t), & \Gamma\Delta t < \zeta \\ \mathbf{v}_j - (\mu_{ij}/m_j)(\lambda - \dfrac{1}{2}(\mathbf{v}_i - \mathbf{v}_j) \cdot \hat{\boldsymbol{\sigma}}_{ij})\hat{\boldsymbol{\sigma}}_{ij}. & \Gamma\Delta t \geqslant \zeta \end{cases} \tag{A.7}$$

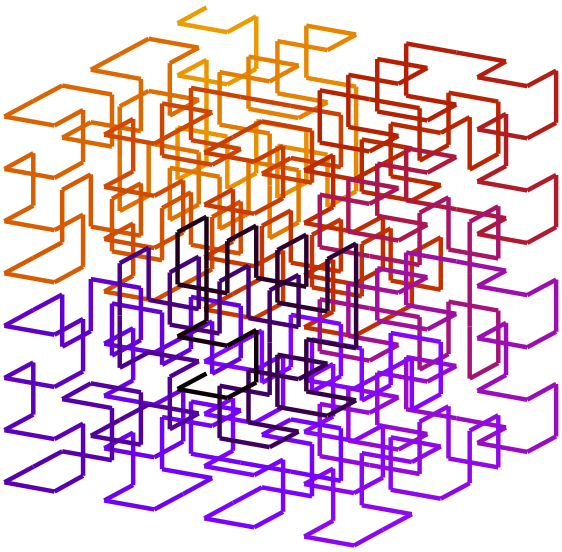

Figure A.1: The particles in HALMD are sorted in memory according to the Hilbert space-filling curve. The successive particles in the memory are most likely spatially close to each other as well. Figure from [**colberg_2011**]

We implemented this algorithm in the "finalize" step of the integration scheme by choosing pairs of successive particles in the memory.

Our algorithm differs from the original algorithm in that there are no collision cells in the system from which to choose the pairs in the original algorithm, and all possible pairs can be chosen, though they will be discarded if the distance is greater than R_T. Although we lack cells, particles in HALMD are sorted in memory using the space-filling Hilbert curve and we choose neighbor pairs in memory. The Hilbert curve provides a mapping between one-dimensional and high-dimensional spaces that preserves locality reasonably well. This means that two data points that are close together in one dimension are also close together in high dimensions. So in our case, the interacting particles, being close in space, are also close in memory for higher efficiency.

As previously stated, we select pairs of successive particles, and there is a high likelihood that the selected particles are not far in space, and the condition of having less distance than a threshold will be met. It should be noted that low collision rates in our algorithm are equivalent to higher collision rates in the original algorithm because we'll have more successful pair choosing.

This algorithm is tested for a liquid with ($\varrho = 0.7\sigma^{-3}$) containing 3000 particles to set the target temperature to be ($T = 2k_B/\varepsilon$). The equilibration and production runs were 200 and 400τ respectively with timestep 0.002 and the sampling was done in intervals of 100 timesteps. We

chose $R_T = 5\sigma$ and $\Gamma = 10$, and the resulted temperatures for the Lennard-Jones and ideal gas particles for simulations on CPU and GPU are as follows:

–	LJ	Ideal gas
CPU	1.959 ± 0.002	1.809 ± 0.005
GPU	1.968 ± 0.003	1.891 ± 0.003

There exists about 2% error in the system's final temperature in LJ and $5\% - 10\%$ in ideal gas, that cannot be eliminated in any way. To identify the problem, we ran simulations beginning with the Andersen method and gradually adding elements of the Lowe-Andersen thermostat.We discovered that going backward and adding and removing a random velocity to the $\mathbf{v}_{cm}$ solves the issue. This means that the discrepancy appears when the condition of angular momentum conservation enters the algorithm by selecting the new velocity to be along the separation vector. With the following velocities, we get better results for temperature, as shown in the table below.

$$\mathbf{v}_i^* = \begin{cases} \mathbf{v}_i(t), & \Gamma\Delta t < \zeta \\ \mathbf{v}_i + (\mu_{ij}/m_i)\lambda & \Gamma\Delta t \geqslant \zeta \end{cases} \tag{A.8}$$

$$\mathbf{v}_j^* = \begin{cases} \mathbf{v}_j(t), & \Gamma\Delta t < \zeta \\ \mathbf{v}_j - (\mu_{ij}/m_j)\lambda & \Gamma\Delta t \geqslant \zeta \end{cases} \tag{A.9}$$

–	LJ	Ideal gas
CPU	1.993 ± 0.001	1.988 ± 0.002
GPU	1.987 ± 0.001	1.945 ± 0.002

The cause of this problem could be a hidden correlation between the separation vectors and the center of mass velocities. Assume the particle positions are on the XY plane, so the separation vector is also on the XY plane. If the particle velocities are in the Z direction, $\mathbf{v}_{cm}$ and $\mathbf{r}_{ij}$ are perpendicular, resulting in a temperature error. More precise and detailed research on this topic could be conducted to determine the exact root cause, but it was beyond the scope of this thesis as well as the time available.

B Calculation of Excluded Volume in Porous medium

In a porous medium, the obstacles occupy space and reduce the accessible volume of the fluid particles. This affects the density, current density, and pressure profiles inside the medium.

To correct for this effect, we must compute the "excluded-volume", which is the volume over which the center of a fluid particle can move. By assuming the obstacles and particles to be hard spheres, their centers cannot be less than 1σ apart. This means that each obstacle prevents the fluid particles from accessing a volume of $(4/3)\pi\sigma^3$.

To ensure that our assumption holds true in our case, we run a simulation in which the particles do not interact with one another and the only interaction in the system is particle-obstacle interaction.

The fluid contains 72000 particles, and the entire box is thermalized using an Andersen thermostat set to $T = 1k_B/\varepsilon$. Near the center of the box is a model porous medium made of obstacles on a fcc lattice. The number of particles inside and outside the medium is recorded after 100τ.

Clearly, the total density in the system can be written as a weighted mean of it in different regions taking volume into account.

$$\varrho^*_{tot} = \frac{\varrho_{out} L_{out} + \varrho^*_{in} L_{in}}{L}, \tag{B.1}$$

Where parameters with superscript $*$ are corrected parameters concerning the volume. Parameters inside and outside the medium are shown with subscripts in and out respectively

and the parameters related to the whole box are shown with subscript tot. L is the whole length of the box in x direction.

Equation B.1 can be modified by $\varrho^*_{tot} = N_{tot}/V^*_{tot}$ and $\varrho^*_{in} = N_{in}/V^*_{in}$. The volume outside the medium V_{out} is not changed and is known. On the other hand $V^*_{tot} = V_{out} + V^*_{in}$. Replacing these parameters will lead to:

$$\frac{N_{tot}}{V_{out} + V^*_{in}} = \frac{\varrho_{out} L_{out} + \frac{N_{in}}{V^*_{in}} L_{in}}{L}, \tag{B.2}$$

and simplified to:

$$(\varrho_{out} L_{out}) V^{*^2}_{in} + (N_{out} L_{out} + N_{in} L_{in} - N_{tot} L) V^*_{in} + N_{in} L_{in} V_{out} = 0. \tag{B.3}$$

All of the above parameters are known, and solving this second order equation results in the accessible volume within the medium. The radius of the sphere is calculated from this, and in this case, where $\sigma = 1$, the radius of the sphere was 0.942σ. The difference between our options is that particles and obstacles are not truly hard spheres and can penetrate.

Bibliography

1. Demirel, Y. & Gerbaud, V. *Nonequilibrium Thermodynamics* (Elsevier, 2019).
2. Faucher, S. *et al.* Critical Knowledge Gaps in Mass Transport through Single-Digit Nanopores: A Review and Perspective. *J. Phys. Chem. C* **123,** 21309–21326 (2019).
3. Heinen, M., Vrabec, J. & Fischer, J. Communication: Evaporation: Influence of heat transport in the liquid on the interface temperature and the particle flux. *J. Chem. Phys.* **145,** 081101 (2016).
4. Sánchez-Díaz, L. E., Lázaro-Lázaro, E., Olais-Govea, J. M. & Medina-Noyola, M. Non-equilibrium dynamics of glass-forming liquid mixtures. *J. Chem. Phys.* **140,** 234501 (2014).
5. Ganti, R., Liu, Y. & Frenkel, D. Molecular Simulation of Thermo-osmotic Slip. *Phys. Rev. Lett.* **119,** 038002 (2017).
6. Todd, B. D. & Daivis, P. J. *Nonequilibrium Molecular Dynamics* (Cambridge University Press, Cambridge, 2017).
7. Onsager, L. Reciprocal Relations in Irreversible Processes. I. *Phys. Rev. Lett.* **37,** 405–426 (1931).
8. Onsager, L. Reciprocal Relations in Irreversible Processes. II. *Phys. Rev. Lett.* **38,** 2265–2279 (1931).
9. Groot, S. R. D. On the Development of Nonequilibrium Thermodynamics. *J. Math. Phys.* **4,** 147–153 (1963).
10. De Groot, S. R. & Mazur, P. *Non-equilibrium thermodynamics* (Courier Corporation, 2013).
11. Donner, J. S., Thompson, S. A., Kreuzer, M. P., Baffou, G. & Quidant, R. Mapping Intracellular Temperature Using Green Fluorescent Protein. *Nano Letters* **12,** 2107–2111 (2012).
12. Pascual, M., Poquet, A., Vilquin, A. & Jullien, M.-C. Phase separation of an ionic liquid mixture assisted by a temperature gradient. *Phys. Rev. Fluids* **6,** 024001 (2021).

13. Daglar, H., Erucar, I. & Keskin, S. Recent advances in simulating gas permeation through MOF membranes. *Mater. Adv.* **2,** 5300–5317 (2021).

14. Velioglu, S. & Keskin, S. Simulation of H2/CH4 mixture permeation through MOF membranes using non-equilibrium molecular dynamics. *J. Mater. Chem. A* **7,** 2301–2314 (2019).

15. Höfling, F. & Dietrich, S. Finite-size corrections for the static structure factor of a liquid slab with open boundaries. *J. chem. Phys.* **153,** 054119 (2020).

16. Joshi, S. Y. & Deshmukh, S. A. A review of advancements in coarse-grained molecular dynamics simulations. *Mol. Simul.* **47,** 786–803 (2021).

17. Delle Site, L. *et al.* Molecular Dynamics of Open Systems: Construction of a Mean-Field Particle Reservoir. *Adv. Theory Simul.* **2,** 1900014 (2019).

18. Whittaker, J. & Delle Site, L. Investigation of the hydration shell of a membrane in an open system molecular dynamics simulation. *Phys. Rev. Res.* **1,** 033099 (2019).

19. Cortes-Huerto, R., Praprotnik, M., Kremer, K. & Delle Site, L. From adaptive resolution to molecular dynamics of open systems. *Eur. Phys. J. B* **94,** 189 (2021).

20. *Highly Accelerated Large-scale Molecular Dynamics package* https://halmd.org.

21. Colberg, P. H. & Höfling, F. Highly accelerated simulations of glassy dynamics using GPUs: Caveats on limited floating-point precision. *Comput. Phys. Commun.* **182,** 1120–1129 (2011).

22. Ebrahimi Viand, R., Höfling, F., Klein, R. & Delle Site, L. Communication: Theory and Simulation of Open Systems out of Equilibrium. *J. Chem. Phys.* **153,** 101102 (2020).

23. Klein, R., Ebrahimi Viand, R., Höfling, F. & Delle Site, L. Nonequilibrium Induced by Reservoirs: Physico-Mathematical Models and Numerical Tests. *Adv. Theory Simul.* **4,** 2100071 (2021).

24. Fritsch, S. *et al.* Adaptive resolution molecular dynamics simulation through coupling to an internal particle reservoir. *Phys. Rev. Lett.* **108,** 170602 (2012).

25. Praprotnik, M., Delle Site, L. & Kremer, K. Adaptive resolution molecular-dynamics simulation: Changing the degrees of freedom on the fly. *J. Chem. Phys.* **123,** 224106 (2005).

26. Praprotnik, M., Delle Site, L. & Kremer, K. Multiscale Simulation of Soft Matter: From Scale Bridging to Adaptive Resolution. *Annu. Rev. Phys. Chem.* **59,** 545–571 (2008).

27. Delle Site, L. & Praprotnik, M. Molecular systems with open boundaries: Theory and simulation. *Phys. Rep.* **693,** 1–56 (2017).

28. Delle Site, L. Some fundamental problems for an energy-conserving adaptive-resolution molecular dynamics scheme. *Phys. Rev. E* **76,** 047701 (2007).

29. Kreis, K., Donadio, D., Kremer, K. & Potestio, R. A unified framework for force-based and energy-based adaptive resolution simulations. *EPL* **108,** 30007 (2014).

30. Potestio, R. *et al.* Hamiltonian Adaptive Resolution Simulation for Molecular Liquids. *Phys. Rev. Lett.* **110,** 108301 (2013).

31. Español, P. *et al.* Statistical mechanics of Hamiltonian adaptive resolution simulations. *J. Chem. Phys.* **142,** 064115 (2015).

32. Agarwal, A., Zhu, J., Hartmann, C., Wang, H. & Delle Site, L. Molecular dynamics in a grand ensemble: Bergmann–Lebowitz model and adaptive resolution simulation. *New J. Phys.* **17,** 083042 (2015).

33. Bergmann, P. G. & Lebowitz, J. L. New Approach to Nonequilibrium Processes. *Phys. Rev. Lett.* **99,** 578–587 (1955).

34. Lebowitz, J. L. & Bergmann, P. G. Irreversible gibbsian ensembles. *Ann. Phys.* **1,** 1–23 (1957).

35. Krekeler, C., Agarwal, A., Junghans, C., Praprotnik, M. & Delle Site, L. Adaptive resolution molecular dynamics technique: Down to the essential. *J. Chem. Phys.* **149,** 024104 (2018).

36. Kreis, K., Fogarty, A. C., Kremer, K. & Potestio, R. Advantages and challenges in coupling an ideal gas to atomistic models in adaptive resolution simulations. *Eur. Phys. J. Spec. Top.* **224,** 2289–2304 (2015).

37. Evans, R. The nature of the liquid-vapour interface and other topics in the statistical mechanics of non-uniform, classical fluids. *Adv. Phys.* **28,** 143–200 (1979).

38. Ciccotti, G. & Delle Site, L. The physics of open systems for the simulation of complex molecular environments in soft matter. *Soft Matter* **15,** 2114 (2019).

39. Hansen, J.-P. & McDonald, I. R. *Theory of Simple Liquids* (Elsevier, 2013).

40. Omelyan, I., Mryglod, I. & Folk, R. Symplectic analytically integrable decomposition algorithms: classification, derivation, and application to molecular dynamics, quantum and celestial mechanics simulations. *Comput. Phys. Commun.* **151,** 272–314 (2003).

41. Kirk, D. B. & Hwu, W.-m. W. *Programming Massively Parallel Processors* (Elsevier, 2017).

42. Stoltzfus, L., Emani, M., Lin, P.-H. & Liao, C. *Data Placement Optimization in GPU Memory Hierarchy Using Predictive Modeling Proceedings of the Workshop on Memory Centric High Performance Computing* (Association for Computing Machinery, 2018).

43. Höft, N. *Computer Simulations of Phase Behavior and Adsorption Kineticsin Metal–Organic Frameworks (MOFs)* PhD thesis (Heinrich-Heine-Universität Düsseldorf, 2016).

44. Bilbao stefan, s. & webb craig j., c. j. physical modeling of timpani drums in 3d on gpgpus. *J. Audio Eng. Soc.* **61,** 737–748 (2013).

45. Noguchi, H., Kikuchi, N. & Gompper, G. Particle-based mesoscale hydrodynamic techniques. *EPL* **78,** 10005 (2007).

46. Gompper, G., Ihle, T., Kroll, D. M. & Winkler, R. G. *Advanced Computer Simulation Approaches for Soft Matter Sciences III* 1–87 (Springer Berlin Heidelberg, Berlin, Heidelberg, 2009).

47. Andersen, H. C. Molecular dynamics simulations at constant pressure and/or temperature. *J. Chem. Phys.* **72,** 2384 (1980).

48. Stone, J. E. *et al.* Accelerating molecular modeling applications with graphics processors. *J. Comput. Chem.* **28,** 2618–2640 (2007).

49. Renner, J., Schmidt, M. & de las Heras, D. Custom flow in molecular dynamics. *Phys. Rev. Res.* **3,** 013281 (2021).

50. Lowe, C. P. An alternative approach to dissipative particle dynamics. *EPL* **47,** 145–151 (1999).

51. Koopman, E. A. & Lowe, C. P. Advantages of a Lowe-Andersen thermostat in molecular dynamics simulations. *J. Chem. Phys.* **124,** 204103 (2006).

52. Hoogerbrugge, P. J. & Koelman, J. M. V. A. Simulating Microscopic Hydrodynamic Phenomena with Dissipative Particle Dynamics. *EPL* **19,** 155–160 (1992).

53. Groot, R. D. & Warren, P. B. Dissipative particle dynamics: Bridging the gap between atomistic and mesoscopic simulation. *J. Chem. Phys.* **107,** 4423–4435 (1997).

54. Bird, G. Recent advances and current challenges for DSMC. *Comput. Math. Appl.* **35,** 1–14 (1998).

55. Alexander, F. J. & Garcia, A. L. The Direct Simulation Monte Carlo Method. *Computers in Physics* **11,** 588 (1997).

56. Malevanets, A. & Kapral, R. Mesoscopic model for solvent dynamics. *J. Chem. Phys.* **110,** 8605–8613 (1999).

57. Schilling, B. Potential truncation effects in molecular simulations. *Darmstadt* (2006).

58. D. Frenkel, B. S. *Understanding Molecular Simulation* (Elsevier, 2002).

59. Bocquet, L. Nanofluidics coming of age. *Nat. Mater.* **19,** 254–256 (2020).

60. Samin, S. & van Roij, R. Interplay Between Adsorption and Hydrodynamics in Nanochannels: Towards Tunable Membranes. *Phys. Rev. Lett.* **118,** 014502 (2017).

61. Falk, K., Sedlmeier, F., Joly, L., Netz, R. R. & Bocquet, L. Molecular Origin of Fast Water Transport in Carbon Nanotube Membranes: Superlubricity versus Curvature Dependent Friction. *Nano Lett.* **10,** 4067–4073 (2010).

62. Höft, N. & Horbach, J. Condensation of Methane in the Metal–Organic Framework IRMOF-1: Evidence for Two Critical Points. *J. Am. Chem. Soc.* **137,** 10199–10204 (2015).

63. Peksa, M., Burrekaew, S., Schmid, R., Lang, J. & Stallmach, F. Rotational and translational dynamics of CO_2 adsorbed in MOF $Zn_2(bdc)_2(dabco)$. *Micropor. Mesopor. Mat.* **216,** 75–81 (2015).

64. Spanner, M. *et al.* Splitting of the Universality Class of Anomalous Transport in Crowded Media. *Phys. Rev. Lett.* **116,** 060601 (2016).

65. Cho, H. W., Kwon, G., Sung, B. J. & Yethiraj, A. Effect of Polydispersity on Diffusion in Random Obstacle Matrices. *Phys. Rev. Lett.* **109,** 155901 (2012).

66. Scholz, C. *et al.* Permeability of Porous Materials Determined from the Euler Characteristic. *Phys. Rev. Lett.* **109,** 264504 (2012).

67. Gniewek, P. & Hallatschek, O. Fluid flow through packings of elastic shells. *Phys. Rev. E* **99,** 023103 (2019).

68. Tan, H., Wooh, S., Butt, H.-J., Zhang, X. & Lohse, D. Porous supraparticle assembly through self-lubricating evaporating colloidal ouzo drops. *Nat. Commun.* **10,** 478 (2019).

69. Römer, F., Bremse, F., Muscatello, J., Bedeaux, D. & Rubi, J. M. Thermomolecular Orientation of nonpolar fluids. *Phys. Rev. Lett.* **108,** 105901 (2012).

70. Duhr, S. & Braun, D. Thermophoretic depletion follows Boltzmann distribution. *Phys. Rev. Lett.* **96,** 168301 (2006).

71. Maeda, Y. T., Buguin, A. & Libchabe, A. Thermal Separation: Interplay between the Soret Effect and Entropic Force Gradient. *Phys. Rev. Lett.* **107,** 038301 (2011).

72. Debuschewitz, C. & Köhler, W. Molecular Origin of Thermal Diffusion in Benzene+Cyclohexane Mixtures. *Phys. Rev. Lett.* **87,** 055901 (2001).

73. Roy, S., Dietrich, S. & Maciolek, A. Solvent coarsening around colloids driven by temperature gradients. *Phys. Rev. E* **97,** 042603 (2018).

74. Würger, A. Molecular-weight dependent thermal diffusion in dilute polymer solutions. *Phys. Rev. Lett.* **102,** 078302 (2009).

75. Lervik, A., Bremse, F. & Kjelstrup, S. Heat transfer in soft nanosscale interfaces: the influence of interface curvature. *Phys. Chem. Chem. Phys.* **5,** 2407–2414 (2009).

76. Lervik, A., Bremse, F., Kjelstrup, S., Bedeaux, D. & Rubi, J. M. Heat transfer in protein-water interface. *Phys. Chem. Chem. Phys.* **12,** 1610–1617 (2010).

77. Bremse, F., Lervik, A., Bedeaux, D. & Kjelstrup, S. Water polarization under thermal gradient. *Phys. Rev. Lett.* **101,** 020602 (2008).

78. Delle Site, L. & Praprotnik, M. Molecular Systems with Open Boundaries: Theory and Simulation. *Phys. Rep.* **693,** 1–56 (2017).

79. Wang, H., Hartmann, C., Schütte, C. & Delle Site, L. Grand-canonical-like molecular-dynamics simulations by using an adaptive-resolution technique. *Phys. Rev. X* **3,** 011018 (2013).

80. Agarwal, A., Wang, H., Schütte, C. & Delle Site, L. Chemical potential of liquids and mixtures via Adaptive Resolution Simulation. *J. Chem. Phys.* **141,** 034102 (2014).

81. Delle Site, L. Formulation of Liouville's theorem for grand ensemble molecular simulations. *Phys. Rev. E* **93,** 022130 (2016).

82. Site, L. D. & Klein, R. Liouville-type equations for the in/i-particle distribution functions of an open system. *J. Math. Phys.* **61,** 083102 (2020).

83. Delle Site, L., Praprotnik, M., Bell, J. B. & Klein, R. Particle-Continuum Coupling and its Scaling Regimes: Theory and Applications. *Adv. Theory Simul.* **3,** 1900232 (2020).

84. Bonella, S., Ferrario, M. & Ciccotti, G. Thermal Diffusion in Binary Mixtures: Transient Behavior and Transport Coefficients from Equilibrium and Nonequilibrium Molecular Dynamics. *Langmuir* **33,** 11281–11290 (2017).

85. Ciccotti, G. & Jacuzzi, G. Direct computation of dynamical response by molecular dynamics: The mobility of a charged Lennard-Jones particle. *Phys. Rev. Lett.* **35,** 789–792 (1975).

86. Surblys, D., Matsubara, H., Kikugawa, G. & Ohara, T. Application of atomic stress to compute heat flux via molecular dynamics for systems with many-body interactions. *Phys. Rev. E* **99,** 051301 (2019).

87. Heinen, M. & Vrabec, J. Evaporation sampled by stationary molecular dynamics simulation. *J. Chem. Phys.* **151,** 044704 (2019).

88. Dibak, M., Fröhner, C., Noé, F. & Höfling, F. Diffusion-influenced reaction rates in the presence of pair interactions. *J. Chem. Phys.* **151,** 164105 (2019).

89. Zausch, J., Horbach, J., Virnau, P. & Binder, K. A combined molecular dynamics and Monte Carlo study of the approach towards phase separation in colloid–polymer mixtures. *J. Phys.: Condens. Matter* **22,** 104120 (2010).

90. Roy, S., Dietrich, S. & Höfling, F. Structure and dynamics of binary liquid mixtures near their continuous demixing transitions. *J. Chem. Phys.* **145,** 134505 (2016).

91. Vrabec, J., Kedia, G. K., Fuchs, G. & Hasse, H. Comprehensive study of the vapour–liquid coexistence of the truncated and shifted Lennard–Jones fluid including planar and spherical interface properties. *Mol. Phys.* **104,** 1509–1527 (2006).

92. Heier, M. *et al.* Equation of state for the Lennard-Jones truncated and shifted fluid with a cut-off radius of 2.5σ based on perturbation theory and its applications to interfacial thermodynamics. *Mol. Phys.* **116,** 2083–2094 (2018).

93. Straube, A. V., Kowalik, B. G., Netz, R. R. & Höfling, F. Rapid onset of molecular friction in liquids bridging between the atomistic and hydrodynamic pictures. *Commun. Phys.* **3,** 126 (2020).

94. De Buyl, P., Colberg, P. H. & Höfling, F. H5MD: a structured, efficient, and portable file format for molecular data. *Comput. Phys. Commun.* **185,** 1546–1553 (2014).

95. Huang, K. *Statistical mechanics* (Wiley, 1986).

96. Gay-Balmaz, F. & Yoshimura, H. Dirac structures in nonequilibrium thermodynamics for simple open systems. *J. Math. Phys.* **61,** 092701 (2020).

97. Delle Site, L. & Klein, R. Liouville-type equation for the n-particle distribution function of an open system. *J. Math. Phys.* **61,** 083102 (2020).

98. Gholami, A., Höfling, F., Klein, R. & Delle Site, L. Thermodynamic relations at the coupling boundary in adaptive resolution simulations for open systems. *Adv. Theory Simul.,* in press (2021).

99. Engquist, B. & Majda, A. J. Absorbing boundary conditions for the numerical evaluation of waves. *Math. of Comput.* **31,** 629–651 (1977).

100. Poblete, S., Praprotnik, M., Kremer, K. & Delle Site, L. Coupling different levels of resolution in molecular simulations. *J. Chem. Phys.* **132,** 114101 (2010).

101. Schnell, S. K., Vlugt, T. J., Simon, J.-M., Bedeaux, D. & Kjelstrup, S. Thermodynamics of a small system in a μT reservoir. *Chem. Phys. Lett.* **504,** 199–201 (2011).

102. Pathania, Y., Chakraborty, D. & Höfling, F. Continuous demixing transition of binary liquids: finite-size scaling from the analysis of sub-systems. *Adv. Theory Simul.* (2021).

103. Hertlein, C., Helden, L., Gambassi, A., Dietrich, S. & Bechinger, C. Direct measurement of critical Casimir forces. *Nature* **451,** 172–175 (2008).

104. Paladugu, S. *et al.* Nonadditivity of critical Casimir forces. *Nat. Commun.* **7,** 11403 (2016).

105. Puosi, F., Cardozo, D. L., Ciliberto, S. & Holdsworth, P. C. W. Direct calculation of the critical Casimir force in a binary fluid. *Phys. Rev. E* **94,** 040102(R) (2016).

106. Rohwer, C. M., Kardar, M. & Krüger, M. Transient Casimir Forces from Quenches in Thermal and Active Matter. *Phys. Rev. Lett.* **118,** 015702 (2017).

107. Krekeler, C. & Delle Site, L. Towards Open Boundary Molecular Dynamics Simulation of Ionic Liquids. *Phys. Chem. Chem. Phys.* **19,** 4701 (2017).

108. Shadrack Jabes, B., Krekeler, C., Klein, R. & Delle Site, L. Probing Spatial Locality in Ionic Liquids with the Grand Canonical Adaptive Resolution Molecular Dynamics Technique. *J. Chem. Phys.* **148,** 193804 (2018).

109. Shadrack Jabes, B. & Delle Site, L. Nanoscale domains in Ionic Liquids: A statistical mechanics definition for molecular dynamics studies. *J. Chem. Phys.* **149,** 184502 (2018).

110. Zavadlav, J. & Praprotnik, M. Adaptive resolution simulations coupling atomistic water to dissipative particle dynamics. *The Journal of Chemical Physics* **147,** 114110 (2017).

111. Delgado-Buscalioni, R., Sablić, J. & Praprotnik, M. Open boundary molecular dynamics. *Eur. Phys. J. Spec. Top.* **224,** 2331–2349 (2015).

112. Sablić, J., Praprotnik, M. & Delgado-Buscalioni, R. Open boundary molecular dynamics of sheared star-polymer melts. *Soft Matter* **12,** 2416–2439 (2016).

113. Delgado-Buscalioni, R., Kremer, K. & Praprotnik, M. Coupling atomistic and continuum hydrodynamics through a mesoscopic model: Application to liquid water. *The Journal of Chemical Physics* **131,** 244107 (2009).

114. Colberg, P. H. & Höfling, F. Highly accelerated simulations of glassy dynamics using GPUs: Caveats on limited floating-point precision. *Comput. Phys. Commun.* **182,** 1120–1129 (2011).

115. Muskat, M. & Wyckoff, R. D. *The flow of homogeneous fluids through porous media* (McGraw-Hill, New York, 1937).

116. Leitmann, S. & Franosch, T. Nonlinear Response in the Driven Lattice Lorentz Gas. *Phys. Rev. Lett.* **111,** 190603. http://link.aps.org/doi/10.1103/PhysRevLett.111.190603 (2013).

117. Lorentz, H. A. Le mouvement des electrons dans les metaux. *Arch. Néerl. Sci. Exactes Nat.* **10.** Proc. Amst. Acad. 7, 438 (1905), 336–370 (1905).

118. Van Beijeren, H. Transport properties of stochastic Lorentz models. *Rev. Mod. Phys.* **54,** 195–234 (1982).

119. Höfling, F., Franosch, T. & Frey, E. Localization Transition of the Three-Dimensional Lorentz Model and Continuum Percolation. *Phys. Rev. Lett.* **96,** 165901 (2006).

120. Höfling, F. & Franosch, T. Crossover in the Slow Decay of Dynamic Correlations in the Lorentz Model. *Phys. Rev. Lett.* **98,** 140601 (2007).

121. Spanner, M. *et al.* Splitting of the Universality Class of Anomalous Transport in Crowded Media. *Phys. Rev. Lett.* **116,** 060601 (2016).

122. Van Leeuwen, J. M. J. & Weijland, A. Non-analytic density behaviour of the diffusion coefficient of a Lorentzgas I. *Physica (Amsterdam)* **36,** 457–490 (1967).

123. Sahimi, M. Flow phenomena in rocks: from continuum models to fractals, percolation, cellular automata, and simulated annealing. *Rev. Mod. Phys.* **65,** 1393–1534 (1993).

124. Scholz, C. *et al.* Permeability of Porous Materials Determined from the Euler Characteristic. *Phys. Rev. Lett.* **109,** 264504 (2012).

125. Katz, A. J. & Thompson, A. H. Quantitative prediction of permeability in porous rock. *Phys. Rev. B* **34,** 8179–8181 (1986).

126. Stauffer, D. & Aharony, A. *Introduction to Percolation Theory* 2nd ed. (Taylor & Francis, London, 1994).

127. Höfling, F., Munk, T., Frey, E. & Franosch, T. Critical dynamics of ballistic and Brownian particles in a heterogeneous environment. *J. Chem. Phys.* **128,** 164517 (2008).

128. Machta, J. & Moore, S. M. Diffusion and long-time tails in the overlapping Lorentz gas. *Phys. Rev. A* **32,** 3164 (1985).

129. Machta, J., Guyer, R. A. & Moore, S. M. Conductivity in percolation networks with broad distributions of resistances. *Phys. Rev. B* **33,** 4818–4825 (1986).

130. Stenull, O. & Janssen, H. Conductivity of continuum percolating systems. *Phys. Rev. E* **64,** 56105 (2001).

131. Balberg, I. Excluded-volume explanation of Archie's law. *Phys. Rev. B* **33,** 3618–3620 (1986).

132. Balberg, I. Simple holistic solution to Archie's-law puzzle in porous media. *Phys. Rev. E* **103,** 063005 (2021).

133. Johnson, J. K., Zollweg, J. A. & Gubbins, K. E. The Lennard-Jones equation of state revisited. *Mol. Phys.* **78,** 591–618 (1993).

134. Klein, R. *Handbook of Mathematical Analysis in Mechanics of Viscous Fluids* (eds Giga, Y. & Novotny, A.) 2827–2868 (Springer, 2018).

135. EVANS, D. J. & MORRISS, G. P. *Statistical Mechanics of Nonequilibrium Liquids* (ANU Press, 2007).

136. Kundu, P. K., Cohen, I. M. & Dowling, D. R. *Fluid Mechanics* 6th ed. ISBN: 9780124059351 (Academic Press, Elsevier, San Diego, 2016).

137. Heinz, H. Calculation of local and average pressure tensors in molecular simulations. *Mol. Simul.* **33,** 747–758 (2007).

138. Varnik, F., Baschnagel, J. & Binder, K. Molecular dynamics results on the pressure tensor of polymer films. *J. Chem. Phys.* **113,** 4444–4453 (2000).

139. Todd, B. D., Evans, D. J. & Daivis, P. J. Pressure tensor for inhomogeneous fluids. *Phys. Rev. E* **52,** 1627–1638 (1995).